RAM ROBOTICS AND MECHATRONICS

NEEDLE TISSUE INTERACTION MODELLING FOR ENHANCEMENT OF FEEDBACK ACCURACY DURING BIOPSIES

L.F.P. (Lodewijk) Lemmens

MSC ASSIGNMENT

Committee:
dr. ir. M. Abayazid
M.S. Selim, MSc
dr. ir. J. Rouwkema

July, 2024

022RaM2024
Robotics and Mechatronics
EEMCS
University of Twente
P.O. Box 217
7500 AE Enschede
The Netherlands

UNIVERSITY OF TWENTE. | TECHMED CENTRE UNIVERSITY OF TWENTE. | DIGITAL SOCIETY INSTITUTE

Abstract

Needle biopsies are a critical yet challenging technique for early stage tumor diagnosis. This study presents a model designed to predict tissue deformation and needle deflection, alongside interaction forces, to enhance real-time visual and haptic feedback for surgeons. Utilizing Finite Element Modelling (FEM) and a four-step insertion procedure, the model includes the friction force using the modified Karnopp model and cutting force modelled as a constant. Validation was performed using a 10% wt gelatin phantom, simulating liver tissue, embedded with either screws or glitter. Force validation was done with an axial force sensor during three needle insertions at speeds of 2.5,3.33,5 and 10 mm/sec. Deflection and deformation where quantified by filming the needle insertions and tracking the movement. The glitter phantom method yielded the most accurate deformation measurements, with model predictions deviating an average of 23.1% in the x-direction and 31.2% in the y-direction. Needle deflection predictions showed an average difference of 0.101 mm compared to the experimental results. While there is room for improvement, the model demonstrates adequate accuracy to potentially enhance real-time haptic and visual feedback during liver biopsies.

Contents

1 Introduction

Liver cancer is the sixth most common cancer in the world with almost 867.000 new cases in 2020 (1) and over 758 725 deaths (1). Biopsy is the least invasive method surgeons can use to diagnose potential tumour tissue. The downside is that biopsies require a highly skilled surgeon who can work with imaging modalities, such as ultrasound, Computed Tomography (CT) or Magnetic Resonance Imaging (MRI), to accurately reach a moving target.
Providing accurate real-time feedback to surgeons is of major importance to target a small tumour tissue in its early stages. Some challenges associated with using imaging modalities for real-time feedback include prolonged exposure to radiation with CT-scans (13), long examination times with MRI scans, and the requirement for special non-magnetic biopsy needles for biopsy procedure (13). Ultrasound (US) is the best and most commonly used imaging modality for biopsies (13). The main drawback is that some structures are not visible using ultrasound (13), making CT or MRI the only viable option in such cases. The downsides of these imaging modalities make the procedure more challenging, increase the intervention time and decrease the accuracy. The extended intervention time results in prolonged exposure, which is more harmful for the patient when using CT.
Modelling needle-tissue interaction could help with increasing the accuracy of real-time haptic and visual feedback. First of all, the model can provide real-time visual feedback, helping surgeons understand the needles position relative to the tumor and plan their path accordingly. Currently, it is possible to generate real-time images of the liver movement due to breathing with the use of Generative Adversarial Networks (GAN's). With the use of real data, a model is trained that generates images of the liver that follow the pattern of the real data until a point where the real-time input is no longer needed. However, a significant drawback of using GAN's is that they can provide real-time predictions but not real-time feedback. These generated images cannot depict processes that weren't in the input such as feedback of the needle insertion. Incorporating a needle-tissue interaction model could enhance these generated images with real-time feedback, resulting in a more comprehensive solution. Second, the haptic feedback is of major importance when doing robotic supported biopsies (9). It helps surgeon's develop a better sense of touch and has been shown to reduce interaction forces and completion time. Modelling needle tissue interaction could help with providing real-time haptic and visual feedback of the process of needle insertion in liver tissue.
Currently in daily practice, a lot of surgeon's do biopsies by hand using a stiff needle and some rough needle steering. More recent research around biopsies is focused on robotic supported needle insertions (37) in which a biopsy is done by a surgeon at the leader side and a robotic device at the follower side. A next step is a fully autonomous biopsy done by a robotic device in which needle steering and pre-operative planning play a huge role (37). In tele-operation, it is important to provide the master (Interventional radiologist) with not only visual but also haptic feedback (9). This will result in a setup in which the knowledge of an experienced surgeon can be combined with the accuracy and possibilities of a robotic device. Again, a needle tissue interaction model can provide the necessary haptic and visual feedback. This research is focused on developing a needle insertion model that can predict liver tissue deformation and needle deflection based on the cutting, stiffness and friction forces of the needle liver interaction. With the use of Finite Element Modelling (FEM), a 4-step model can be created to accurately model the interaction between tissue and needle adopted from (16). With the use of this model, it is possible to show needle deflection and tissue deformation, while showing the interaction forces in the axial direction, to simulate a real-time biopsy.

Research question

This study aims to answer the following research question: How can tissue deformation and needle deflection be modelled to accurately estimate the deflections and deformations in a liver-mimicking phantom?

This can be split up into the following sub-questions :

- What specific bio-mechanical properties of liver tissue are crucial to accurately model for predictive needle insertion simulations?
- Which kind of model can optimally balance between realism and computational efficiency?
- What are the most accurate methods to validate the accuracy of the predictive needle insertion model?

2 Literature review

2.1 Part 1: Physical model of the needle-tissue interaction

This study focused on the visual and haptic feedback that can be provided to surgeons during liver biopsies. Our goal was to develop a realistic model that can predict needle deflection and tissue deformation based on forces modelled utilizing experimental data. In literature, there are a lot of physical models describing needle-tissue interaction. Misra *et al.* showed an overview of all the methods of tool-tissue modelling up to 2008 (27). These methods are linear elasticity-based, nonlinear (hyperelastic) elasticity-based finite element (FE) methods or various other techniques not relying on FE methods or continuum mechanics. Every one of these methods has its own downsides and advantages. Adam *et al.* proposed Meshless Total Lagrangian Explicit Dynamics (MTLED) since finite element discretization uses oversimplifying in case of complex tissue structures and time-consuming generation of grids (20). This method works best when coupled with a finite element method since meshless simulation can be used for geometries where good quality elements cannot be created. Since this study is working with homogeneous liver tissue with no intricate structures, this approach is unnecessarily complicated. GAO *et al.* wrote a paper on soft tissue surface deformation being explained on the basis of continuum mechanics and a geometry model is presented to approximate the volume of tissue deformation (16). This way it is possible to predict complex behaviour and dynamics of soft tissue. Niki *et al.* reviewed research on tissue deformation modelling, needle insertion force modelling and biomechanical properties of tissue (7). Their review emphasized the importance of robotics and simulation for achieving more accurate and safer needle insertions. They also highlighted how numerous studies have shown that the axial forces on an insertion needle are a summation of forces caused by different physical phenomena like cutting, deformation and, needle displacement. Herink *et al.* wrote an article about final element modelling using SOFA (19). SOFA produces less accurate results compared to ABAQUS due to several factors. The limited amount of calculation time in SOFA restricts the complexity and accuracy of the simulations. SOFA uses different mesh and proximity detection which results in a slightly larger needle guide. Jushiddi *et al.* studied the use of ABAQUS to simulate a bevel-tipped biopsy into soft gel (21). The study showed promising results with the model being much quicker than other more complex and time-consuming models. It must be noted that the modelling of agargel, used in this study, is quite different from a real in vivo situation. Okamura *et al.* modelled needle insertions in three parts 1. capsule stiffness, a nonlinear spring model and 2. friction, a modified Karnopp model and 3. cutting, a constant for a given tissue (31). One different approach is splitting up the interaction into multiple steps (16):

- No interaction between needle and liver tissue
- Interaction between needle and liver tissue but no cutting
- The moment the needle will cut through the tissue and the liver tissue relaxes
- Cutting of the needle through the liver tissue
- Retraction of the needle from the tissue.

This method will make use of needle-tissue coupling, which means that the interactive forces are displayed on the tissue and needle nodes, which makes it possible to show tissue deformation and needle deflection. This results in an efficient, accurate and robust method which is important for our purposes.

2.2 Part 2: Kriging based meta model that is trained offline

During the literature review, it became clear that using FEM to solve the needle-tissue interaction model is always computationally expensive. Computationally expensive processes take a long time to solve, resulting in delays making real-time use challenging. A newer article by Y.

Lei *et al.* adopted Kriging based modeling (24). A kriging-based model is a model that uses a limited data set to gain estimates of values over a continuous spatial field. The main advantage of Kriging based modelling is the offline training from the data set of the physical model, resulting in less computational expensiveness when run real-time. So Kriging based modelling will keep the accuracy of the detailed physical model because of offline training, but also be computationally less expensive because the trained Kriging based model can be used in real-time. Kriging based modeling encompasses a lot of different approaches. These approaches differ in the use of different semi-variance functions (e.g., spherical, exponential, rational ...). Mengxiao *et al.* wrote an article about validating Kriging based semi-variance functions based on data from experiments on soft tissue and concludes spherical is the best model (38). Since the complexity of FEM in our research isn't very high yet, due to the abstraction of how the liver tissue is modelled, it has not been implemented. However, it could become a viable option as the model's complexity increases.

2.3 Part 3: Needle-tissue force interaction validation

A lot of studies have been conducted to measure the needle tissue force interaction. Van Gerwen reviewed the influence of various factors on needle insertion force using experimental data found in literature (18). This showed the differences in order-of-magnitude of forces due to the large number of variables involved and the different experimental approaches. Indications were found that puncture forces decrease and friction force increases with increasing velocity as well as that larger needle diameters can cause higher peak forces. Okamora *et al.* studied the modelling of interaction forces into bovine liver studying the effect of needle diameter and tip type (31). They concluded that the most inclusive model is a combination of FEM and experimentally-determined force sources. Roesthuis *et al.* modelled the needle as a cantilever beam, using the interaction forces to predict needle deflection (35). Experimental values from bevel-tipped needle insertions into gelatin showed no difference in tip force between 10mm/sec and 20mm/sec. The friction force was found to be dependent on insertion depth and velocity. Misra *et al.* modelled the natural bending of a bevel-tipped needle into soft tissue and showed that the energy associated with needle-tissue interaction stiffness is more significant than the energy due to compression, rupture and tip loads (28). Bao investigated the mechanical performance of tracheal tissue when punctured. This may not be about the liver but proposed some interesting approaches to FE modelling, contact mechanics between needle and tissue based on material characteristics, needle diameter and puncture angle. (8). Fukushima *et al.* estimated the needle friction and tip forces, based on in vitro experiments and the recursive least square method, using a coaxial needle that was able to measure tip and friction force separately (14). Fukushima *et al.* also estimated the theoretical tip forces by subtracting the friction force, calculated using dynamic friction coefficients, from the total insertion force (15). They also calculated the experimental tip force by subtracting the insertion force with no cutting from the total insertion force. Kobayashi *et al.* modelled and validated friction forces based on their relative velocities (23). They showed that up to 1.5 mm/sec, the friction force is dependent on speed while with speeds higher than 1.5 mm/sec the frictional force is approximately constant. Kataoka *et al.* measured the tip and friction forces separately, during penetration of prostate tissue, using a 7-axial load cell (22). They showed a detailed force time curve to help understand the mechanics of needle penetration. Moore *et al.* studied elementary cutting tool edges to predict hollow needle insertion forces (29). They showed that higher inclination angles result in lower cutting forces. Dehghan *et al.* did a comparison of needle bending models (12). A comparison was made between finite element method Using triangular elements, finite element method using non-linear beam elements and angular spring model. The results showed that the Angular spring model was the easiest, fastest and most accurate simulation method for 2D implementation.

2.4 Part 4: Model implementation

A lot of research is dedicated to needle-tissue interaction modelling for path planning or needle steering purposes. Muzzammil *et al.* reviewed different path planning papers using bevel-tipped and flexible needles (30). Abayazid *et al.* studied ultrasound guided 3D needle steering through a gelatin phantom using an algorithm that reduces the amount of needle rotations achieving a sub-millimeter accuracy (6). Carriere *et al.* showed a needle steering model using a handheld device and an event triggered based controller to reduce needle deflection (11). The system uses a surgeon in the loop system in which the needle is steered automatically. With a reduced order kinematic bicycle model and with ultrasound feedback the next step is determined. Since it is still complex to design a model that is able to accurately predict deflection and deformation on a realistic liver model and run real-time, there is still a gap on the market that creates some opportunities.
This study aims to build and validate a real-time model, that can demonstrate needle deflection and tissue deformation along with force feedback, enhancing the imaging modality feedback with accurate optical and haptic feedback of real-time simulations. The model should be able to run real-time and provide visual/haptic feedback with high accuracy, allowing all kinds of needle movements. The modelled tissue will consist of a 2D homogeneous liver-mimicking material.

3 Methods and Materials

This chapter has been divided into two sections: simulation and validation. The first part of this chapter will be dedicated to explaining the work of the predictive model of needle into soft tissue. The second part explains the reasoning behind the validation of the simulation output.

3.1 Equations of simulation

Part 1: Physical model of soft tissue

The mechanical behaviour of the simulation can be modelled as two interrelated components that can be coupled to form an interconnected model. The first part represents the deformation of the tissue, while the other part describes the interaction with the needle. Initially, the deformation of the tissue can be modelled using the following dynamic equations (16):

$$M\ddot{u}(t) + C\dot{u}(t) + Ku(t) = Q(t) \tag{3.1}$$

Where M represents the mass matrix, C the damping matrix, K the stiffness matrix, Q the loading matrix and u equals the nodal displacement vector.
For modelling the tissue this way, important assumptions for the tissue are homogeneity and linear-elasticity. The Newmark method, a numerical integration technique for solving differential equations, gives the nodal displacement and velocity. The equations are given by:

$$\dot{u}_{t+\Delta t} = \dot{u}_t + [(1-\delta)\ddot{u}_t + \delta\ddot{u}_{t+\Delta t}]\,\Delta t \tag{3.2}$$

$$u_{t+\Delta t} = u_t + \dot{u}_t\Delta t + \left[\left(\frac{1}{2} - \xi\right)\ddot{u}_t + \xi\ddot{u}_{t+\Delta t}\right]\Delta t^2 \tag{3.3}$$

Integrate these expressions into equation 3.1, and the displacement at time $t+\Delta t$ is obtained as:

$$\begin{aligned}\left(K + \frac{1}{\xi\Delta t^2}M + \frac{1}{\xi\Delta t}C\right)u_{t+\Delta t} &= Q_{t+\Delta t} \\ &+ M\left[\frac{1}{\xi\Delta t^2}u_t + \frac{1}{\xi\Delta t}\dot{u}_t + \left(\frac{1}{2\xi} - 1\right)\ddot{u}_t\right] \\ &+ C\left[\frac{\delta}{\xi\Delta t}u_t + \left(\frac{\delta}{\xi} - 1\right)\dot{u}_t + \left(\frac{\delta}{2\xi} - 1\right)\Delta t\ddot{u}_t\right]\end{aligned} \tag{3.4}$$

This equation can be written with general force and displacement as:

$$\mathbf{K}_{\text{tissue}} \cdot u = F \tag{3.5}$$

Where F is the general force vector, u is the displacement vector and $\mathbf{K}_{\text{tissue}}$ is the general stiffness vector which can be defined after determining the mesh and material properties. The global tissue stiffness matrix can be determined under the assumption of homogeneous material. The local stiffness matrix can be defined as (10):

$$\mathbf{K}_e = B' * D_e * B * \text{weight} * \det(J) \tag{3.6}$$

While the local mass matrix can be defined as:

$$\mathbf{M}_e = \int_{\Omega_e} N_e^T \rho N_e \, d\Omega \tag{3.7}$$

which is solved numerically in the code. The local damping matrix is solved using Rayleigh damping:

$$\mathbf{C}_e = \alpha * \mathbf{M}_e + \beta * \mathbf{K}_e \tag{3.8}$$

with α being 0.01 and β being 0.1. B is the strain-displacement matrix which can be calculated using the shape function derivatives with respect to the global coordinates using the Jacobian. **D** is defined as the elasticity matrix for isotropic materials being (3):

$$\mathbf{D}_e = \begin{bmatrix} \lambda+2\mu & \lambda & 0 \\ \lambda & \lambda+2\mu & 0 \\ 0 & 0 & \mu \end{bmatrix} \tag{3.9}$$

$$\lambda = \frac{E\nu}{(1+\nu)(1-2\nu)} \tag{3.10}$$

$$\mu = \frac{E}{2(1+\nu)} \tag{3.11}$$

These matrices can all be combined into the global mass, damping and stiffness matrices. Using Newmark's method, it is possible to calculate the displacement given the force.

Physical model of needle

The flexible needles are modelled as a solid bar with a constant length (16). The relationship between the needle deflection and force can be modelled as follows:

$$\begin{cases} \omega_1 = k_1 \left(\sum_{i=1}^{i=n} F_i\right) \\ \omega_2 = k_2 \left(\sum_{i=2}^{i=n} F_i\right) + \Delta_{1,2} \times \frac{3k_1}{2l_1} \left(\sum_{i=1}^{i=n} F_i\right) \\ \vdots \\ \omega_n = k_n F_n + \sum_{j=1}^{j=n-1} \left(\Delta_{j,n} \times \frac{3k_j}{2l_j} \left(\sum_{i=j}^{i=n} F_i\right)\right) \end{cases} \tag{3.12}$$

with $k_i = (\frac{l^3}{3EI})$,$\Delta_{i,j}$ equals the distance between point i and j and l_i denotes the distance between point i and the base of the needle support. This can be rewritten as $F_x = \overline{\mathbf{K}} \cdot \omega$, since ω is a linear function of F.
Under the assumption that $F_{iy} << F_{ix}$ then $F_{iy} = 0$. This means that the deformation in the x direction is only equal to ω and the deformation in the y direction is only equal to the displacement u. So $F_y = \overline{\mathbf{K}} \cdot \omega$ can be rewritten as:

$$F = \begin{bmatrix} 0 & 0 & 0 & \cdots & 0 \\ 0 & K_{1,1} & 0 & \cdots & K_{1,n} \\ 0 & 0 & 0 & \cdots & 0 \\ \vdots & \vdots & \vdots & \ddots & \vdots \\ 0 & K_{n,1} & 0 & \cdots & K_{n,n} \end{bmatrix}_{2n \times 2n} \cdot u = \hat{\mathbf{K}}_n \cdot u \tag{3.13}$$

With u as $[u_{1x}, \omega_1, \ldots, u_{nx}, \omega_n]^{\mathrm{T}}$
The local stiffness matrix of the needle has been determined using the general formulas for beam element matrices (17).

$$\begin{bmatrix} V_1 \\ M_1 \\ V_2 \\ M_2 \end{bmatrix} = (EI) \begin{bmatrix} \frac{12}{L^3} & \frac{6}{L^2} & -\frac{12}{L^3} & \frac{6}{L^2} \\ \frac{6}{L^2} & \frac{4}{L} & -\frac{6}{L^2} & \frac{2}{L} \\ -\frac{12}{L^3} & -\frac{6}{L^2} & \frac{12}{L^3} & -\frac{6}{L^2} \\ \frac{6}{L^2} & \frac{2}{L} & -\frac{6}{L^2} & \frac{4}{L} \end{bmatrix} \begin{bmatrix} \Delta_1 \\ \theta_1 \\ \Delta_2 \\ \theta_2 \end{bmatrix} \tag{3.14}$$

Given that there is no rotation ($\theta = 0$) and the deflection in the y-direction equals zero the above matrix can be simplified into:

$$\begin{bmatrix} V_1 \\ M_1 \\ V_2 \\ M_2 \end{bmatrix} = (EI) \begin{bmatrix} \frac{12}{L^3} \\ \frac{6}{L^2} \\ -\frac{12}{L^3} \\ \frac{6}{L^2} \end{bmatrix} \begin{bmatrix} \Delta_1 \end{bmatrix} \tag{3.15}$$

So the local needle stiffness matrix that connects the displacement of the needle to the force is only $\frac{12*E*I}{L^3}$. This can be incorporated into the global stiffness matrix of the needle.

Force determination

Now that the needle and tissue models are established, it's important to look into the forces during the 4 stages (16): interaction between needle and liver tissue but no cutting, the moment the needle will cut through the tissue and the liver tissue relaxes, insertion of the needle through the liver tissue and retraction of the needle.

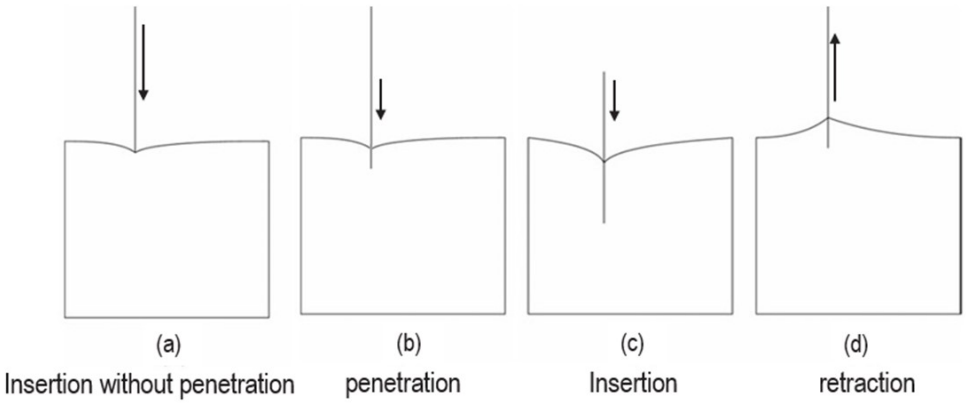

Figure 3.1: The four stages of the needle insertion. A) Interaction between needle and liver tissue but no cutting B) The moment the needle cuts through the tissue and the liver tissue relaxes C) Insertion of the needle through the liver D) Retraction of the needle. Adapted and edited from: "Modeling and Simulation of Flexible Needle Insertion Into Soft Tissue Using Modified Local Constraints" by Gao *et al.* (16)

In the first phase, there is no cutting of the needle, only deformation of the liver tissue due to the needle pressing on the liver tissue. This continues until the cutting force exceeds the piercing threshold and pierces into the liver tissue. The needle deformation can be calculated using $\omega = K_1^{-1} F_1$. The cutting force on the top of the needle can be calculated using (8):

$$F_1 = \frac{2Ez^2}{\pi(1-\nu^2)\cot(\alpha)\sin(\theta)} \tag{3.16}$$

With θ being the insertion angle, α being the bevel angle, E being the tissue Young's modulus and μ being the tissue Poisson's ratio and z being the travelled distance. This can be summarized as:

$$\begin{cases} F = F_1 = \frac{2Ez^2}{\pi(1-\nu^2)\cot(\alpha)\sin(\theta)} \\ y_2 = K_{\text{needle}}\, F \end{cases} \tag{3.17}$$

When the cutting force exceeds the threshold, the needle will pierce into the liver tissue. Once pierced the force is modelled as a combination of the friction force and the cutting force. Friction force being proportional to the needle depth into tissue and its relative velocity and the cutting force being dependent only on velocity. Section 3.2 explains more in-depth the forces used in the simulation.

Coupling of Tissue-Needle model

When the needle nodal points coincide with the tissue node points the force and displacement of the needle in tissue can be written as:

$$F_G = \mathbf{K}_{\text{needle}} \cdot u_G \tag{3.18}$$

The insertion of the needle causes a change in stiffness in the area. In this case $\mathbf{K}_G = \mathbf{K}_{\text{tissue}} + \mathbf{K}_{\text{needle}}$ which leads to:

$$\mathbf{K}_G \cdot u = \mathbf{F} \tag{3.19}$$

Solution

The general model for needle-tissue coupling:

$$\hat{\mathbf{K}}_G \cdot \begin{bmatrix} u_P \\ u_R \\ u_B \end{bmatrix} = \begin{bmatrix} K_{11} & K_{12} & K_{13} \\ K_{21} & K_{22} & K_{23} \\ K_{31} & K_{32} & K_{33} \end{bmatrix} \cdot \begin{bmatrix} u_P \\ u_R \\ u_B \end{bmatrix} = \begin{bmatrix} F_P \\ F_R \\ F_B \end{bmatrix} \tag{3.20}$$

Since the force on the rest nodes is zero ($F_r = 0$) and the displacement of the boundary nodes is zero ($u_B = 0$), the solution equals:

$$\begin{bmatrix} u_P \\ u_R \end{bmatrix} = \begin{bmatrix} K_{11} & K_{12} \\ K_{21} & K_{22} \end{bmatrix}^{-1} \begin{bmatrix} F_P \\ 0 \end{bmatrix} \tag{3.21}$$

This gives us the opportunity to calculate the displacement of the tissue nodes around the needle (u_p) and the rest nodes (u_r).

3.2 Forces used in simulation

There are a lot of studies dedicated to modeling forces acting on a needle. A lot of modelling methods are computationally expensive and hard to solve in real-time. To keep the modelled forces accurate but not too complex, they are modelled as a lumped force model (31). This means that the total force acting on the needle can be built up from five forces generated by different sources:

$$F_{\text{needle}} = F_{\text{friction}} + F_{\text{cutting}} + \text{torque} + F_{\text{stiffness}} + F_{\text{radial}} \tag{3.22}$$

Friction force

The friction force is the force that the tissue and needle generate while sliding against each other and acts upon the needle shaft. The friction force has been found to be dependent on insertion speed and insertion depth (35) and can be modelled with the use of the modified Karnopp friction model (31):

$$F_{\text{friction}}(\dot{z}, F_a) = \begin{cases} C_n \text{sgn}(\dot{z}) + b_n \dot{z}, & \dot{z} \leq -\Delta v/2 \\ \max(D_n, F_a), & -\Delta v/2 < \dot{z} \leq 0 \\ \min(D_p, F_a), & 0 < \dot{z} \leq \Delta v/2 \\ C_p \text{sgn}(\dot{z}) + b_p \dot{z}, & \dot{z} \geq \Delta v/2 \end{cases} \tag{3.23}$$

This implies that once a needle is below a speed that is considered zero there is only a static friction force (D) but once the speed is higher than zero the friction force is dependent on a dynamic friction force (C) and a damping coefficient (b).

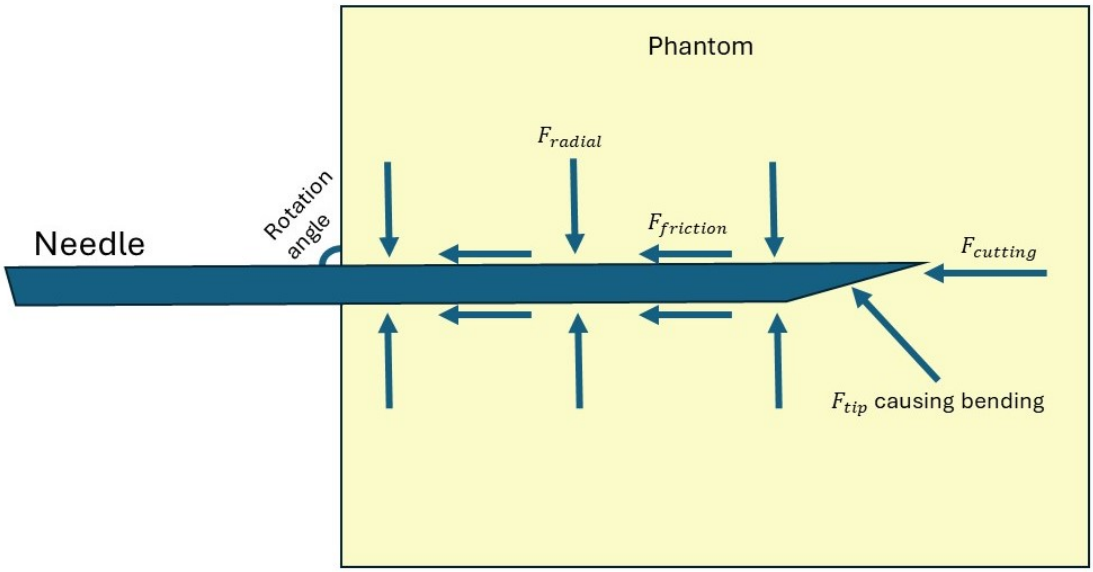

Figure 3.2: Forces acting on the needle during an insertion. F_{friction} acting along the needle shaft. F_{radial} acting orthogonal on the needle shaft. F_{cutting} acting on the tip of the needle. F_{tip} acting perpendicular to the bevel tip causing bending. Torque and stiffness forces are not shown here.

Cutting force

The cutting force is the force that exists at the tip of the needle to cut through the tissue. Cutting is an iterative process consisting of cutting and compressing. In this study, the cutting force is modelled as a constant, independent of penetration depth, while inside the tissue and zero while outside the tissue resulting in:

$$f_{\text{cutting}} = \begin{cases} 0, & t_p > t > l_p \\ f_{\text{cutting}}, & t \geq t_p \end{cases} \tag{3.24}$$

In which t is the puncture location, t_p is the needle tip location and l_p is the phantom length. Since, in this study, the phantom is homogeneous the assumption can be made that there are no different structures that influence the cutting process.

Stiffness force before puncture

This is the force that happens due to the tissue being compressed but no cutting happens. All the force that is happening is stiffness force of the tissue on the tip of the needle and can be calculated using equation 3.16. This stiffness force results in compression of the tissue without any cutting taking place.

Torque force

The torque force of the needle is only present when the needle is rotated (see figure 3.2). With rotation, the torque is determined by the friction of the tissue on the rotating needle. This can create a lag which means that the tip of the needle is not rotated as far as the base of the needle. The torque of the needle can create a deformation of the tissue around the needle but since this model is in 2D this deformation is neglected.
The torque that the needle needs to exert when the needle needs to make an angle change of 180 degrees in 1 second is calculated with the following formula (33):

$$\tau_b = b * \dot{\theta} \tag{3.25}$$

In which b is the damping coefficient and $\dot{\theta}$ is the angular speed. In this case, the damping coefficient has been found in literature and experimentally.
The second torque is when there is no needle steering using rotation of the needle but needle steering by changing the angle of the needle while it is inserted. When the needle is inserted and the surgeon wants to change its direction, it bends the needle in a certain direction. The tissue pushes against the direction of the needle and creates a torque. It can be calculated using the FEM model of the tissue using $F = K * u$ in which u is the movement of the tissue due to the needle moving and K is the stiffness matrix of the tissue. The assumption is made that there is no tissue tearing while rotating the needle.

Radial force

The radial force is the force exerted by the tissue on the needle. This could cause the needle to bend in different ways if the tissue has an unsymmetrical form. In this research insertions in a symmetrical phantom have been conducted, so the radial force is the same on all sides and won't affect the needle bending.

3.3 Different movements possible in the simulation

During this research, a model has been created in which certain aspects can be implemented based on movement of the needle. The first and simplest model is the **normal insertion** in which a needle is inserted perpendicular to the homogeneous liver tissue. The liver tissue being a 2D $120 \times 80 mm^2$ rectangle consisting of 600 nodes. Parameters of the tissue and needle can be adjusted according to the desired mechanical properties. A more complicated model has been designed, **angled insertion**, in which a needle can be inserted with a rotation angle less than 90 degrees. Everything else is the same as in the previous model. On both models, some more complex needle movements have been explored. First, the needle can be rotated around the rotation angle once inside the tissue, **needle rotation**, causing a lot of tissue deformation. Second, the needle can be **retracted** from the tissue. This last one has not been investigated in depth because it is not as important as the other models.
For all movements (see figure 3.3) visualisation of the needle deflection and tissue deformation was the most important part together with showing the cutting and friction force real-time.

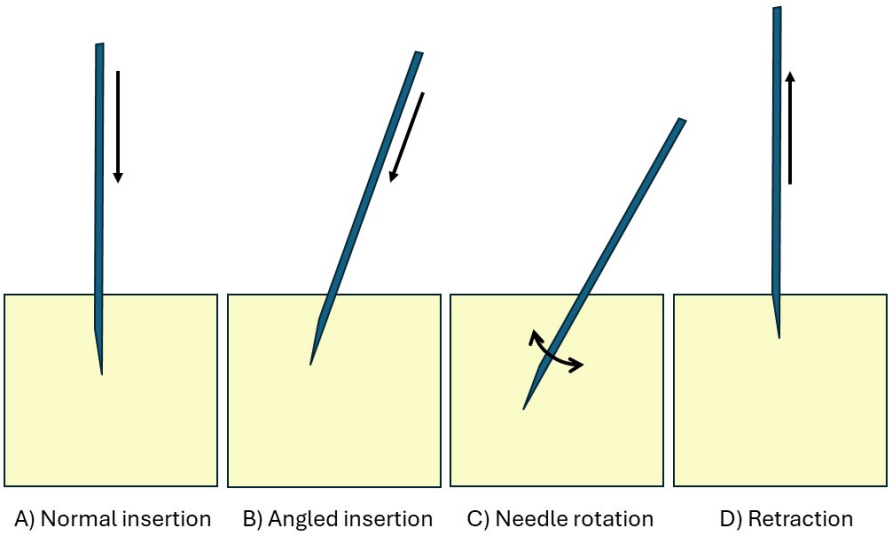

Figure 3.3: The four different needle movements possible in the simulation.

3.4 Parameters used in simulation

The parameters used while building the simulation are collected from literature.

Table 3.1: Parameters of the tissue, found in literature to help build the model.

Tissue Parameters	Value	Unit
Tissue Mesh Nodes	600	-
Tissue Mesh Width	120e-3	m
Tissue Mesh Height	80e-3	m
Tissue young's modulus (16)	80e3	N/m^2
Poisson's ratio (16)	0.49	-
Gamma (16)	0.5	-
Beta (16)	0.25	-
Damping Coefficient (31)	212.31	N s/ m^2
Dynamic friction (31)	10.57	N/m
Cutting Threshold (31)	2.3040	N
cutting force (35)	0.3	N

Table 3.2: Parameters of the needle, found in literature, to help build the model.

Needle Parameters	Value	Unit
Needle Nodes	40	-
Needle Length (2)	0.15	m
Young's modulus needle (16)	200e9	N/m^2
Moment of inertia needle (16)	7.854e-13	m^4
Needle Diameter (2)	1e-3	mm
Needle bevel angle	30	deg

3.5 Simulation Assumptions

To design a model of a needle penetrating into soft tissue, that needs to run real-time, several assumptions need to be made. These assumptions keep the computational cost of the model within the desired boundaries, allowing it to run real time. The key assumptions and their implications are discussed below:

1. • **The liver tissue is assumed to be homogeneous**
   – In reality, a liver consists of different tissue structures which influence the way the tissue/needle deforms. The model mimics a 2D 120×80 mm^2 rectangular section of homogeneous liver tissue, which limits the visualization of the needle bending to the x- and y- y-direction. It is not possible to show the bending in the z-direction.

2. • **Simplification of input forces**
   – Higher detailed force modelling could increase accuracy but would significantly increase the computational cost and thus the delay. This model uses an initial stiffness force, cutting force and friction force phase. First, the needle compresses the tissue without cutting which causes a stiffness force on the needle tip and tissue. Next, the stiffness force exceeds the threshold and cutting starts happening and the needle penetrates the tissue. Here an assumption is made to simplify the cutting and friction force a bit. The friction coefficient

is modelled as a dynamic parameter depending on velocity and penetration depth while the cutting force is modelled as a constant (31).

3. • **Boundary condition**
   - In the simulation, boundary conditions are set to all the sides except for the insertion point. In a real body, the liver will be surrounded by other organs/-tissue/bone which will create a boundary condition. In the simulation, this is modelled by setting a high stiffness to the boundary nodes. This is an oversimplified way of simulating the boundary conditions that are present in the body but more details requires a higher computational burden resulting in a larger delay.

4. • **Stiffness adjustment around needle**
   - The tissue around the needle stiffens due to the presence of the needle. The nodes around the needle with increased stiffness are identified by locating all the tissue nodes within a certain range around the needle. To prevent continuous movement of the nodes under constant friction force, the stiffness of the contact nodes increases over time. This ensures that the needle eventually slips past the nodes, instead of dragging them along, mimicking more realistic behaviour.

5. • **Needle types**
   - In the simulation, different needles are used with different stiffnesses depending on the use of the needle. When the user wants to do needle steering with the use of the bevel tip of the needle, the needle needs to be flexible. If the user likes to insert a needle and change the angle by force, a stiffer needle that will hardly bend needs to be used.

3.6 Validation of input parameters for the simulation

During this study, the purpose is to design a realistic model that can run real-time. The designed model has to be validated against measurements on a real phantom. The purpose of this validation is to see whether the correct input parameters have been used and whether the simulation gives accurate deformation/deflection results based on the input.

Friction force

The first parameter to validate is the friction force of the needle within the phantom tissue. In the model, a friction coefficient is used to determine the force based on speed and insertion depth. To validate this coefficient, experiments need to be conducted where the isolated friction force, the insertion speed and the needle location are known. The total force of the interaction with the needle and tissue is known as:

$$F_{\text{measured}} = F_{\text{cutting}} + l(C_n sgn(\dot{z}) + b_n \dot{z}) \tag{3.26}$$

In this equation, there are two unknowns, the dynamic friction (C_n) and damping coefficient (b_n). With 2 unknowns a minimum of 2 experiments at 2 different speeds ($\dot{z}$) need to be conducted to find the value of both unknowns. Given that the measured force at a given length is known, and the cutting force is calculated at a given speed, the dynamic friction and damping coefficient can be calculated.

Cutting force

The second force that needs to be validated is the cutting force. This force is present as long as the needle moves and the tip is inside the phantom. The cutting force is assumed to be a

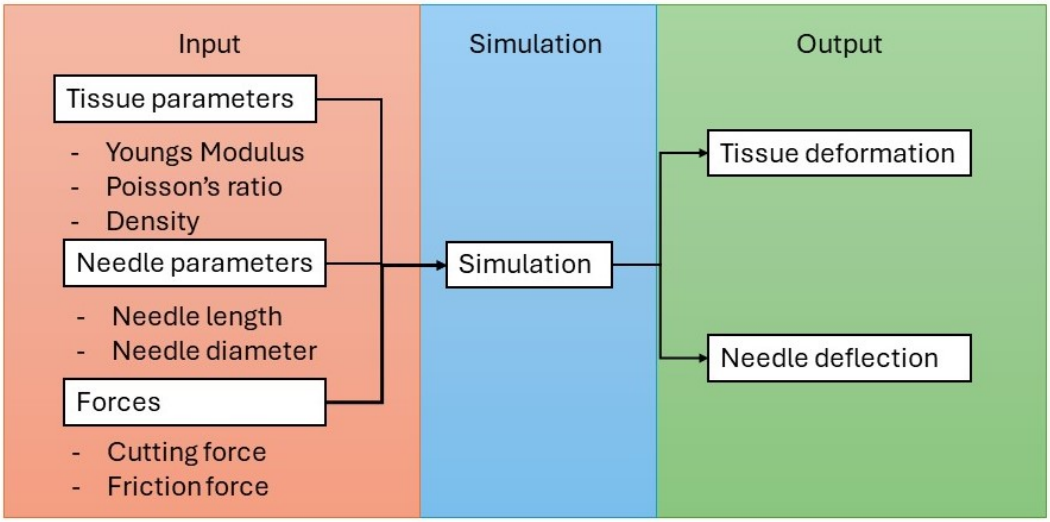

Figure 3.4: Overview of the input and output of the simulation.

constant force during the insertion. To determine the cutting force, a penetration all the way trough the phantom needs to be done to isolate friction force from cutting force. When the tip is outside the phantom, only friction force is present with a constant surface area with the phantom. The cutting force is calculated by subtracting the measured force of the moment the needle is outside the phantom from the measured force when the needle is just about to exit the phantom. Important factors are the constant speed, accurate needle location and the measured force when the needle is outside the phantom in a relaxed phantom state.

Young's modulus and Poisson's ratio

The Young's modulus and Poisson's ratio can be determined using advanced machinery that wasn't available for this study. Because the exact amount of gelatin and other ingredients in the phantom are known Young's modulus and Poisson's ratio can be determined from literature. It is crucial that the phantom is built the exact same way as described in the source and is homogeneous everywhere.

Density

The density of the phantom can be determined by weighing it on a scale and measuring its volume. The volume is known from the mould that is used to build the phantom. Dividing the mass by the volume yields the density.

3.7 Validation of the output of the simulation

After these input values are validated, and the model is changed accordingly, a needle deflection and tissue deformation can be obtained from the simulation. The output of the simulation needs to be validated against the output from experiments.

Needle deflection

The needle deflection can be found by filming the whole insertion into the phantom. On the first frame of the needle entering the tissue and the last frame of the needle movement, the location of the needle tip can be found resulting in the deflection. This deflection can be compared to the deflection found in the simulation.

Tissue deformation

The tissue deformation is a bit more difficult to determine since gelatin is transparent and deformation is hard to track with only a camera. To track the tissue deformation, one phantom with small screws and one with glitter inside are built. These embedded screws/glitter will move with the phantom deformation once hard. The whole insertion of the needle will again be filmed and the movement of the screws/glitter can be tracked using the Kanade-Lucas-Tomasi algorithm (4). The core principle of this algorithm is that it takes a small window around the point of interest and finds the best match in the next frame. The best match is found by minimizing the error between two frames by looking at the pixel intensities and the optical flow. It is crucial to calculate a pixel to mm conversion, by filming an object with known length while filming the phantom. The length of the object is divided by the amount of pixels it contains, which results in the conversion factor. The deformation of the embedded screws/glitter is validated against nodes on the same location in the simulation.

4 Validation

The experiments aim to validate the output of the simulation model. During the experiments, it is important to keep track of what parameters need to be evaluated and which remain constant and known. The initial experiments validate the input parameters of the simulation model such as friction force coefficient, cutting force constant, Young's modulus, Poisson's ratio and density. The second experiment is to validate the output of the simulation model, including needle deflection and tissue deformation. First, the setup will be introduced. Next, the experimental protocol will be explained.

4.1 Pre-experimental setup choices

During the design of the experimental setup, it was important to consider all factors that influence the simulation. An initial experiment was conducted with a gelatin phantom. This could show the deficiencies of the setup and help in making some design changes. The first important factor was constant insertion speed. This is done by giving a pulse function as input (see figure 4.1):

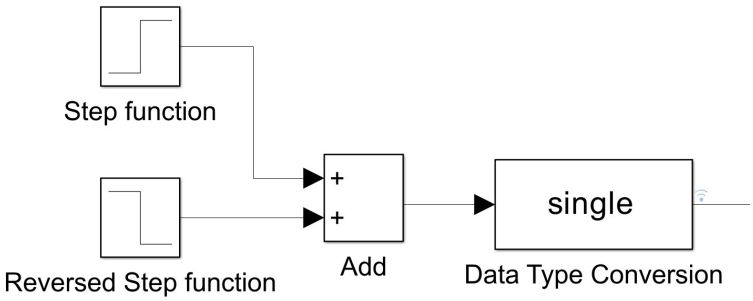

Figure 4.1: Overview of Simulink adjustment to provide the model with a pulse function as input. The two step functions are added up to form a pulse function, which is then converted to the correct data type to be compatible with the output of sensors.

By adding up the two step functions, a pulse function is created that moves the needle to the desired location and back at a constant speed, ensuring consistent needle movement viable for comparison.
The second critical aspect of the setup is the movement of the needle at a constant and known speed. To test this, the needle was moved for a predetermined time, and the distance travelled was measured by hand. It became apparent that the values in the setup were outdated. The Simulink model lacked a parameter to directly change the insertion speed so four Simulink models have been developed with insertion speeds of 2.5, 3.33, 5 and 10 mm/sec.
The phantom needed to be homogeneous and representative of liver tissue. Literature research indicated that 10% wt gelatin concentration best simulates liver tissue (36). To maintain the properties of the phantom for a longer time, one-third of the phantom consisted of cleaning vinegar. To validate that cleaning vinegar doesn't affect the phantom properties, since in literature only water is used, a phantom with solely water was constructed for validation.
The 100% water phantom is also used to make sure that only friction force is measured after the needle exits the phantom. This is done by pausing the needle for 5 seconds before being moved forward again. This allows the phantom to fully relax, ensuring that only the friction force is measured.

Set up for force validation

In this study, all simulations and programs are run on a Lenovo Thinkpad gen 11 (13e generation Intel® Core™ i7-1355U-processor, 32GB). All simulations and Simulink models were developed with the use of Matlab 2023a and 2023b. The experimental setup consists of a leader and follower side. The leader side consists of a Simulink model which is used to move the 18G needle with the use of a 5V Linear Actuator Stepper Motor on the follower side. The needle can be moved into a phantom holder which can hold a phantom of $120 \times 55 \times 80$ mm^3. The phantom holder is secured in its place with tape behind it so that it isn't able to move back but can be shifted sideways to make sure needle insertions can be done at different locations. The insertion device is connected to the laptop via an Arduino board. The forces are measured at the base of the needle with an axial Piezoresistive force sensor with a range of 0-10 N. This study made use of a gelatin phantom made out of 60 gr gelatin (10% wt), 180 ml cleaning vinegar and 360 ml water. The full setup can be found in figure 4.2.

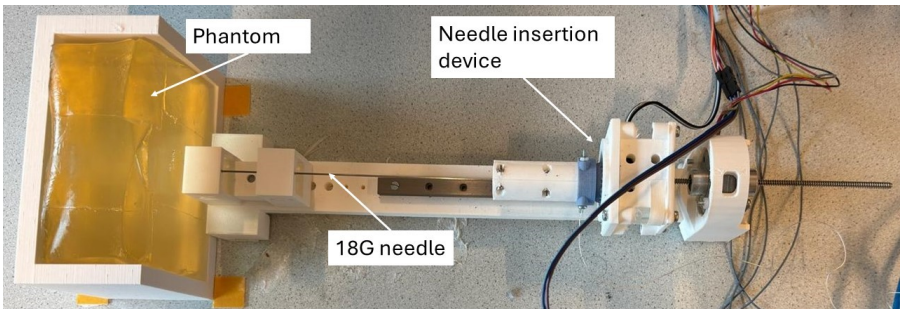

Figure 4.2: Experimental setup, used for force validation, showing the needle insertion device, the 18G needle, phantom and haptic handle.

Since there is only an axial force sensor at the base of the needle there is only one force output and one cannot distinguish between the cutting and friction force. To tackle this problem a phantom holder is designed, that allows full penetration of the needle through the phantom, using Solidworks 2023 (see figure 4.3 and 4.4. The needle will penetrate with constant speed through the phantom and exit at a hole at the other side of the phantom holder.

Setup for Needle deflection and tissue deformation validation with the use of screws

For validation of the simulation output, the same setup can be used as for the force validation (see figure 4.2). The only change will be within the phantom and the orientation of the phantom holder. Because of the transparency of the used gelatin phantom, it is really hard to track deformation. This has been solved by embedding screws into the gelatin phantom created from out of 10% wt gelatin 33.3% cleaning vinegar and 66.6% water. The phantom is created in two phases. In the first phase, half of the phantom is created and set in the fridge overnight. The next day screws are stuck in the phantom at the same location as the mesh nodes in the simulation and the other half of hot gelatin is poured over this and the screws get melted into the phantom. This will result in a phantom with embedded nodes that can be used to track tissue deformation. The phantom holder will be placed on its side so the needle insertion device can stay in its place and the needle is inserted from the top. The setup for the force validation has been expanded with a camera of an iPhone 15 pro to film the whole insertion at a quality of 4k 60 fps. The whole setup can be found in figure 4.5.

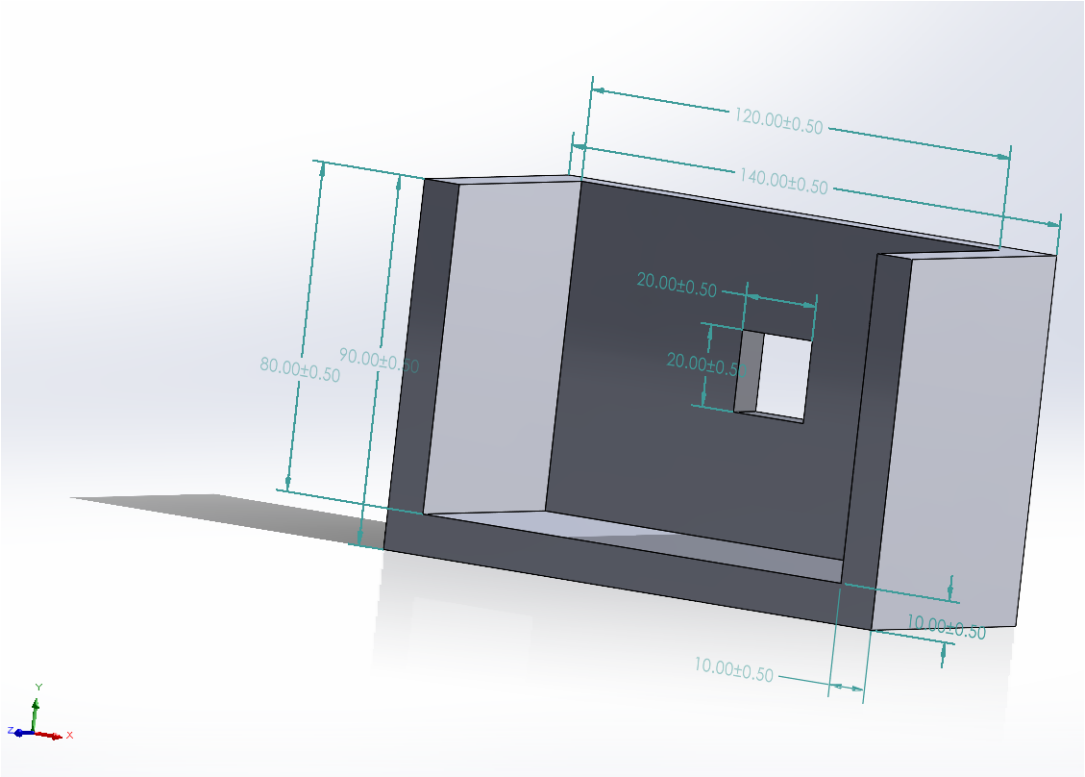

Figure 4.3: Simulink model of the phantom holder with a 20x20mm hole to allow full penetration.

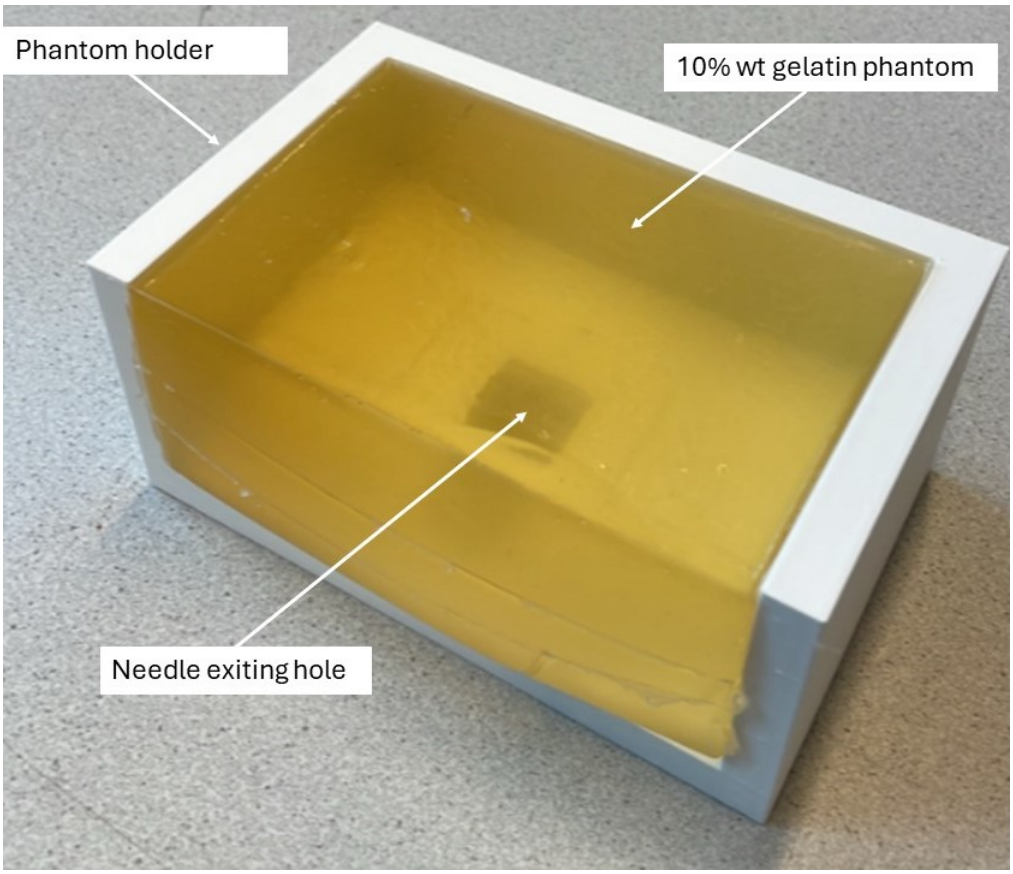

Figure 4.4: 3D printed phantom holder with 10% gelatin phantom inside.

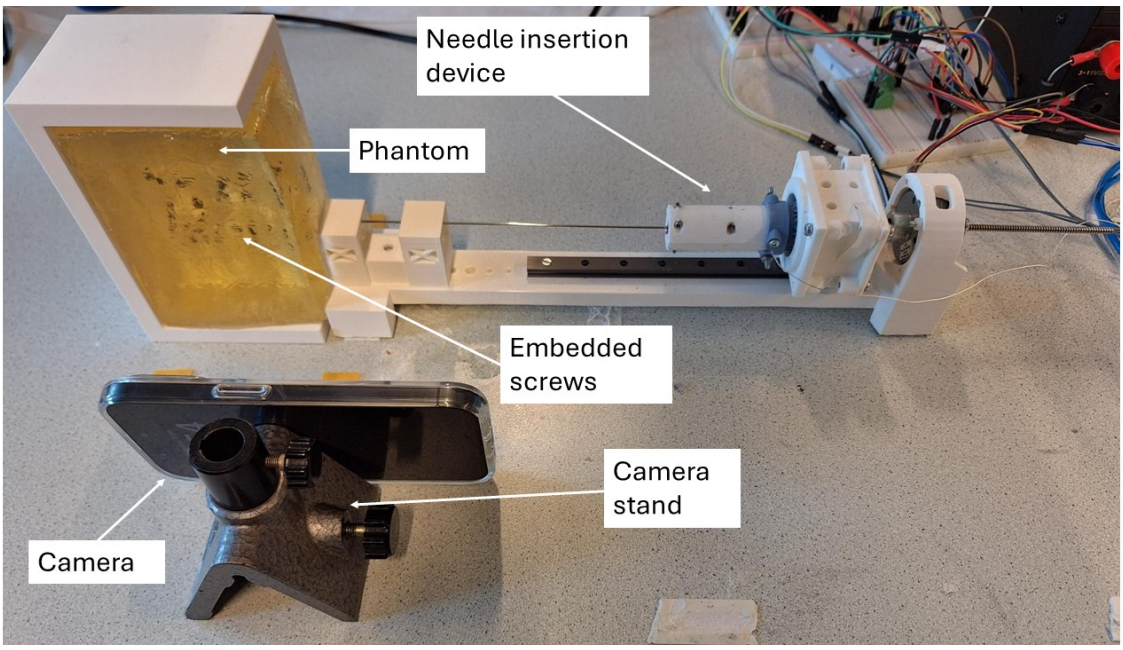

Figure 4.5: Experimental setup for the simulation output validation, showing the phantom with embedded screws, the needle insertion device and, the camera stand.

As can be seen in figure 4.6 (left) the screws were put in straight into the first half of the phantom. When the second half of the hot gelatin was poured, the screws started moving because of remelting of the gelatin that held the screws in place. Due to the screws being in the same plane, this was still usable for the experiments.

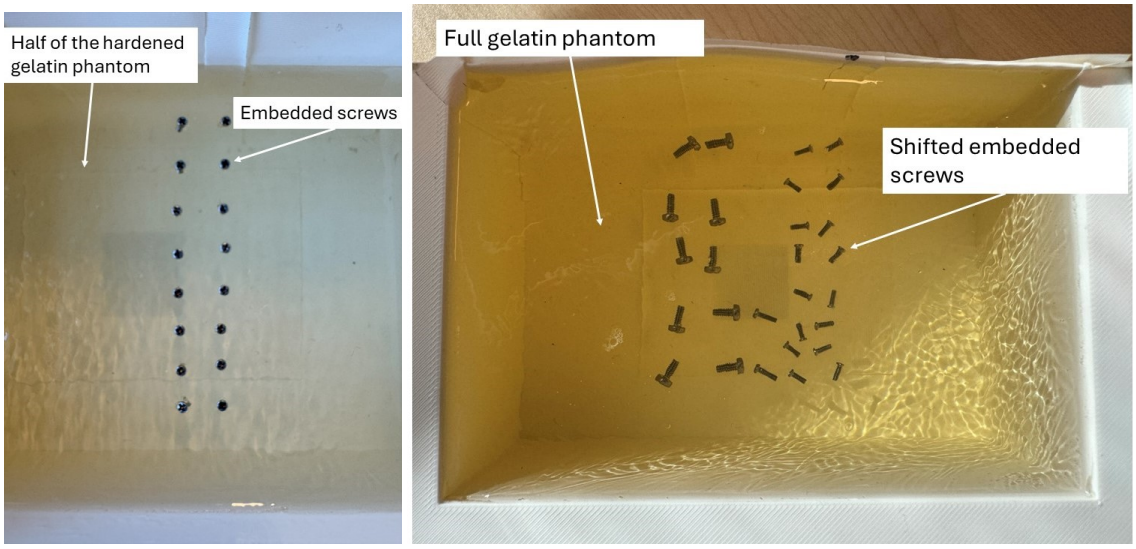

Figure 4.6: Left: Half of the phantom, that has hardened overnight in the fridge, with the screws still in a straight line. Right: The whole phantom with the embedded screws, which have moved due to the remelting of the gelatin in the left figure that originally held the screws.

Setup for Needle deflection and tissue deformation validation with the use of glitter

The setup for the glitter experiments is the same as with the screw experiment. The only change is the phantom. This time, the phantom is created out of 10% wt gelatin with 33.3% cleaning vinegar and 66.6% water. First, half of the phantom is poured with nothing in it and set in the fridge overnight. Next, the glitter is sprinkled over the hardened half of the phantom. Next, the second layer of gelatin is poured and hardened overnight in the fridge. Resulting in figure 4.7.

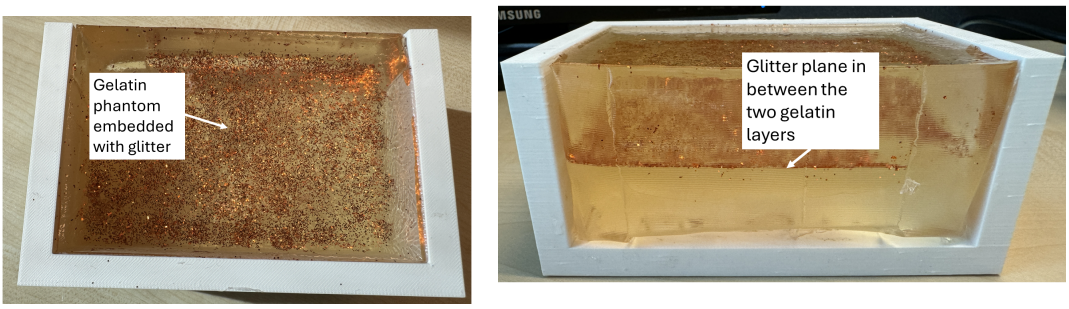

Figure 4.7: Left: Phantom with embedded glitter from above. Right: phantom with embedded glitter from the front.

4.2 Experimental protocol

4.2.1 Force validation

During the design phase of the experimental protocols, it was important to distinguish between constant parameters and the parameters that needed to be evaluated. For a short overview, see table 4.1

Variables	Constant Values
Friction coefficient	Insertion velocity
Cutting force	Needle dimensions
Young's Modulus	Phantom dimensions
Poisson's ratio	Phantom properties

Table 4.1: Variables and constant values during the experiments.

For the measurement of the friction coefficient and cutting force, 6 needle runs were done at 4 different speeds:

- 0.01 Hz -> 2.5 mm/sec
- 0.0075 Hz -> 3.33 mm/sec
- 0.005 Hz -> 5 mm/sec
- 0.0025 Hz -> 10 mm/sec

The first three runs, so-called dry runs, are used to calculate the design forces. A dry run means that the needle is moving up and down with no phantom. In this case, the measured forces are the friction forces of the needle pushing through a small hole to minimize bending and the clamp force due to the needle being held by a clamp joint. The last three runs, needle insertions into the phantom, are used to find all the necessary parameters. After every insertion, the phantom was slightly re-positioned to prevent repetitive testing in the same area. Next, the data was stored in a .mat file and a separate Matlab script was used to filter the dry run forces out of the measured phantom forces.
To find the Young's modulus and Poisson's ratio, it was determined with the laboratory technician that since the specifics of the phantom are known the values can be found in literature.
The density can be found by weighing the phantom and knowing its volume.

4.2.2 Needle deflection and tissue deformation validation

During these experiments, two values need to be evaluated: the needle deflection and the tissue deformation. This will be achieved by performing 3 insertions into the phantom at a speed of 3 mm/sec (0.008494 Hz). It is important that the screws/glitters are in the same plane as the needle, along with the bevel tip of the needle being positioned in a way that the needle deflects upwards. All of that is to make sure that the deflection and deformation are in the 2D plane that is used in the simulation and visible to the camera. The whole insertion will be filmed and stored. With the use of Matlab, the movement of the needle and screws/glitters can be tracked over time and compared with the results of the simulation. Note that the phantom isn't re-positioned after every insertion for the screws because the needle needs to stay in the same plane as the screws. After an insertion into the phantom, a cavity is formed. To ensure that the phantom relaxed to its original form and the pre-made cavity closed, sufficient time was allowed between each experiment. This resulted in no big differences in measured forces or deformation between the iterations. In the glitter experiments, the phantom was re-positioned after each insertion. This was possible because the needle could be inserted into the whole phantom as long as the needle was in the same plane as the glitter.

A final experiment is conducted in which a needle is inserted three times into the glitter phantom at a speed of 10 mm/sec. The results of these iterations are used to see the effect of velocity on deformation.

5 Results

The results will again be split up into two sections: the characterization of the input variables of the model and the validation of the output variables of the model.

5.1 Simulation input characterization

Before measuring the wanted tip and friction force, it is important to isolate any other force that is present in the setup. This procedure involved conducting 3 dry runs prior to the measurements with a phantom. The objective was to measure the forces that the needle was exposed to without the phantom. An example of the graphs can be seen in figure 5.1 which shows the forces of a dry run at 2.5 mm/sec with a full insertion and retraction.

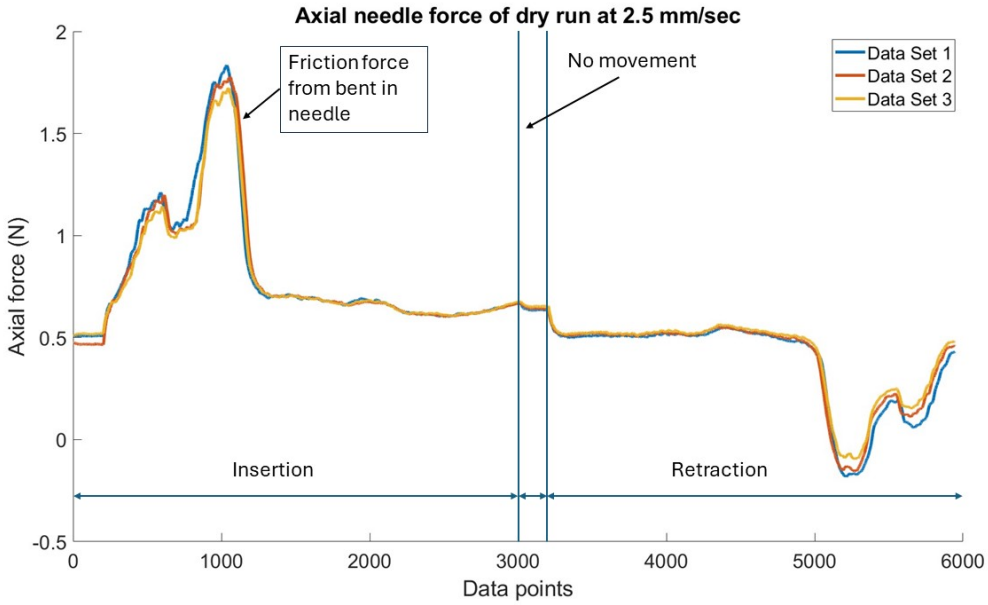

Figure 5.1: Measured forces of dry run at 2.5 mm/sec to detect the forces inside the setup. A full insertion and retraction is shown with a pause around 3000. During the insertion, the clear disturbance of the setup on the needle friction can be seen.

Up to point 3000, the needle is moving forward, followed by a stationary phase of the needle for about 2 seconds, followed by a retraction of the needle to its original starting position. There is a significant amount of friction force present within the setup. The force first goes up fast to a peak around 1.8 N. Next, it drops again and stays constant at around 0.6-0.7 N. At 3200 the needle starts moving back so we observe a drop in force and a peak the other way around can be seen.
The peaks can be explained because of the needle support in the setup. The needle is pushed through a really small hole, in the needle support, to prevent the needle from too much bending. Because the needle has a small bent, there is a lot of friction while pushing this bent through the small hole. The bent is at the tip of the needle which explains why there is a peak in the beginning and at the end of the measurement because this is the moment the bent goes through the needle support.
Since almost the same force curve is outputted every time, because the needle follows the same exact movement, the measured friction force in the setup can be subtracted from the measured force with the phantom. This will result in the isolated force of just the needle interaction with the phantom. As can be seen in figure 5.2, where the average dry run force is subtracted from

the 3 dry run measurements at 2.5 mm/sec, the forces fluctuate around zero. Table 5.1 shows the standard deviations from zero for all subtractions at all speeds, indicating that this way of filtering out the setup-induced forces from the total measured forces is valid.

Table 5.1: Standard deviation (STD) from zero, for all dry run measurements, at all speeds.

Velocity	STD Measurement 1 (N)	STD Measurement 2 (N)	STD Measurement 3 (N)
2.5 mm/sec	0.03	0.0201	0.00224
3.33 mm/sec	0.0054	0.0057	0.0105
5 mm/sec	0.0042	0.0157	0.0129
10 mm/sec	0.0139	0.0125	0.0129

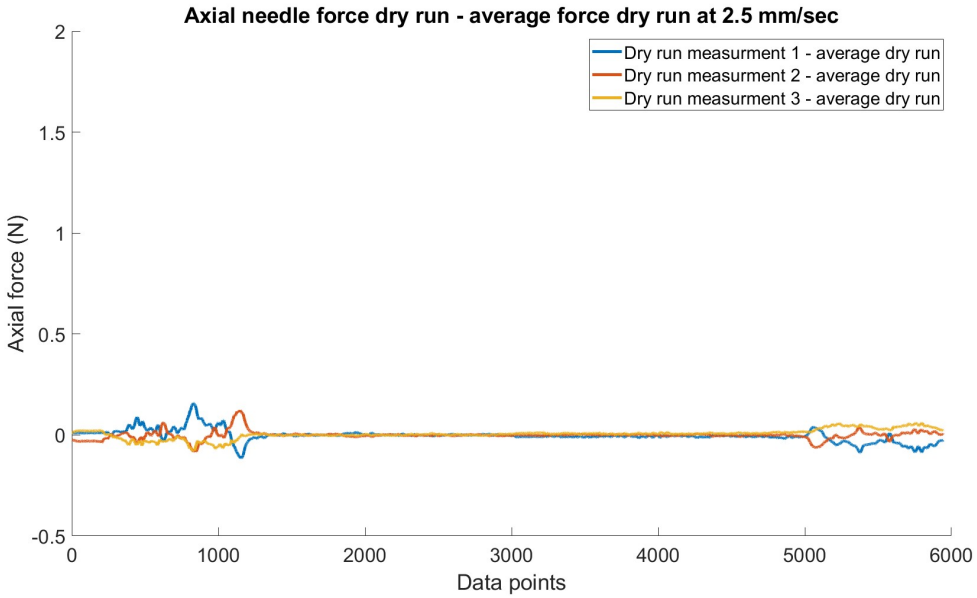

Figure 5.2: Subtraction of the average dry run force graph from the 3 measured dry run forces at 2.5 mm/sec.

In both figures 5.1 and 5.2, the insertion and retraction have been shown but in the future, there is only interest in the insertion so the retraction part will be left out for all following graphs.

Next for every speed, 3 insertions into the phantom have been conducted which resulted in the following curves for 2.5 mm/sec (see figure 5.3).

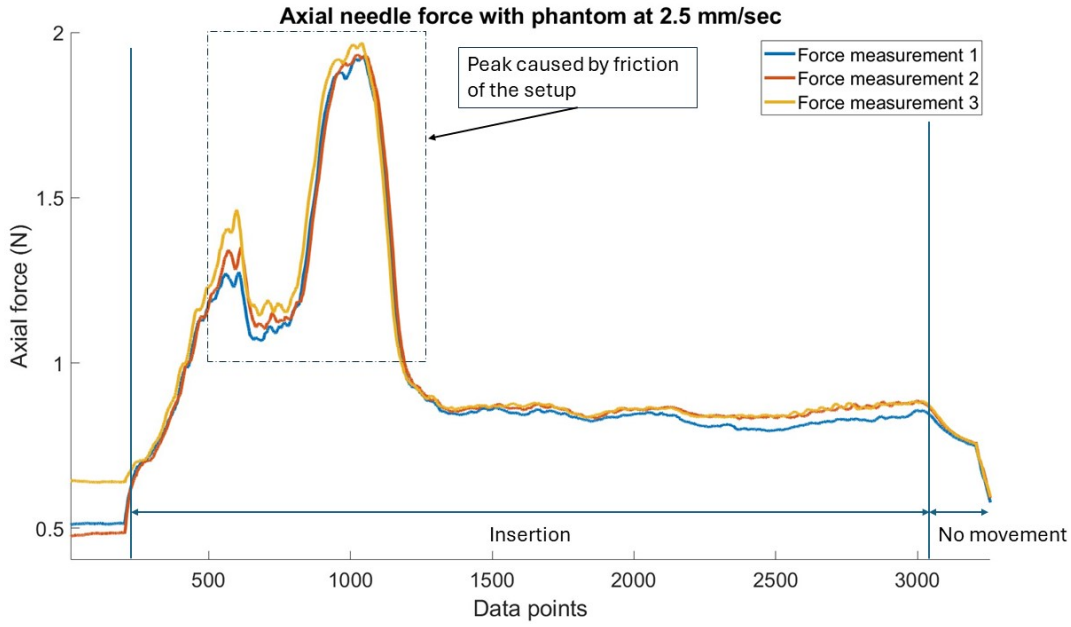

Figure 5.3: Measured total forces of only insertion into a phantom at 2.5 mm/s. The peak caused by the bent in the setup can be seen clearly at 1100.

This figure shows the total measured force when doing an insertion run through the phantom. But, since $f_{\text{measured}} = f_{\text{dryrun}} + f_{\text{friction}} + f_{\text{cutting}}$ the dry run forces need to be removed from the measured force by subtracting the average axial dry run force form the axial measured total force resulting in figure 5.4 for 2.5 mm/sec.

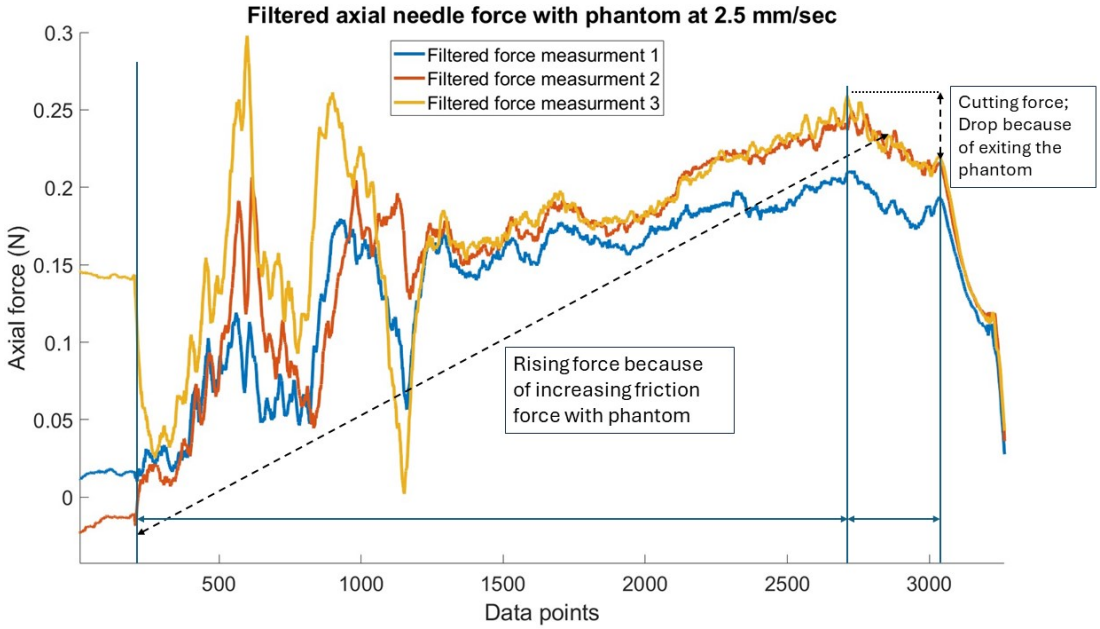

Figure 5.4: Total force measured minus the average dry run force at 2.5 mm/sec. From this figure, the rise in axial force, due to the friction being dependent on insertion depth, and cutting force can be clearly seen.

Although this figure still shows some effects of the setup forces, they are small. The remaining

forces can be attributed to the friction and cutting force of the needle on the phantom, which can be used to calculate the friction coefficient and cutting force at 3 mm/sec. After obtaining the filtered phantom force graphs at every speed, the next step was to find the cutting force and friction coefficient. This was done manually and the results can be seen in table 5.2 and 5.3.

speed (mm/s)	Cutting force 1 (N)	Cutting force 2 (N)	Cutting force 3 (N)	Average cutting force (N)
2.5	0.058	0.040	0.027	0.042
3.33	0.043	0.043	0.048	0.044
5	0.059	0.042	0.064	0.055
10	0.038	0.068	0.064	0.057

Table 5.2: Cutting forces at 2.5/3.33/5 and 10 mm/sec insertion speed.

It is shown by the results from the experiments that cutting force increases slightly with insertion speed. With the use of interpolation, it is possible to calculate the cutting force at an insertion speed of 3 mm/sec, which resulted in 0.04335 N at a speed of 3 mm/sec. In literature, the effect of velocity on cutting force is still inconclusive but for this study, our own findings will be used (18).

speed (mm/sec)	FrictionC (N s/mm^2) 1	FrictionC 2 (N s/mm^2)	FrictionC 3 (N s/mm^2)
2.5	0.00165	0.00177	0.00141
3.33	0.00235	0.00203	0.00231
5	0.0018	0.00153	0.0015
10	0.0012	0.00076	0.010

Table 5.3: Friction Coefficients at every speed. The friction coefficients are calculated by dividing the difference in force, between start of insertion and exiting the phantom, by the travelled distance and the insertion speed.

To find the dynamic friction and damping coefficient, the results of all measurements except the third one at 10 mm/sec have been used. As can be seen in table 5.3, this measurement is an outlier and needs to be excluded in the calculations. Next, the damping coefficient and dynamic friction can be calculated twice. Once using 2.5 mm/sec and 3.33 mm/sec and once using 5 mm/sec and 10 mm/sec. This gave the following equations:

$$F_{\text{measured}} = F_{\text{cutting}} + l(C_p + b_p \cdot \dot{z}) \tag{5.1}$$

$$0.244 = 0.042 + 0.055(C_p + b_p \cdot 0.0025) \tag{5.2}$$

$$0.261 = 0.044 + 0.055(C_p + b_p \cdot 0.00333) \tag{5.3}$$

$$0.382 = 0.0549 + 0.055(C_p + b_p \cdot 0.005) \tag{5.4}$$

$$0.501 = 0.106 + 0.055(C_p + b_p \cdot 0.01) \tag{5.5}$$

If equation 5.2 and 5.3 are solved simultaneously a dynamic friction of 2.86285 N/m and a damping coefficient of 324.768 Ns/m^2 are found. If equation 5.4 and 5.5 are solved simultaneously, a dynamic friction of 4.718692 N/m and a damping coefficient of 245.338 Ns/m^2 are found. These two are averaged together to give a dynamic friction of 3.791 N/m and a damping coefficient of 285.053 Ns/m^2.
The Young's modulus found in literature is 30.74 kPa according to a study done by Rippy *et al.* (34). In this study, the young's modulus has been found using ultrasound elastography, optical coherence elastography and uniaxial testing. The average of all measurements used in this paper has been used. The Poisson's ratio is 0.422 according to a study done by Otterloo *et al.* (32). The density of the phantom equals $\frac{0.489}{0.120 \times 0.080 \times 0.055} = 636.71875\ Kg/m^3$.

5.2 Water vs Cleaning vinegar validation

An additional experiment has been conducted to test the difference between using 100% water or 66.6% water and 33.3% cleaning vinegar when building the gelatin phantom. In addition, during this experiment, a pause has been introduced after the needle exits the phantom and moves further after 5 seconds. This is to isolate the friction force and validate the found cutting and friction forces. This gave the following result at 2.5mm/sec:

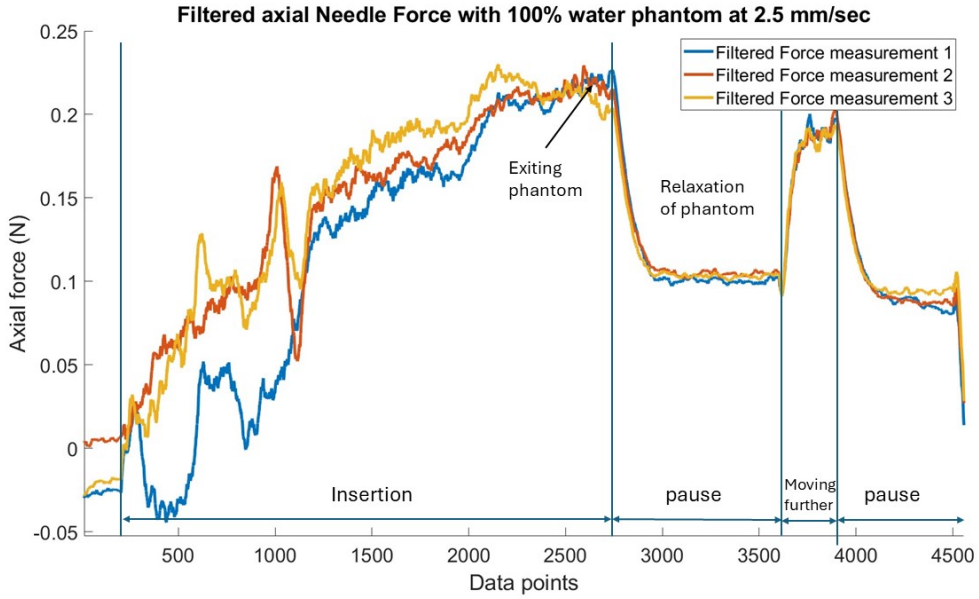

Figure 5.5: Axial needle force minus average dry run force of a needle insertion in a 100% water phantom with 10% wt gelatin at 2.5mm/sec. The pause and moving further phase are clearly visible.

When figure 5.5 is compared with figure 5.4, it can be observed that the force in both cases initially rises to around 0.25 N and next decreases to approximately 0.1 N. This behaviour and magnitude range are the same as with the cleaning vinegar, which indicates that the cleaning vinegar has no effect on the structure of the gelatin and won't affect the friction and cutting force. The pause was introduced to make sure the phantom was totally relaxed after the needle exited the phantom and the next movement was purely friction force. This figure confirms that the cutting force is really low and the friction force at full insertion depth is around 0.19 N.

5.3 Simulation output

With the use of the output from the force validation experiments, it is possible to run the simulation. This produces the following results after a full insertion of 60 mm (see figure 5.6).

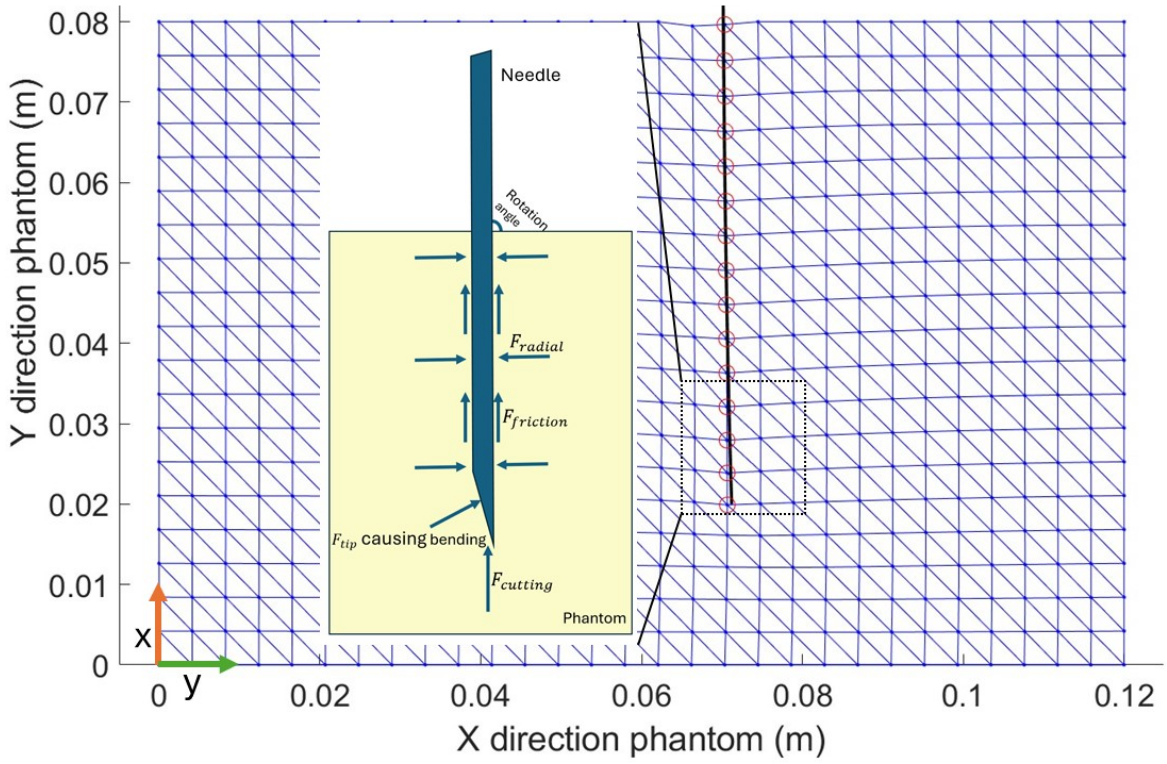

Figure 5.6: 60 mm insertion into 2D liver mimicking homogeneous tissue with experimentally determined input variables.

The deformation of the phantom tissue in the simulation seems to be really small. This is caused by the cutting and friction force from the experiments also being really small. It is important to keep in mind that the experiments aren't used to simulate a real insertion into a liver but to validate that the model gives the same result as the experimental output when the same input parameters are used.
To show that the model is also able to predict realistic tissue deformation and needle deflection within a higher stiffness material, a model with more realistic forces (see figure 5.7) is made with the input parameters from table 3.1 and 3.2. The figure shows a full insertion of 60 mm into homogeneous liver tissue. In the upper right corner, the forces are shown real-time during the insertion. Due to the larger forces present in this model, the deformation and deflection are also larger.

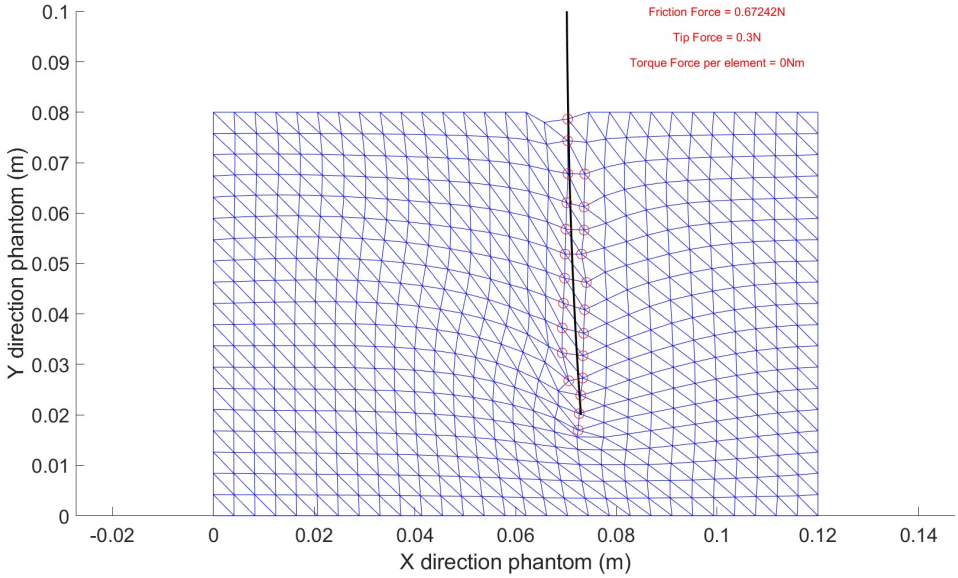

Figure 5.7: 60 mm insertion into 2D liver mimicking homogeneous tissue with input variables found in literature.

The result of two additional movements possible in the model are shown in figure 5.8. The needle is inserted under an angle of 60 degrees and the needle is rotated 10 degrees while inserted 1.2 cm inside the tissue. 10 degrees is quite a large rotation but this is used to make the tissue deformation visible in extreme cases.

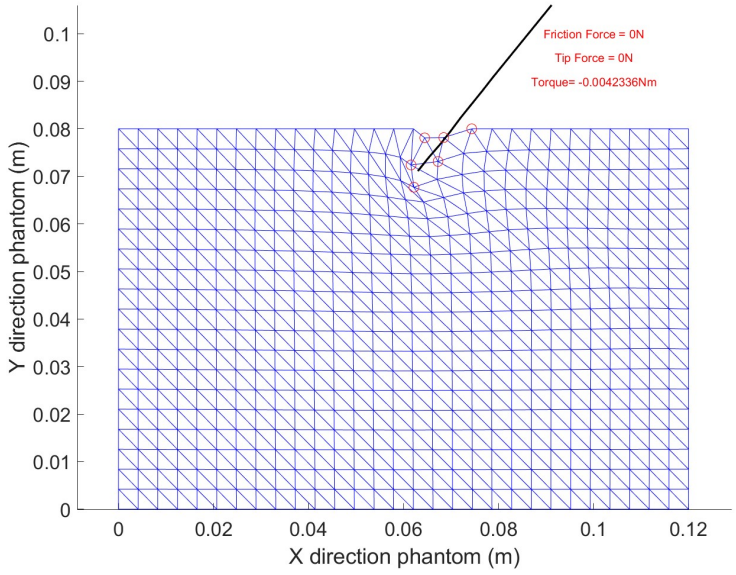

Figure 5.8: 12 mm insertion into 2D liver mimicking homogeneous tissue under an angle of 60 degrees. After the insertion of 12 mm, the needle is rotated 10 degrees to show the deformation around the needle.

The tissue deformation resulting from a rotation of 10 degrees appears quite large but not unrealistic. The tissue on the left side of the needle is compressed and on the right side, it

is stretched. This model shows promising and interesting results since this method of doing biopsies to steer the needle to align with the target tumour is often used by surgeons.

5.4 Simulation output validation screw nodes

During the experiments, to validate the simulation output, the needle was inserted into the phantom with embedded screws 3 times. Figure 5.9 shows a close-up of the needle inside the phantom after a full insertion. With the use of the Lucas-Kanade algorithm, four screws are traced over time. Meanwhile, the change in the y location of the needle tip is calculated between the first and last frame to calculate the deflection.

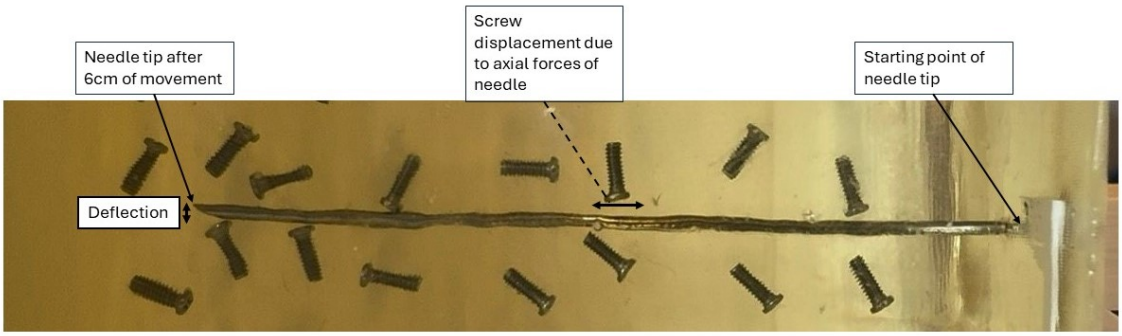

Figure 5.9: Full insertion into the gelatin phantom with embedded screws. This figure shows the deflection of the needle tip from its starting point, together with the deformation of the screws.

The simulation predicted a needle deflection of 1.200 mm. Meanwhile, the experimental needle deflections were 1.353 mm, 1.005 mm and 1.545 mm, with an average deflection of 1.301 mm with a standard deviation of 0.274 mm. The simulation prediction differed 0.101 mm (7.8 %) from the experimentally found deflection.
The 4 points in the experimental data that correspond the most with the node placement in the simulation, are chosen to be tracked over time and can be seen in figure 5.10 and 5.11.

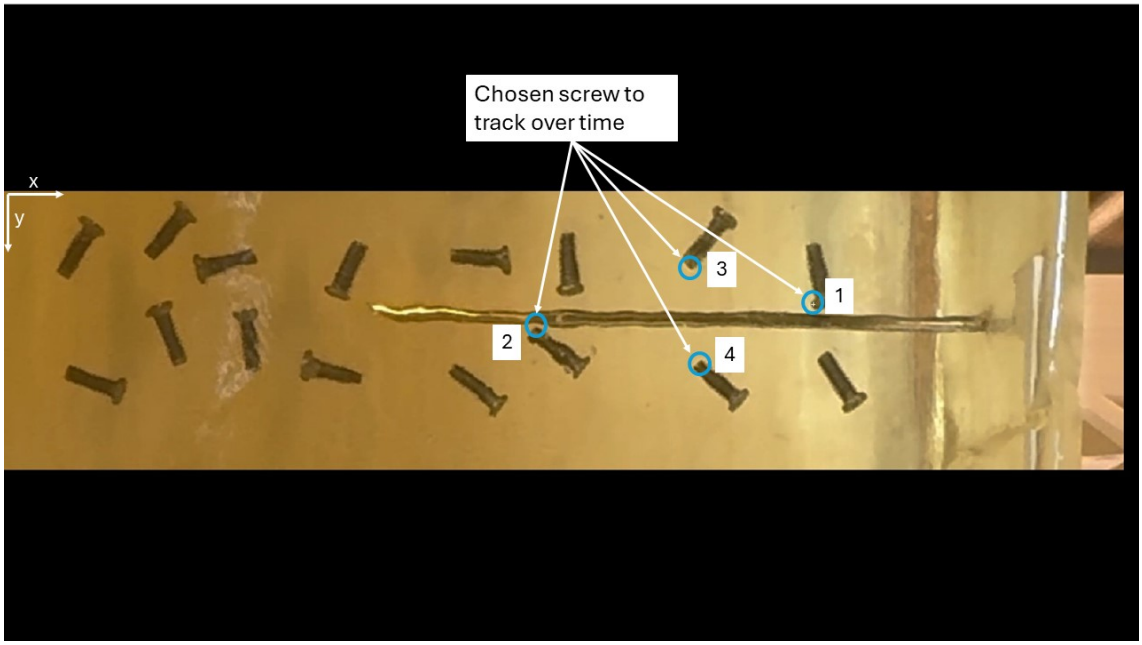

Figure 5.10: The 4 chosen screws that correspond most with the nodes in the simulation.

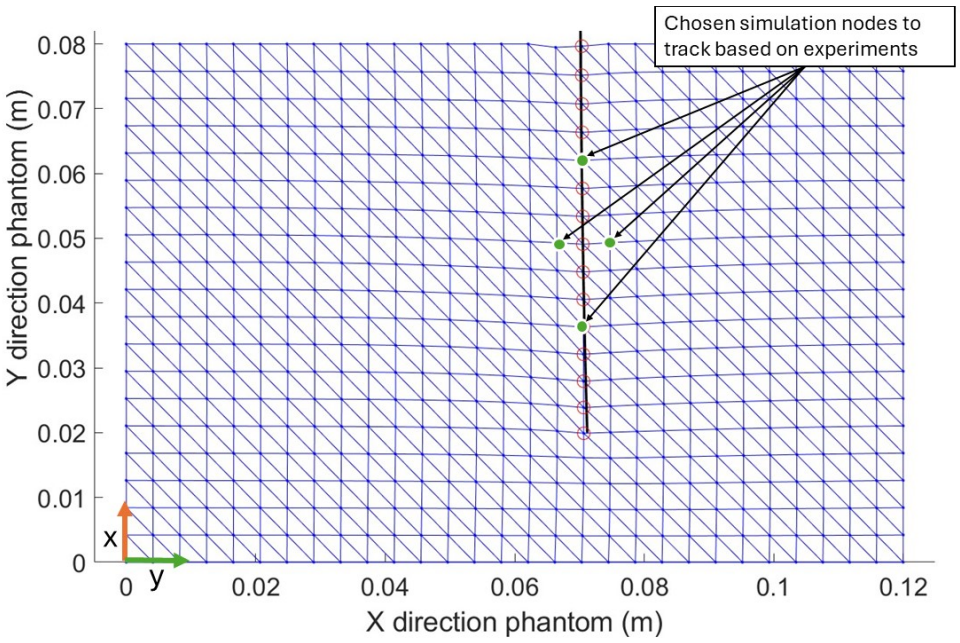

Figure 5.11: The 4 nodes in the simulation that correspond with the 4 screws in the experimental phantom.

The next step is to track the x- and y-displacement over time for both the screws and the simulation nodes. Figure 5.12 shows the change in x- and y- coordinates in millimetres, after pixel to mm conversion, of screw 1. Figure 5.13 shows the change in x- and y- coordinates in mm of the simulation of node 1.

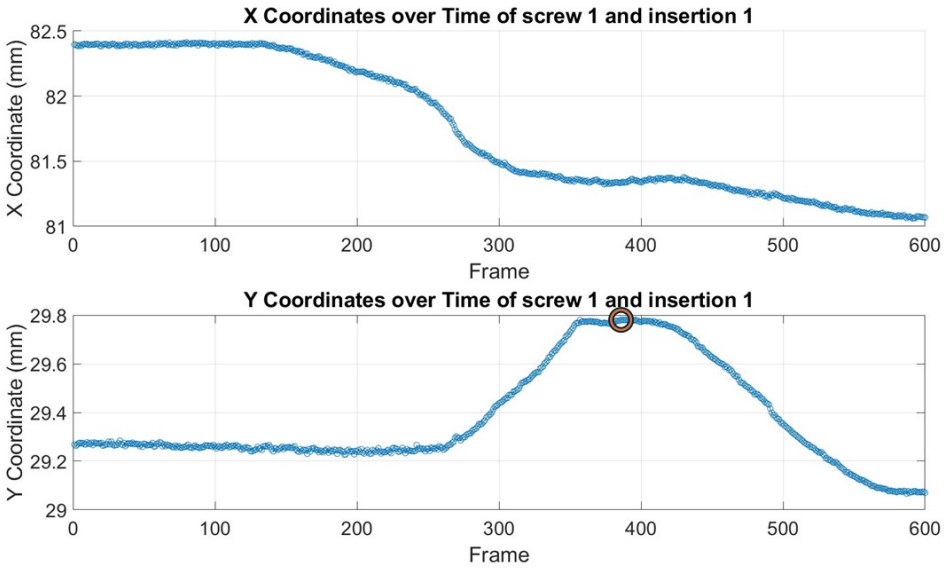

Figure 5.12: X- and Y- displacement over time of screw 1 embedded in gelatin with a needle insertion speed of 3 mm/sec.

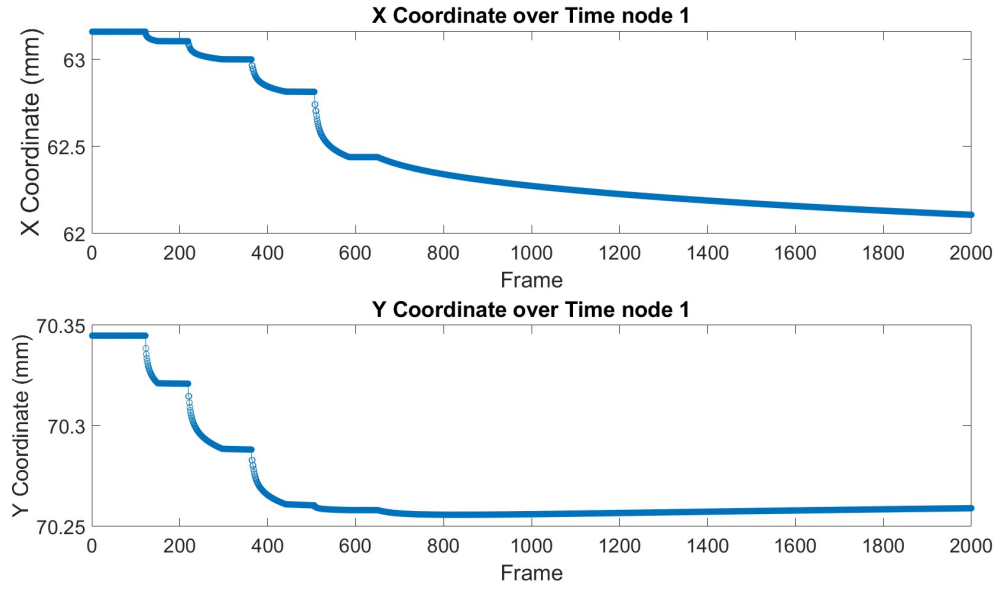

Figure 5.13: X- and Y- displacement over time of node 1 in the simulation with a needle insertion speed of 3 mm/sec.

It is important to keep in mind that the movement of the needle past the first node and screw is not exactly at the same time. These plots are used to check whether the nodes and screws deform the same way. The first big difference that can be seen is in the smoothness of the screw movement compared to the node in the model. The second big difference is the relaxation in the y- direction of the screw compared to the simulation node. In the simulation, the relaxation after the needle passes isn't modelled. This is why in the simulation, the y-coordinate is almost constant after the needle tip passes. In the experiments, the screws first move towards the needle and after the needle tip passes, it relaxes away from the needle. The deformation of the simulation is compared with the movement of the screws towards the needle and not the

total movement (up to the orange circle in figure 5.12). Table 5.4 shows the deformation of the 4 screws in the three experiments together with the average, the standard deviation and the percentage of difference with the simulation results at an insertion speed of 3 mm/sec. Table 5.5 shows the deformation of the same 4 nodes in the simulation.

	Node	Exp 1	Exp 2	Exp 3	Average	STD	diff (mm (%))
X deformation (mm)	1	1.260	1.191	1.637	1.363	0.299	0.312 (22.9)
X deformation (mm)	2	1.078	1.160	1.445	1.228	0.193	0.24 (19.5)
X deformation (mm)	3	0.830	0.779	1.068	0.892	0.155	0.206 (23.1)
X deformation (mm)	4	0.881	0.900	1.085	0.955	0.113	0.163 (14.6)
Y deformation (mm)	1	0.502	0.323	0.476	0.434	0.097	0.348 (79.5)
Y deformation (mm)	2	0.386	0.774	0.792	0.650	0.229	0.103 (48.9)
Y deformation (mm)	3	0.176	0.184	0.259	0.206	0.045	0.033 (13.8)
Y deformation (mm)	4	0.779	0.186	0.716	0.697	0.092	0.403 (57.8)

Table 5.4: X-deformation and Y-deformation of the 4 nodes for all 3 experiments. The average column shows the average of the deformations of the 3 experiments and the STD shows the standard deviation.

	Node	Simulation		Node	Simulation
X deformation (mm)	1	1.051	Y deformation (mm)	1	0.086
X deformation (mm)	2	1.468	Y deformation (mm)	2	0.332
X deformation (mm)	3	1.098	Y deformation (mm)	3	0.239
X deformation (mm)	4	1.118	Y deformation (mm)	4	0.294

Table 5.5: X-deformation and Y-deformation of the 4 nodes in the simulation.

These tables indicate that the deformation from the simulation doesn't differ too much from the experimentally determined deformation in the x-direction. In the y-direction, the results sometimes differ up to almost 79.5%. This big difference may be caused by the size of the screws restricting the movement and the nodes not corresponding exactly with the simulation nodes.

5.5 Simulation output validation glitter nodes

During the experiments, to validate the simulation output, the needle was inserted into the phantom with embedded glitter 3 times at 3 mm/sec. Figure 5.14 shows a close-up of the needle inside the phantom after a full insertion. With the use of the Lucas-Kanade algorithm, four nodes are traced over time. In these nodes, 3-4 glitters are traced and the average is plotted over time to find the deformation in x- and y-direction. These nodes corresponds with the nodes from the simulation quite accurately and are shown in figure 5.11 and 5.15.

Figure 5.14: Fully inserted needle into a gelatin phantom with glitter.

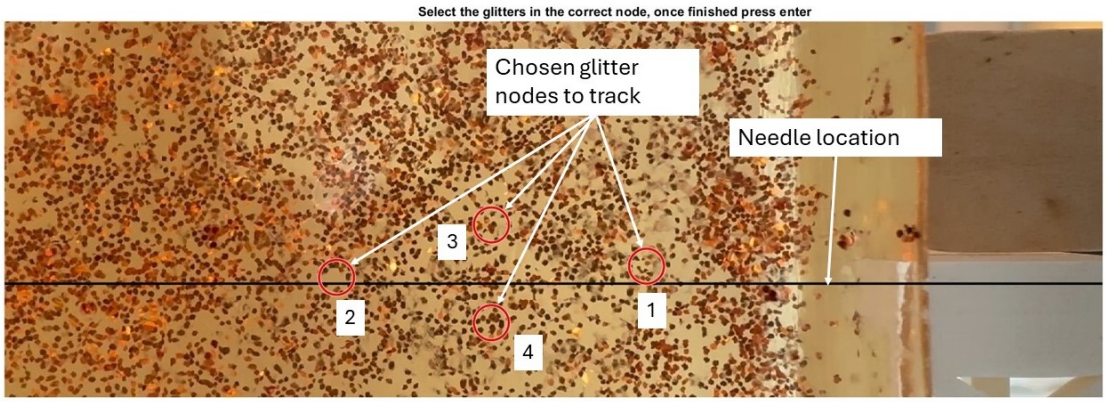

Figure 5.15: The 4 locations in the phantom where glitters are traced over time to find the deformation.

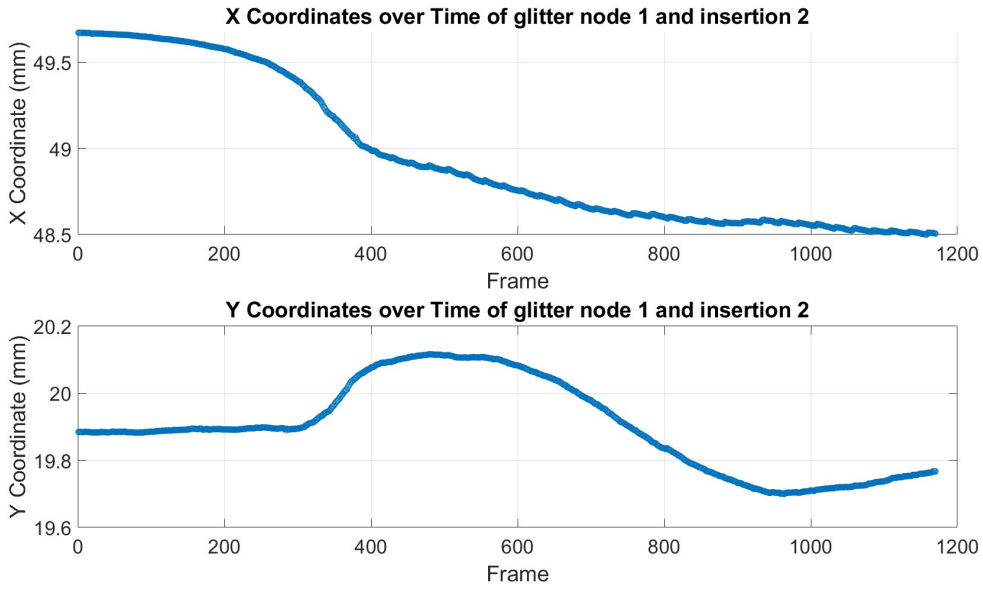

Figure 5.16: Average x- and y- displacement over time of 4 glitters in node 1. A full insertion into a gelatin phantom at a speed of 3 mm/sec is measured.

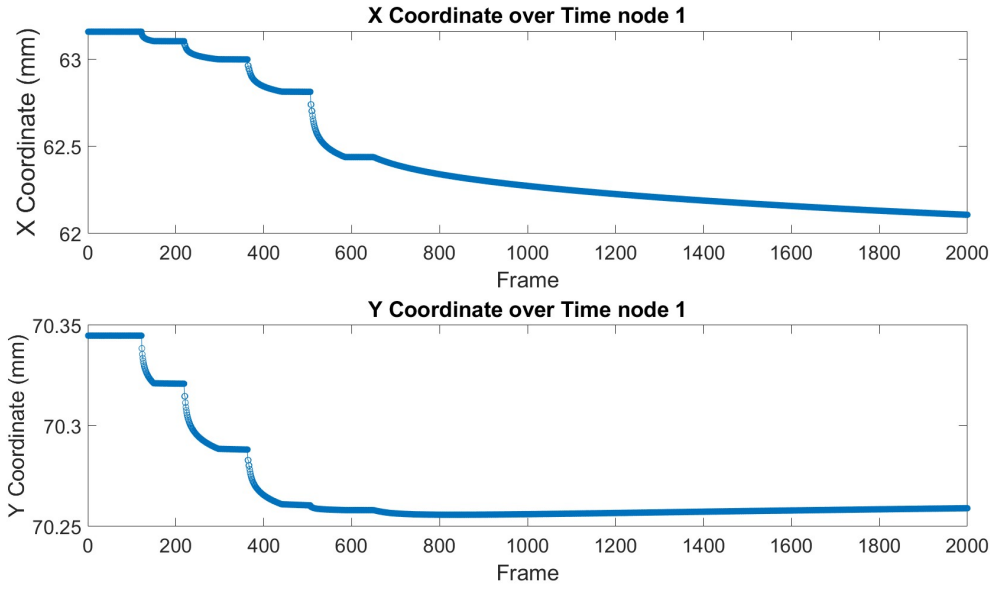

Figure 5.17: X- and Y- displacement over time of node 1 in the simulation with a needle insertion speed of 3 mm/sec.

As can be seen in figure 5.16 and 5.17, the deformation in the x-direction only differs in the smoothness of the movement. In the y-direction, the same difference can be seen as with the embedded screws. The glitter moves towards the needle and after a while it relaxes away from the needle. This is not modelled in the simulation so the y-coordinate stays constant after moving towards the needle. The following table shows the total deformation in the x- and y-direction and can be compared with the results in table 5.5.

	Node	Exp 1	Exp 2	Exp 3	Average	Std	% diff
x deformation (mm)	1	1.456	1.662	1.227	1.448	0.218	0.397 (27.4)
x deformation (mm)	2	1.678	1.253	1.141	1.448	0.283	0.02 (1.4)
x deformation (mm)	3	0.931	0.836	0.742	0.842	0.095	0.256 (30.4)
x deformation (mm)	4	0.878	0.853	0.787	0.839	0.047	0.279 (33.3)
y deformation (mm)	1	0.049	0.231	0.213	0.164	0.1	0.078 (47.6)
y deformation (mm)	2	0.733	0.397	0.447	0.526	0.181	0.194 (36.9)
y deformation (mm)	3	0.076	0.036	0.046	0.053	0.021	0.186 (350.9)
y deformation (mm)	4	0.380	0.313	0.275	0.323	0.053	0.029 (9)

Table 5.6: X- and y-deformation of the 4 glitter locations for all 3 experiments. The average of the 3 experiments is shown together with the standard deviation. Finally, the last column shows the difference with the simulation output in percentage.

The results from the simulation in the x-direction are really accurate compared to the results of the glitter experiments. In the y-direction, there is a larger difference in deformation between the simulation and the experiments in node 3. The differences of the other nodes are still within the usable limits but the modelled movement in the y-direction requires some more attention. The deformation observed in the screw experiment showed almost the same movement pattern as that of the glitter phantom. However, the magnitude of deformation of the measured nodes was greater in the glitter experiment. This difference can be attributed to the screws being significantly bigger than the glitter particles. The larger screws interfere with the gelatin movement more than the glitter particles. The part of the screw closer to the needle may be dragged along but due to the top of the screw being stuck in less moving gelatin, the movement is obstructed. Consequently, the results from the glitter experiments, which show less obstructed motion and a more realistic response to the needle insertion, provide a more accurate representation of the tissue deformation.

5.6 Glitter deformation output at 10 mm/sec

One last experiment was conducted to find the deformation in the x- and y-direction at 10 mm/sec. This experiment is used to find the effect of speed on the deformation. Table 5.7 shows an overview of the deformation in the x- and y-direction of 3 insertions into a 10 % wt gelatin phantom. The movement of the first node can be seen in figure 5.18. This is approximately the same as the movement of node 1 at 3 mm/sec only the magnitude is smaller. This can be clearly seen in table 5.7 when compared with the results from table 5.4.

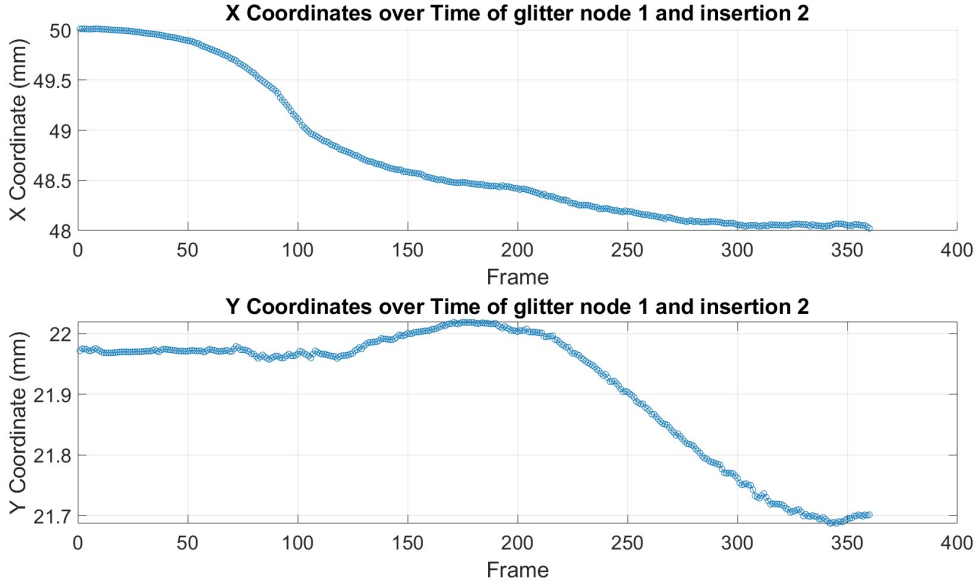

Figure 5.18: Average x- and y- displacement of 4 glitters in node 1. A full insertion into a gelatin phantom at a speed of 10 mm/sec is measured.

	Node	Exp 1	Exp 2	Exp 3	Average	Std	% Diff
x deformation (mm)	1	1.784	1.989	1.223	1.665	0.397	0.449 (27)
x deformation (mm)	2	1.477	1.761	1.773	1.670	0.168	0.028 (1.7)
x deformation (mm)	3	1.382	1.165	0.83	1.126	0.278	0.138 (12.3)
x deformation (mm)	4	0.932	1.013	1.361	1.102	0.228	0.2 (18.1)
y deformation (mm)	1	0.113	0.046	0.028	0.062	0.045	0.019 (30.6)
y deformation (mm)	2	0.321	0.353	0.188	0.287	0.088	0.026 (9.1)
y deformation (mm)	3	0.051	0.08	0.06	0.074	0.015	0.185 (170.3)
y deformation (mm)	4	0.164	0.267	0.325	0.252	0.082	0.051 (20.2)

Table 5.7: X- and y-deformation of the 4 glitter locations for all 3 experiments with an insertion speed of 10 mm/sec into a 10% wt gelatin phantom. The deformations of all three experiment along with the average over the three experiments are shown. The last two columns show the standard deviation and the difference between the simulation and experiments in percentage.

	Node	Simulation		Node	Simulation
X deformation (mm)	1	1.216	Y deformation (mm)	1	0.081
X deformation (mm)	2	1.698	Y deformation (mm)	2	0.313
X deformation (mm)	3	1.264	Y deformation (mm)	3	0.200
X deformation (mm)	4	1.302	Y deformation (mm)	4	0.303

Table 5.8: X-deformation and Y-deformation of the 4 nodes in the simulation with an insertion speed of 10 mm/sec.

The experimental results show that as velocity increases, the deformation decreases, which is in line with literature (26) (5). The final column of table 5.7 presents the difference with the simulation results from table 5.8. These differences are quite substantial. The primary reason for this is that in the simulation, input forces rise with velocity, leading to higher deformation. However, in real-life, deformation decreases with increasing velocity, resulting in significant differences. Literature supports the increase in friction force when the velocity increases (18). For cutting force literature is still inconclusive about the effect of velocity (18). In this study, cutting force shows a slight increase with velocity, which has been incorporated into the simulation.

6 Discussion

In this study, a model is created to predict needle deflection and tissue deformation with a sub-millimeter precision. Interaction forces in the form of cutting, friction and torque can be shown real time based on the four different needle movements. This section will highlight the possible reasons behind the difference between the experimental and simulation output.

6.1 Force validation

The experimental forces collected in this study differ from the expectations from literature. Literature indicates that the force required to penetrate through a real liver or a liver-mimicking phantom is significantly higher than the forces measured in this study. While literature often reports forces in a range of 1-2 N, the experiments in this study only measured forces from 0.02-0.4 N. This study already demonstrated that the cleaning vinegar, used in this study, does not affect phantom properties and measured forces. It is possible that while gelatin mimics the young's modulus of the human liver closely, the frictional component of gelatin is too low to mimic a real liver. It is important to note that this study aimed to develop a model that provides realistic values given a specific input data set, which in this case is achieved.
Additionally, some high outliers, in force, were observed in the measurements. These peaks were attributed to the friction forces from the setup. An extra experiment was conducted, in which the hole of the needle support was widened, showing that these peaks do not affect the measured friction and cutting force. Due to the increase of the hole in the needle support, the needle deflection increased. Filtering was done using a dry run before every measurement to subtract the measured "setup forces" from the total measured forces with the phantom. This could result in a slight loss of accuracy.

6.2 Simulation output validation

The low deformation and deflection output of the simulation was expected due to the input force being low. To further validate these findings, a phantom with embedded screws was constructed. However, achieving high accuracy during this process was challenging. The screws were placed with a set of tweezers and a calliper, but manually placing the screws 4 mm apart along the needle's insertion path was a challenging task and reduced the accuracy. After the screws were placed and the second layer of hot gelatin was poured, the screws started to move slightly due to the melting of the gelatin that was supposed to hold them. although the screws are still all in the same plane, this shifting reduces the accuracy.
The simulation output could differ from the experimentally found results due to the fact that the Young's modulus and Poisson's ratio are found in literature due to the unavailability of the necessary equipment to do this experimentally. These values might not be accurate due to the phantoms not having the exact same temperature or not exactly the same building process. These variables have a lot of impact on the output of the simulation and for future work, it would be better to measure these variables with higher precision.
Additionally, the Lucas-Kanade algorithm used for screw tracking might sometimes have a hard time tracking the exact same point of the screws/glitter, because they are very small, behind gelatin and after the zoom in the resolution is a bit lower. This issue was greater with increasing insertion speed. This could result in some difference in the tracked output and the real output which could influence the deformation findings.
This study made use of insertion into the gelatin phantom with embedded screws to validate tissue deformation and needle deflection. The second and third insertion into the phantom with embedded screws is done in the same location as the first one due to the fact that the needle needs to stay in the exact same plane as the screws. This could result in the needle mov-

ing through a pre-made cavity and result in slightly lower axial interaction forces. This could reduce the deformation of the screws and deflection of the needle and consequently affect the results.
The glitter experiments allowed for the most optimal movement of the gelatin and consequently showed the most realistic movement. However, there is still a notable difference between the simulation and the experimentally collected data. In the x-direction, the average difference is around 23.1%. This difference is likely due to inaccuracies during the experiments or interaction forces. The difference in the y-direction is caused by some different problems. Modelling deformation in the y-direction is more complex due to the various forces having an effect along with the significant role of tissue relaxation, which is currently not modelled. On the bevel tip side of the needle, the forces include a cutting force pushing the nodes away and a friction force pulling the nodes towards the needle. Conversely, on the other side of the needle, the nodes are pulled because they are coupled to the nodes that get affected by the cutting force and friction force pulls the nodes towards the needle. Specifically for node 3, the substantial difference is probably caused by the node being pulled too hard towards the needle in the simulation. This occurs because of the cutting force pushing nodes under the needle, thus pulling node 3 towards the needle, and friction force pulling the node towards the needle. The distance travelled by the nodes, based on the force applied, depends on the stiffness. The increased stiffness around the needle is currently modelled as an area with an applied stiffness factor. This threshold and stiffening factor are derived from literature and calculations but do not take into account the complexity of this process. As a result, node 3 might not be stiff enough in the y-direction, allowing for too large movement. Further research is necessary to improve the modelling of these complex movements and accurately represent the stiffness variations around the needle.

7 Conclusions and Recommendations

7.1 Conclusions

The goal of this study was to answer the question on how tissue deformation and needle deflection can be modelled to accurately estimate the deflections and deformations in a liver-mimicking phantom? In this study, a model has been developed, with the use of FEM, to predict tissue deformation and needle deflection based on an experimental model with a sub-millimetre accuracy. The experimentally determined friction and cutting force in this study, based on a 10% wt gelatin phantom (36), deviate from the findings in literature. Literature often showed friction forces between 1-2 N while this research showed forces between 0.02-0.4 N. The simulation output showed promising results while tested with experimentally validated input and literature-validated input. The model differed from the results of the screw experiment on average 20% in the x-direction and 50% in the y-direction. The model differed only 23.1% on average in the x-direction and 31.2% on average in the y-direction from the glitter phantom experiments, in which node 3 is used as an outlier. The needle deflection differed 0.101 mm (7.8%) from experimentally found needle deflection. Although the methods used in this study are still far away from clinical use, the model showed promising results to enhance the accuracy of haptic and visual real-time feedback to surgeons during liver biopsies.

7.2 Future work

Most importantly, it is important to repeat the experiments with higher quality equipment available. The Young's modulus and Poisson's ratio of the phantom need to be determined experimentally instead of using literature found values. Additionally, the needle setup of the axial force measurements needs a new needle without a bent to accurately measure the insertion forces. Finally, the forces in this simulation are modelled based on experimental values from a gelatin phantom. To get a really accurate simulation in-vivo experiments could help increase the realism of the force model. Since in-vivo could be quite challenging, because of the ethical approval, a lot of improvement can also be made by using a different phantom material like polyvinyl alcohol and changing the structure by implementing different parts with different stiffnesses (e.g. vessels, Glisson's capsule).
For the future of this study, it is important to close the gap between this study and implementation into clinical use. This means more focus on improving the realism of the model while keeping the computational complexity and thus the delay low. For example, this study did not model the relaxation of a tissue node in the y-direction after the needle has passed the node. To increase the realism of the model, it is good to add this kind of behaviour to the model. Important to note is that the deformation in the y-direction in both cases is very small and tracking errors might be present in some results.
A lot of research has already been conducted in the 2D FE models for predicting of needle-tissue interaction. While increasing the complexity, of for example the modelled tissue, the computational expensiveness of the simulation rises imposing a larger delay. Building a 3D model would also increase the computational expensiveness a lot and running an accurate 3D model real-time would be a challenge. For future research, it might be interesting to look into modelling the needle-tissue interaction in 3D with high complexity for generation of data sets. These data sets can be used to train a machine learning algorithm that is able to predict tissue deformation and needle deflection real-time because of the offline training (25).
As discussed in the literature review, another way of offline training would be Kriging-based modelling. A Kriging-based model is also trained offline using a limited data set and gains estimates of values over a continuous spatial field. Offline training is an interesting topic for

future research, because it creates the possibility to generate realistic complex models but, due to offline training, they can be run real-time.
The model implemented in this study is able to predict tissue deformation and needle deflection for a 2D, homogeneous mesh. For future research, it is interesting to look into extending the model to 3D while increasing the realism of the mesh by implementing different kinds of structures like blood vessels or the Glisson's capsule. This model focuses on the visual aspects of tissue deformation and needle deflection together with providing force feedback. Once the required realism is achieved, it is possible to provide the force feedback of the model back to the haptic handle that is left out in this study (see figure 7.1).

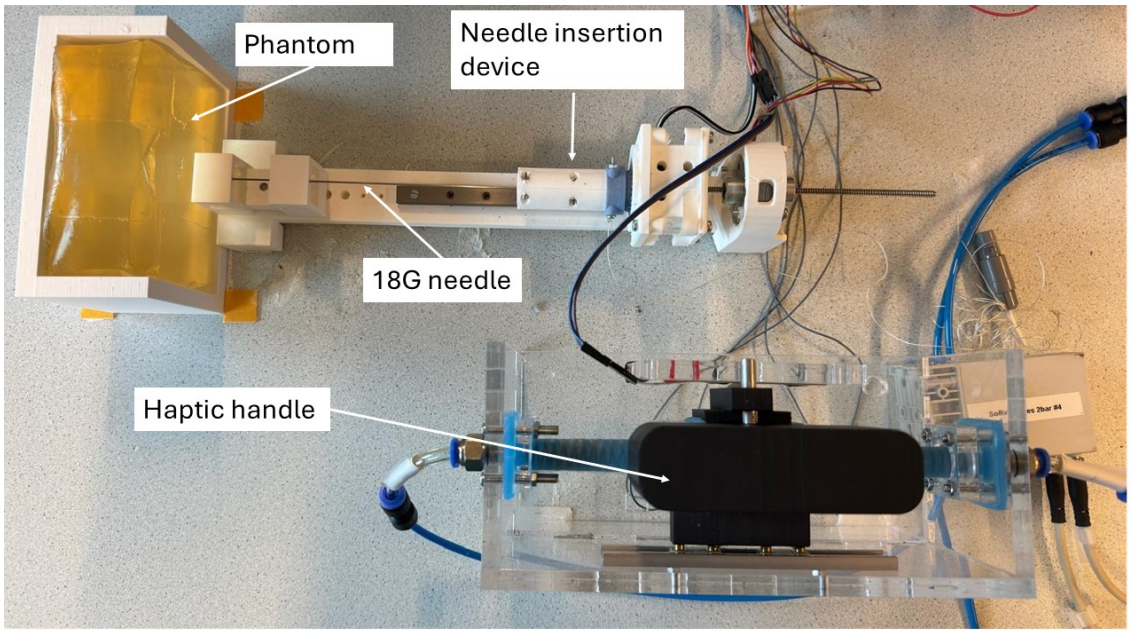

Figure 7.1: Setup with a haptic handle that could be used for haptic feedback in future research.

Meanwhile, this model could also be used for needle steering purposes. Due to the bevel-tipped needle which causes bending of the needle, it is possible to steer the needle using rotations based on a path planning method. This model could help visualise the needle deflection as feedback for the path planning method and calculate the tissue deformation to help minimize tissue trauma.

Bibliography

[1] (2022), Liver cancer statistics | World Cancer Research Fund International.
https://www.wcrf.org/cancer-trends/liver-cancer-statistics/

[2] (2024), Aurora Ready-to-Use Tools - NDI.
https://www.ndigital.com/electromagnetic-tracking-technology/aurora/aurora-tools/

[3] (2024), Linear Elastic Material.
https://doc.comsol.com/5.5/doc/com.comsol.help.sme/sme_ug_theory.06.23.html

[4] 4 (), Track points in video using Kanade-Lucas-Tomasi (KLT) algorithm - MATLAB - MathWorks Benelux - accessed 2023.
https://nl.mathworks.com/help/vision/ref/vision.pointtracker-system-object.html

[5] Aaboubout, Y., M. R. N. Soares, E. M. Barroso, L. C. van der Sar, A. Bocharnikov, I. Usenov, V. Artyushenko, P. J. Caspers, S. Koljenović, T. C. B. Schut, J. J. van den Dobbelsteen and G. J. Puppels (2021), Experimental study on needle insertion force to minimize tissue deformation in tongue tissue, *Medical Engineering Physics*, **vol. 97**, pp. 40–46, ISSN 1350-4533, doi:10.1016/J.MEDENGPHY.2021.10.003.

[6] Abayazid, M., G. J. Vrooijink, S. Patil, R. Alterovitz and S. Misra (2014), Experimental Evaluation of Ultrasound-Guided 3D Needle Steering in Biological Tissue, *International journal of computer assisted radiology and surgery*, **vol. 9**, pp. 931–939, ISSN 18616429, doi:10.1007/S11548-014-0987-Y.
https://www.ncbi.nlm.nih.gov/pmc/articles/PMC4382439/

[7] Abolhassani, N., R. Patel and M. Moallem (2007), Needle insertion into soft tissue: a survey, *Medical engineering physics*, **vol. 29**, pp. 413–431, ISSN 1350-4533, doi:10.1016/J.MEDENGPHY.2006.07.003.
https://pubmed.ncbi.nlm.nih.gov/16938481/

[8] Bao, Y. D., S. Q. Qu, D. B. Qi and W. Wei (2022), Investigation on puncture mechanical performance of tracheal tissue, *Journal of the Mechanical Behavior of Biomedical Materials*, **vol. 125**, ISSN 1751-6161, doi:10.1016/J.JMBBM.2021.104958.

[9] Bergholz, M., M. Ferle and B. M. Weber (2023), The benefits of haptic feedback in robot assisted surgery and their moderators: a meta-analysis, *Scientific Reports 2023 13:1*, **vol. 13**, pp. 1–15, ISSN 2045-2322, doi:10.1038/s41598-023-46641-8.
https://www.nature.com/articles/s41598-023-46641-8

[10] Bui, H. P., S. Tomar, S. Pierre, A. Bordas, P. Alain, H. P. Bui and P. A. Bordas (2018), Corotational cut finite element method for real-time surgical simulation: Application to needle insertion simulation, *Computer Methods in Applied Mechanics and Engineering*, p. 10, doi:10.1016/j.cma.2018.10.023Ãŕ.
https://hal.science/hal-01921631

[11] Carriere, J., M. Khadem, C. Rossa, N. Usmani, R. Sloboda and M. Tavakoli (2019), Event-Triggered 3D Needle Control Using a Reduced-Order Computationally Efficient Bicycle Model in a Constrained Optimization Framework, *Journal of Medical Robotics Research*, **vol. 4**, ISSN 24249068, doi:10.1142/S2424905X18420047.
https://www.worldscientific.com/worldscinet/jmrr

[12] Dehghan, E., O. Goksel and S. E. Salcudean (2006), A Comparison of Needle Bending Models, *Lecture Notes in Computer Science (including subseries Lecture Notes in Artificial Intelligence and Lecture Notes in Bioinformatics)*, **vol. 4190 LNCS - I**, pp. 305–312, ISSN

1611-3349, doi:10.1007/11866565_38.
https://link.springer.com/chapter/10.1007/11866565_38

[13] Ewertsen, C. (2010), PHD Image fusion between ultrasonography and CT, MRI or PET/CT for image guidance and intervention - a theoretical and clinical study.

[14] Fukushima, Y. and K. Naemura (2014), Estimation of the friction force during the needle insertion using the disturbance observer and the recursive least square, *ROBOMECH Journal*, **vol. 1**, pp. 1–8, ISSN 21974225, doi:10.1186/S40648-014-0014-7/FIGURES/10.
https://robomechjournal.springeropen.com/articles/10.1186/s40648-014-0014-7

[15] Fukushima, Y., K. Saito and K. Naemura (2013), Estimation of the Cutting Force Using the Dynamic Friction Coefficient Obtained by Reaction Force During the Needle Insertion, *Procedia CIRP*, **vol. 5**, pp. 265–269, ISSN 2212-8271, doi:10.1016/J.PROCIR.2013.01.052.

[16] Gao, D., Y. Lei, B. Lian and B. Yao (2016), Modeling and Simulation of Flexible Needle Insertion Into Soft Tissue Using Modified Local Constraints, **vol. 138**, no.12, ISSN 1087-1357, doi:10.1115/1.4034134.
https://doi.org/10.1115/1.4034134

[17] Gavin, H. P. (2014), Beam Element Stiffness Matrices.
https://people.duke.edu/~hpgavin/cee421/beam-element.pdf

[18] van Gerwen, D. J., J. Dankelman and J. J. van den Dobbelsteen (2012), Needle–tissue interaction forces – A survey of experimental data, *Medical Engineering Physics*, **vol. 34**, pp. 665–680, ISSN 1350-4533, doi:10.1016/J.MEDENGPHY.2012.04.007.

[19] Herink, M. (2013), Master Thesis: Finite Element Modelling of Prostate Deformation and Needle-Tissue Interactions.

[20] Horton, A., A. Wittek, R. Joldes and K. Miller (2010), A meshless Total Lagrangian explicit dynamics algorithm for surgical simulation, *International Journal for Numerical Methods in Biomedical Engineering Int. J. Numer. Meth. Biomed. Engng*, **vol. 26**, pp. 977–998, doi:10.1002/cnm.1374.
www.interscience.wiley.com

[21] Jushiddi, M. G., J. J. Mulvihill, D. Chovan, A. Mani, C. Shanahan, C. Silien, S. A. M. Tofail and P. Tiernan (2019), Simulation of biopsy bevel-tipped needle insertion into soft-gel, *Computers in Biology and Medicine*, **vol. 111**, p. 103337, ISSN 0010-4825, doi:10.1016/J.COMPBIOMED.2019.103337.

[22] Kataoka, H., T. Washio, K. Chinzei, K. Mizuhara, C. Simone and A. M. Okamura (2002), Measurement of the Tip and Friction Force Acting on a Needle during Penetration, *LNCS*, **vol. 2488**, pp. 216–223.

[23] Kobayashi, Y., T. Sato and M. G. Fujie (2009), Modeling of friction force based on relative velocity between liver tissue and needle for needle insertion simulation, *Proceedings of the 31st Annual International Conference of the IEEE Engineering in Medicine and Biology Society: Engineering the Future of Biomedicine, EMBC*, pp. 5274–5278, doi:10.1109/IEMBS.2009.5334078.

[24] Lei, Y., S. Du, M. Li, T. Xu, Y. Hu and Z. Wang (2024), Needle-tissue interaction model based needle path planning method, *Computer Methods and Programs in Biomedicine*, **vol. 243**, ISSN 0169-2607, doi:10.1016/J.CMPB.2023.107858.

[25] Leong, F., C. Y. Lai, S. F. Khosroshahi, L. He, S. de Lusignan, T. Nanayakkara and M. Ghajari (2022), A Surrogate Model Based on a Finite Element Model of Abdomen for Real-Time Visualisation of Tissue Stress during Physical Examination Training, *Bioengineering 2022*, **vol. 9**, p. 687, ISSN 2306-5354, doi:10.3390/BIOENGINEERING9110687.
https://www.mdpi.com/2306-5354/9/11/687/htmhttps:

//www.mdpi.com/2306-5354/9/11/687

[26] Mahvash, M. and P. E. Dupont (2010), Mechanics of Dynamic Needle Insertion into a Biological Material, *IEEE transactions on bio-medical engineering*, **vol. 57**, pp. 934–943, ISSN 00189294, doi:10.1109/TBME.2009.2036856. /pmc/articles/PMC3021974//pmc/articles/PMC3021974/?report=abstracthttps://www.ncbi.nlm.nih.gov/pmc/articles/PMC3021974/

[27] Misra, S., K. T. Ramesh and A. M. Okamura (2008), Modeling of Tool-Tissue Interactions for Computer-Based Surgical Simulation: A Literature Review, *Presence (Cambridge, Mass.)*, **vol. 17**, pp. 463–491, ISSN 15313263, doi:10.1162/PRES.17.5.463. https://www.ncbi.nlm.nih.gov/pmc/articles/PMC2813063/

[28] Misra, S., K. B. Reed, K. T. Ramesh and A. M. Okamura (2009), Observations of Needle-Tissue Interactions, *Conference proceedings : Annual International Conference of the IEEE Engineering in Medicine and Biology Society. IEEE Engineering in Medicine and Biology Society. Conference*, **vol. 2009**, pp. 262–265, doi:10.1109/IEMBS.2009.5332872. https://www.ncbi.nlm.nih.gov/pmc/articles/PMC2859834/

[29] Moore, J. Z., K. Malukhin, A. J. Shih and K. F. Ehmann (2011), Hollow needle tissue insertion force model, *CIRP Annals - Manufacturing Technology*, **vol. 60**, pp. 157–160, doi:10.1016/j.cirp.2011.03.101. http://ees.elsevier.com/cirp/default.asp

[30] Muzzammil, H. M., Y.-D. Zhang, H. Ejaz, Q. Yuan and M. Muddassir (2024), A review on tissue-needle interaction and path planning models for bevel tip type flexible needle minimal intervention, *Mathematical Biosciences and Engineering 2024 1:523*, **vol. 21**, pp. 523–561, ISSN 1551-0018, doi:10.3934/MBE.2024023. http://www.aimspress.com/article/doi/10.3934/mbe.2024023http://www.aimspress.com/rticle/doi/10.3934/mbe.2024023

[31] Okamura, A. M., C. Simone and M. D. O'Leary (2004), Force modeling for needle insertion into soft tissue, *IEEE Transactions on Biomedical Engineering*, **vol. 51**, pp. 1707–1716, ISSN 00189294, doi:10.1109/TBME.2004.831542.

[32] van Otterloo, J. and A. R. Cruden (2016), Rheology of pig skin gelatine: Defining the elastic domain and its thermal and mechanical properties for geological analogue experiment applications, *Tectonophysics*, **vol. 683**, pp. 86–97, ISSN 0040-1951, doi:10.1016/J.TECTO.2016.06.019.

[33] Reed, K. B., A. M. Okamura and N. J. Cowan (2009), Modeling and Control of Needles with Torsional Friction, *IEEE transactions on bio-medical engineering*, **vol. 56**, p. 2905–2916, ISSN 00189294, doi:10.1109/TBME.2009.2029240. https://www.ncbi.nlm.nih.gov/pmc/articles/PMC2859043/

[34] Rippy, J. R., M. Singh, S. R. Aglyamov and K. V. Larin (2021), Ultrasound Shear Wave Elastography and Transient Optical Coherence Elastography: Side-by-Side Comparison of Repeatability and Accuracy, *IEEE Open Journal of Engineering in Medicine and Biology*, **vol. 2**, pp. 179–186, ISSN 26441276, doi:10.1109/OJEMB.2021.3075569.

[35] Roesthuis, R. J., Y. R. van Veen, A. Jahya and S. Misra (2011), Mechanics of needle-tissue interaction, *IEEE/RSJ International Conference on Intelligent Robots and Systems*, pp. 2557–2563, doi:10.1109/IROS.2011.6094969.

[36] Scali, M., P. A. H. Veldhoven, P. W. J. Henselmans, D. Dodou and P. Breedveld (2019), Design of an ultra-thin steerable probe for percutaneous interventions and preliminary evaluation in a gelatine phantom, **vol. 14**, no.9, pp. 1–24, doi:10.1371/journal.pone.0221165. https://doi.org/10.1371/journal.pone.0221165

[37] Siepel, F. J., B. Maris, M. K. Welleweerd, V. Groenhuis, P. Fiorini and S. Stramigioli (2021), Needle and Biopsy Robots: a Review, *Current Robotics Reports 2021 2:1*, **vol. 2**, pp. 73–84, ISSN 2662-4087, doi:10.1007/S43154-020-00042-1.
https://link.springer.com/article/10.1007/s43154-020-00042-1

[38] Zhao, M., D. Gao, S. Zhao, L. Wang and L. Li (2019), Modelling Soft Tissue Deformation Based on Spatial Kriging, *IOP Conference Series: Materials Science and Engineering*, **vol. 646**, ISSN 1757-899X, doi:10.1088/1757-899X/646/1/012021.
https://iopscience.iop.org/article/10.1088/1757-899X/646/1/012021

8 Appendix

8.1 Axial forces of dry-runs

This section shows the results of the dry runs at 3.33 mm/sec, 5 mm/sec and 10 mm/sec. As can be seen with increasing speed the effect of friction caused by the bent in the needle remains prominently present. There is no relation between the magnitude of the peaks and the insertion speed.

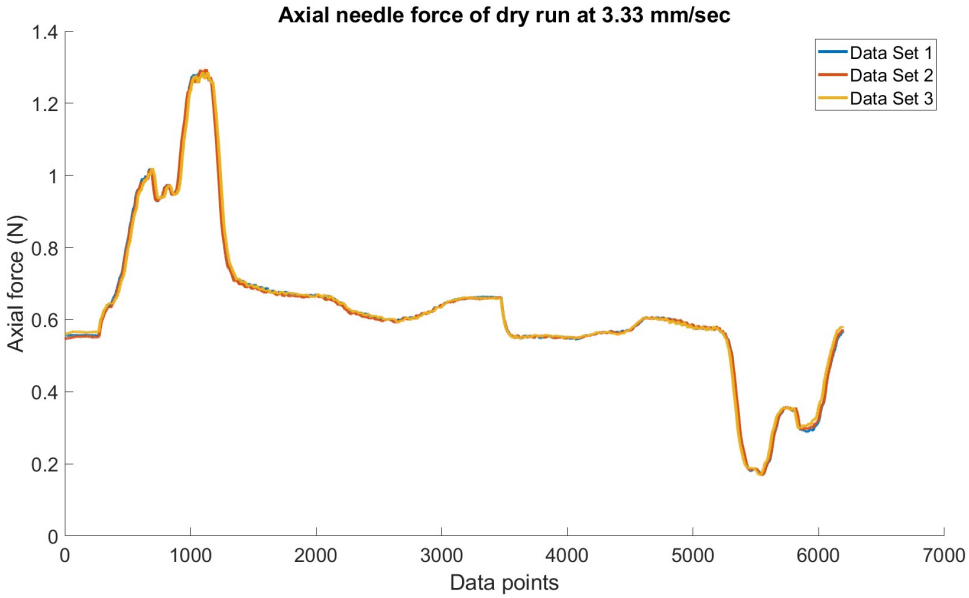

Figure 8.1: Axial force of needle insertion during a dry run at 3.33 mm/sec.

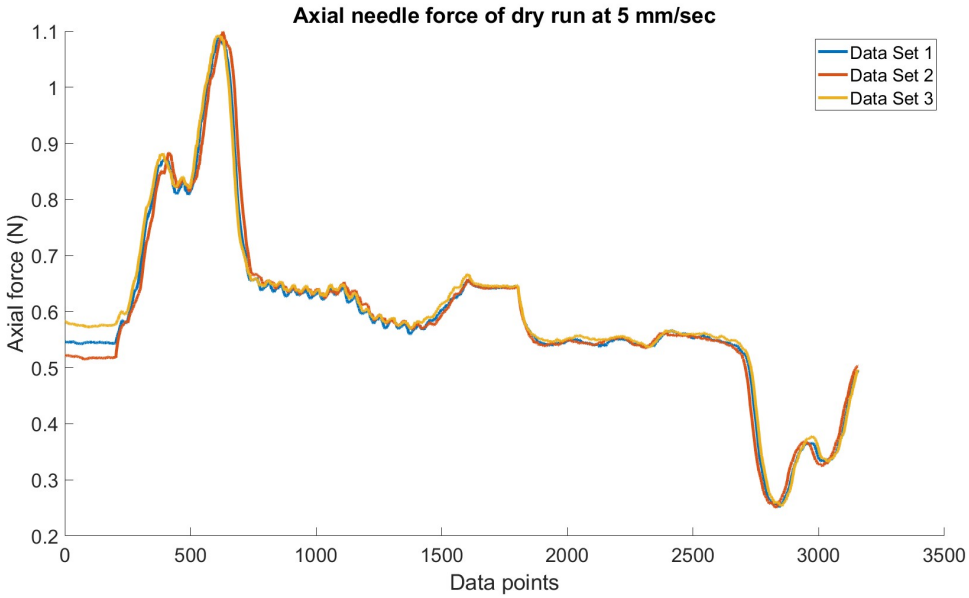

Figure 8.2: Axial force of needle insertion during a dry run at 5 mm/sec.

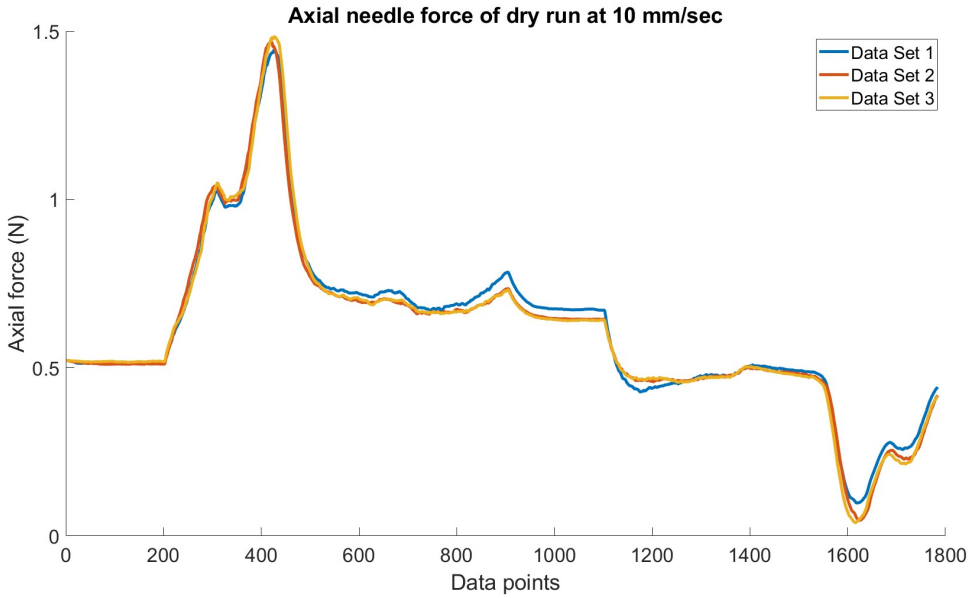

Figure 8.3: Axial force of needle insertion during a dry run at 10 mm/sec.

8.2 Unfiltered axial forces of insertions and retractions into phantom

The following 3 graphs show the results of the unfiltered forces of an insertion and retraction into a 10% wt gelatin phantom (33% cleaning vinegar and 66% water). The clear effect of the setup forces can be seen in the figures.

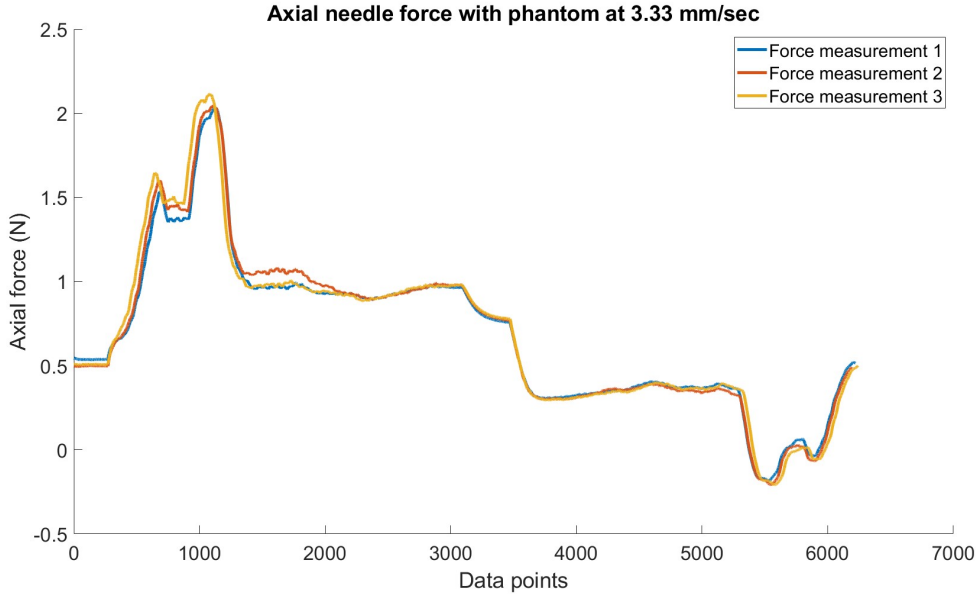

Figure 8.4: Unfiltered axial needle force of an insertion and retraction into a 10% wt gelatin phantom at 3.33 mm/sec.

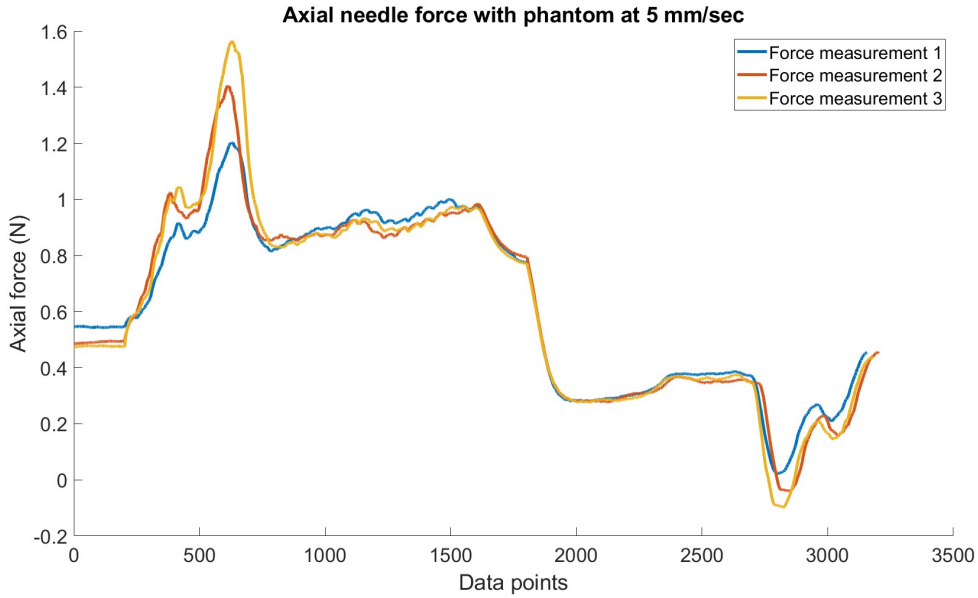

Figure 8.5: Unfiltered axial needle force of an insertion and retraction into a 10% wt gelatin phantom at 5 mm/sec.

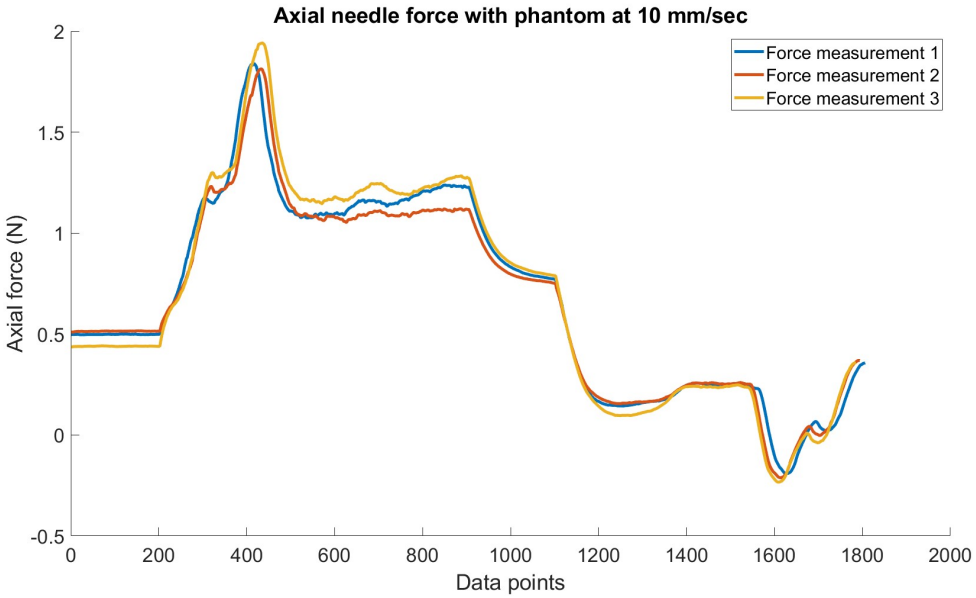

Figure 8.6: Unfiltered axial needle force of an insertion and retraction into a 10% wt gelatin phantom at 10 mm/sec.

8.3 Filtered axial forces of insertion into phantom

The following 3 figures show the filtered insertion forces into a gelatin phantom at 3.33 mm/sec, 5 mm/sec and 10 mm/sec. The filtering has been done by subtracting the average force, of the 3 dry runs, from the measured forces. The effect of the peaks, caused by the bent in the needle, are still visible but removed from the important parts of the graph.

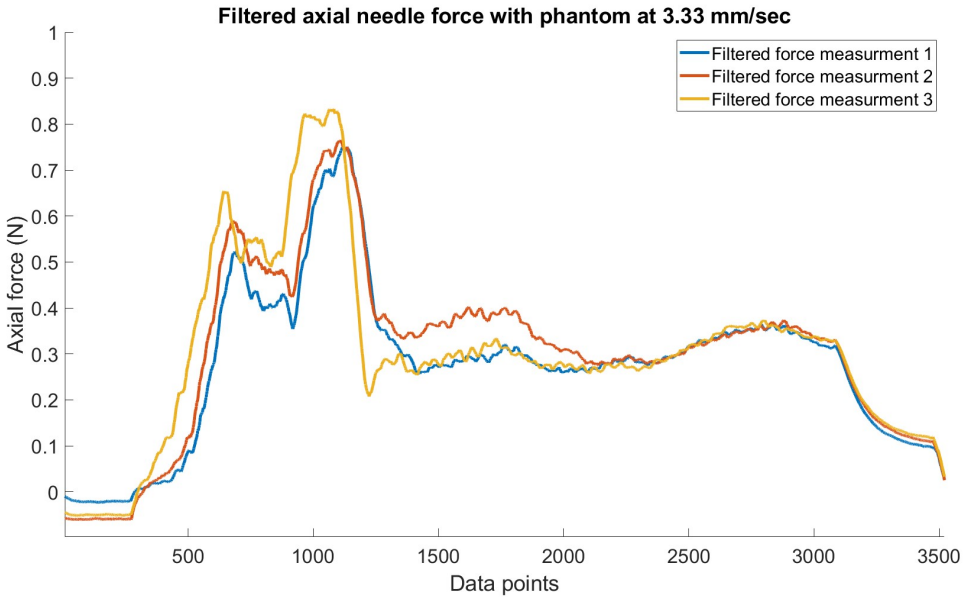

Figure 8.7: Filtered axial needle force of insertion into a 10% wt gelatin phantom at 3.33 mm/sec.

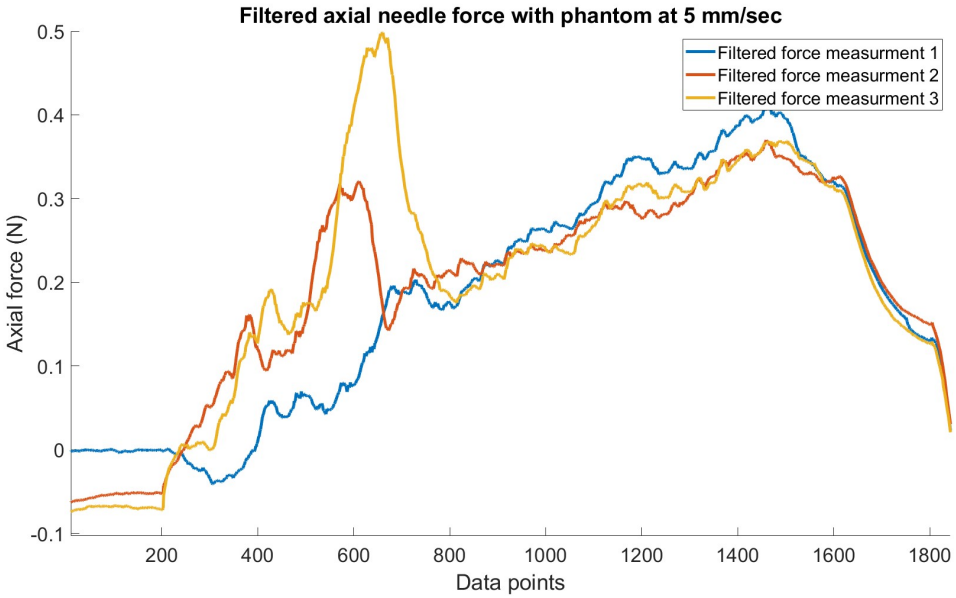

Figure 8.8: Filtered axial needle force of insertion into a 10% wt gelatin phantom at 5 mm/sec.

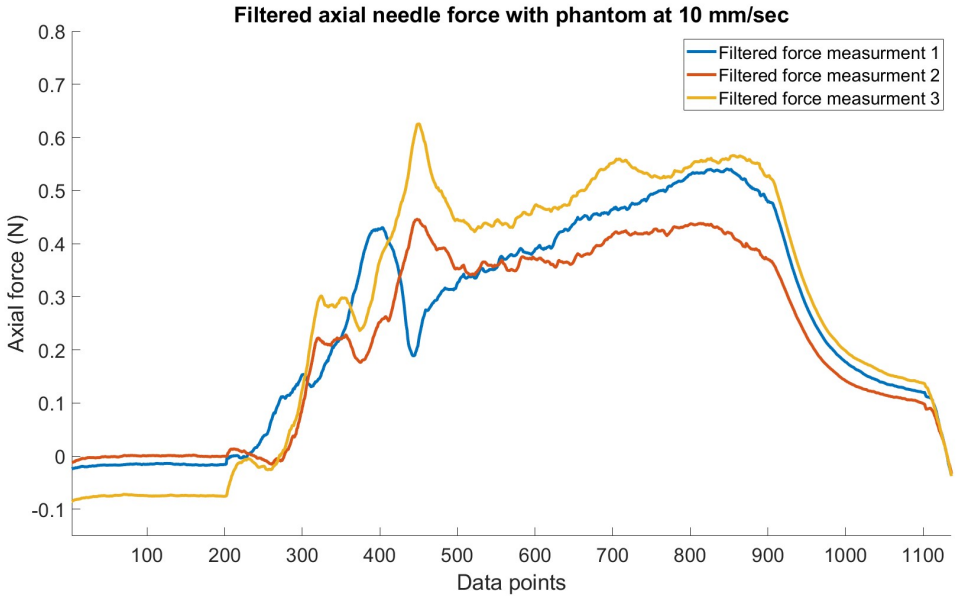

Figure 8.9: Filtered axial needle force of insertion into a 10% wt gelatin phantom at 10 mm/sec.

8.4 Water vs cleaning vinegar

The following three graphs show filtered insertion forces into a gelatin phantom build with 100% water. After the needle tip exits the phantom a pause of 5 seconds is introduced to make sure that the only forces measured are friction forces when moving further. The effect of the setup forces in these graphs is less prominent. The measured friction and cutting forces are approximately the same as with the phantom that used cleaning vinegar.

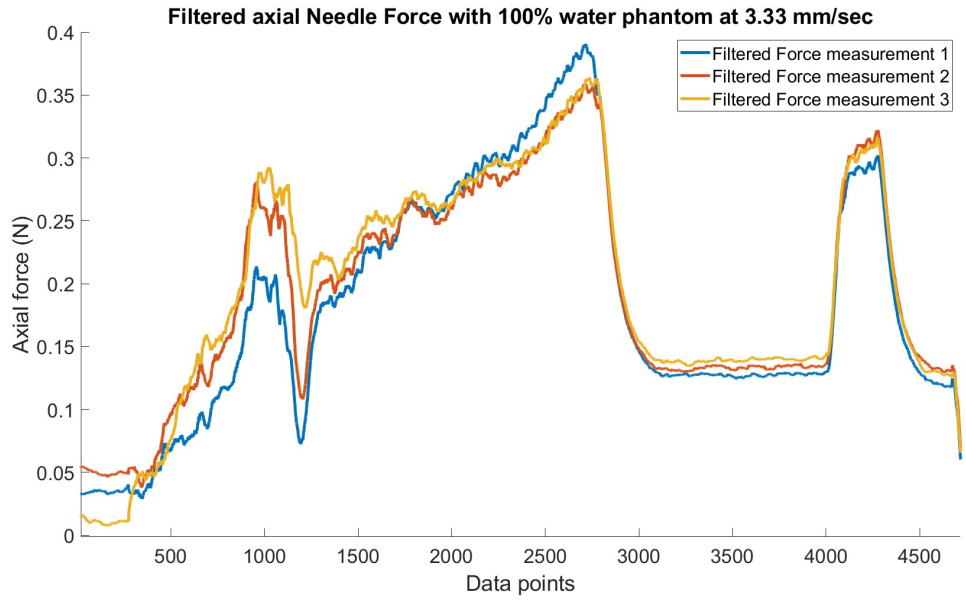

Figure 8.10: Filtered axial needle force into a phantom made out of 100% water at 3.33 mm/sec. After the needle tip exits the phantom the needle is paused for 5 seconds and moved further.

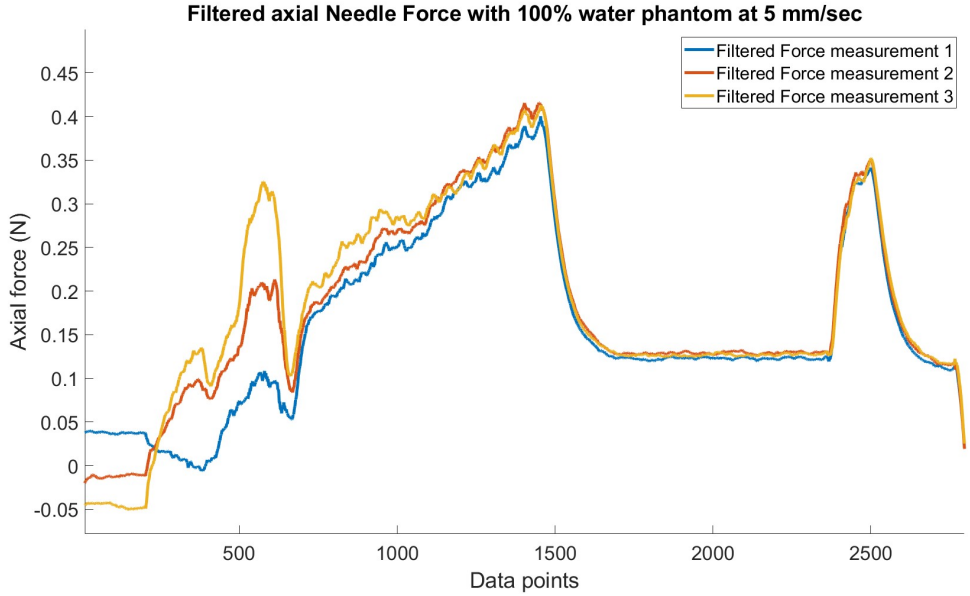

Figure 8.11: Filtered axial needle force into a phantom made out of 100% water at 5 mm/sec. After the needle tip exits the phantom the needle is paused for 5 seconds and moved further.

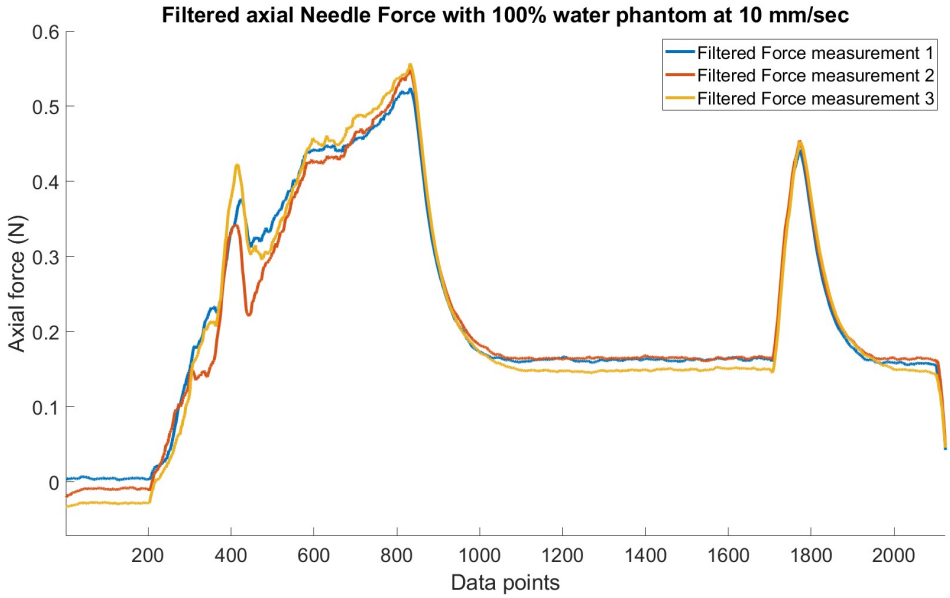

Figure 8.12: Filtered axial needle force into a phantom made out of 100% water at 10 mm/sec. After the needle tip exits the phantom the needle is paused for 5 seconds and moved further.

8.5 Deformation results simulation

The following 3 figures show the movement of nodes 2, 3 and 4 of the simulation. It is the displacement in the x- and y-direction of an insertion with 3 mm/sec into a 10% wt gelatin phantom.

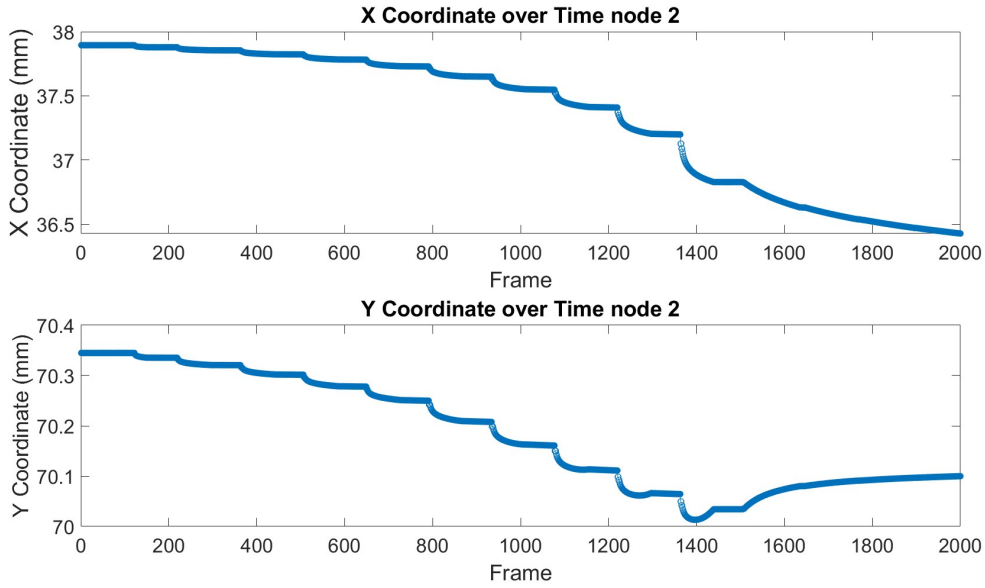

Figure 8.13: X- and y-displacement of node 2 over time of an insertion into a 10% wt gelatin phantom at 3 mm/sec.

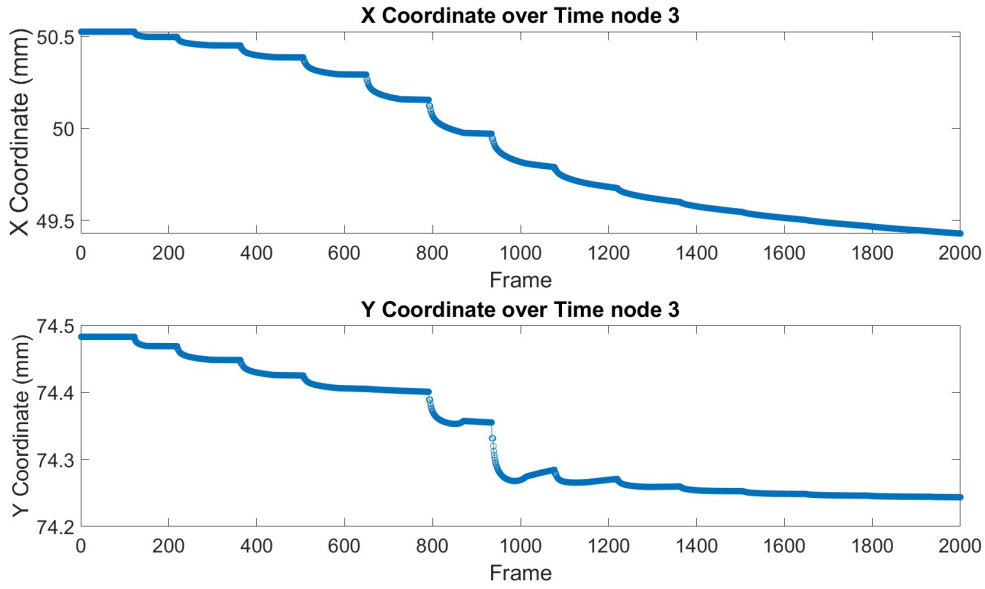

Figure 8.14: X- and y-displacement of node 3 over time of an insertion into a 10% wt gelatin phantom at 3 mm/sec.

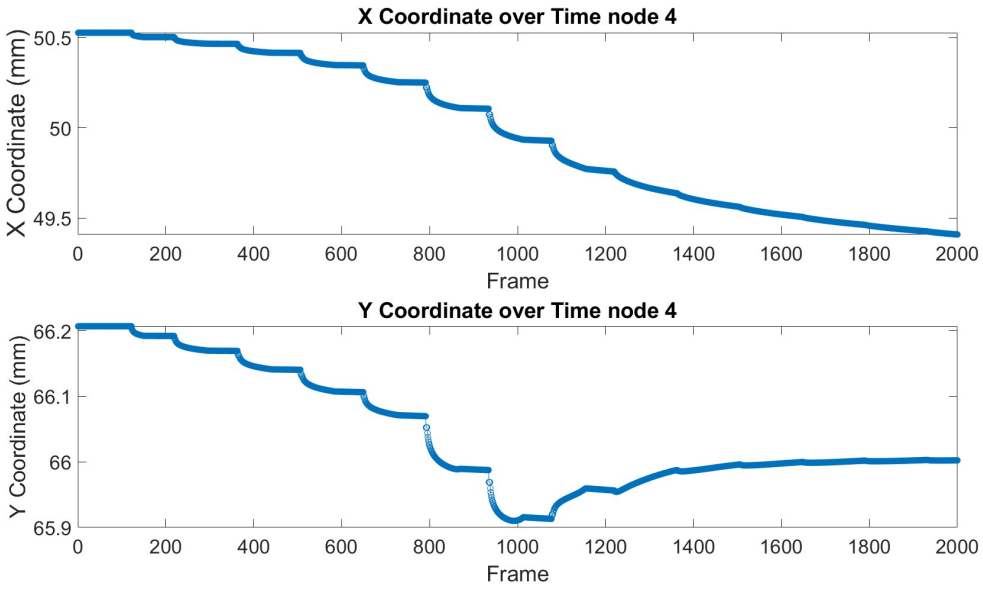

Figure 8.15: X- and y-displacement of node 4 over time of an insertion into a 10% wt gelatin phantom at 3 mm/sec.

8.6 Screw displacements experiments

The following figures show the displacement, in the x- and y -direction, of the 3 screws that correspond with the nodes used in the simulation. The displacements are caused by the needle that is inserted into the 10% wt gelatin phantom with a speed of 3 mm/sec.

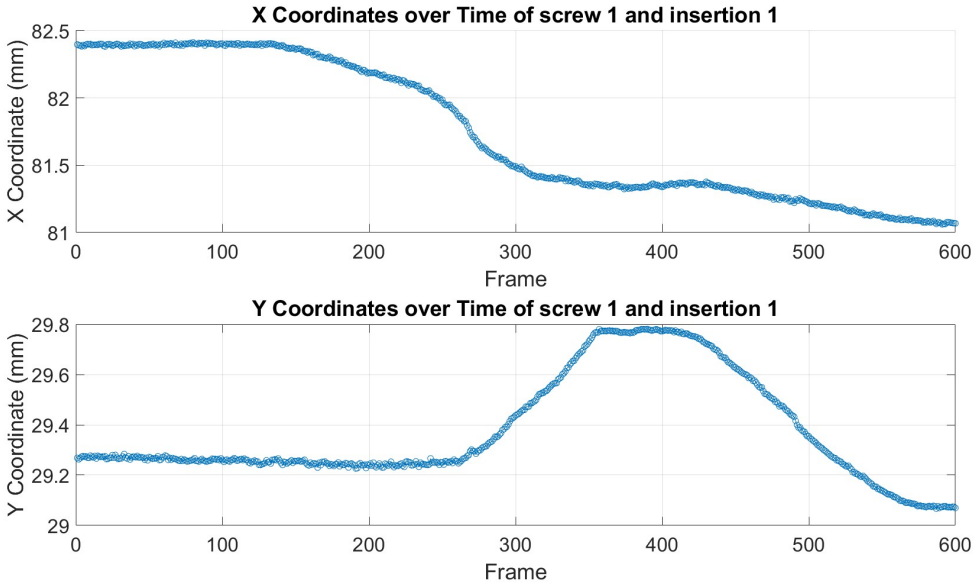

Figure 8.16: X- and y- displacement of screw 1 over time of insertion 1 into a 10% wt gelatin phantom at 3 mm/sec.

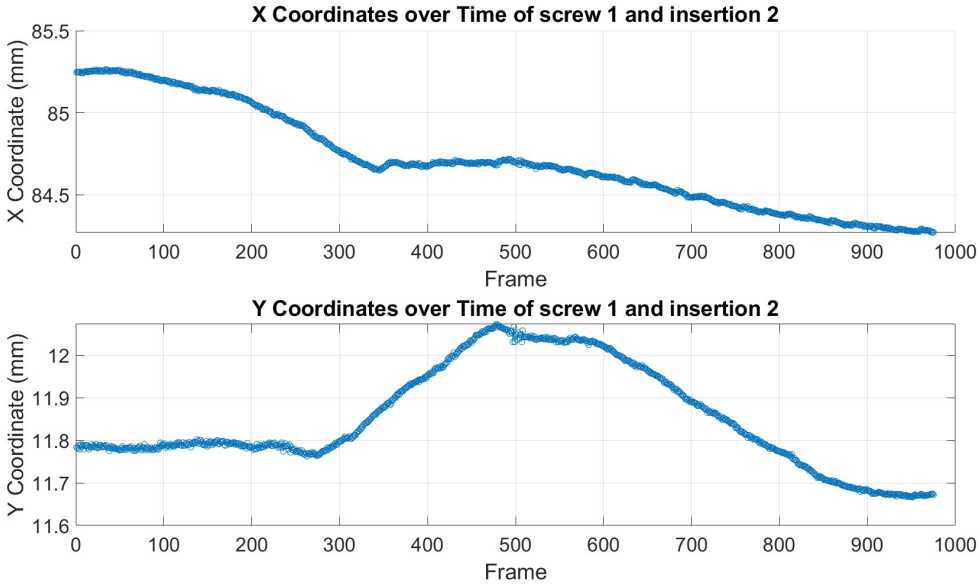

Figure 8.17: X- and y- displacement of screw 1 over time of insertion 2 into a 10% wt gelatin phantom at 3 mm/sec.

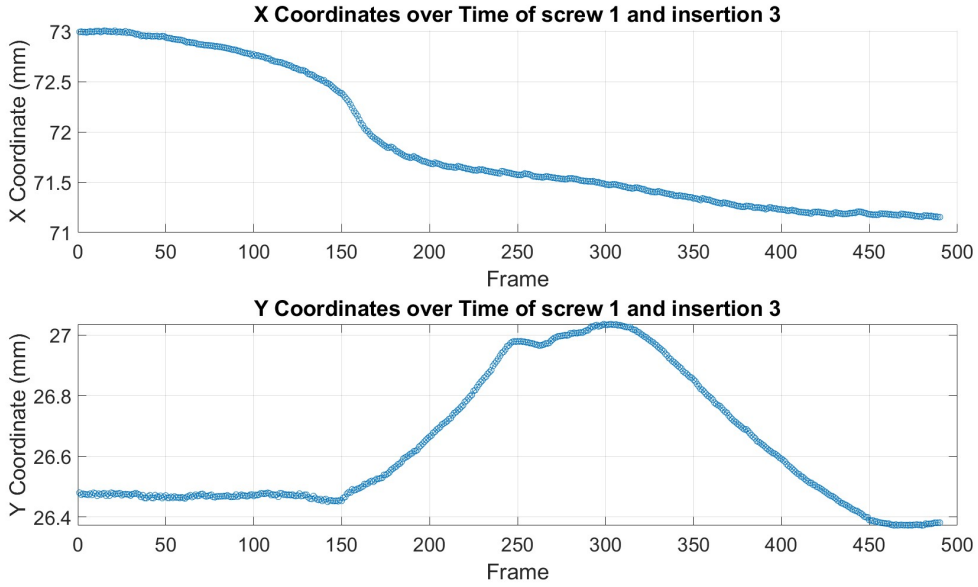

Figure 8.18: X- and y- displacement of screw 1 over time of insertion 3 into a 10% wt gelatin phantom at 3 mm/sec.

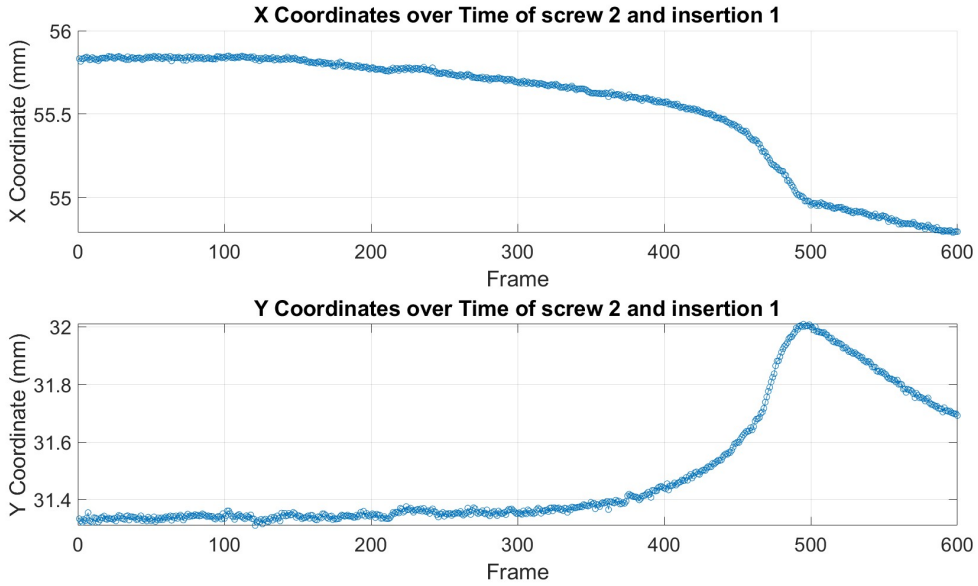

Figure 8.19: X- and y- displacement of screw 2 over time of insertion 1 into a 10% wt gelatin phantom at 3 mm/sec.

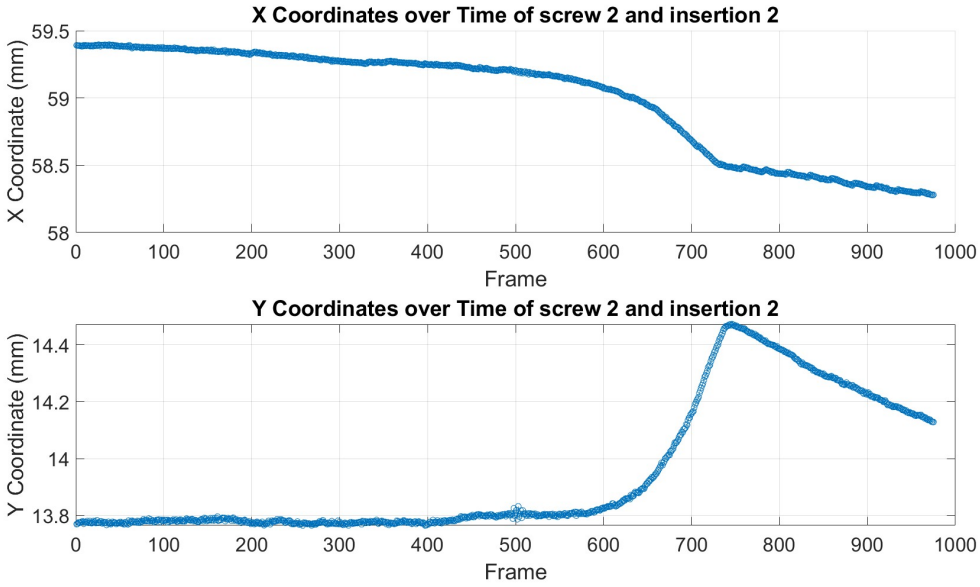

Figure 8.20: X- and y- displacement of screw 2 over time of insertion 2 into a 10% wt gelatin phantom at 3 mm/sec.

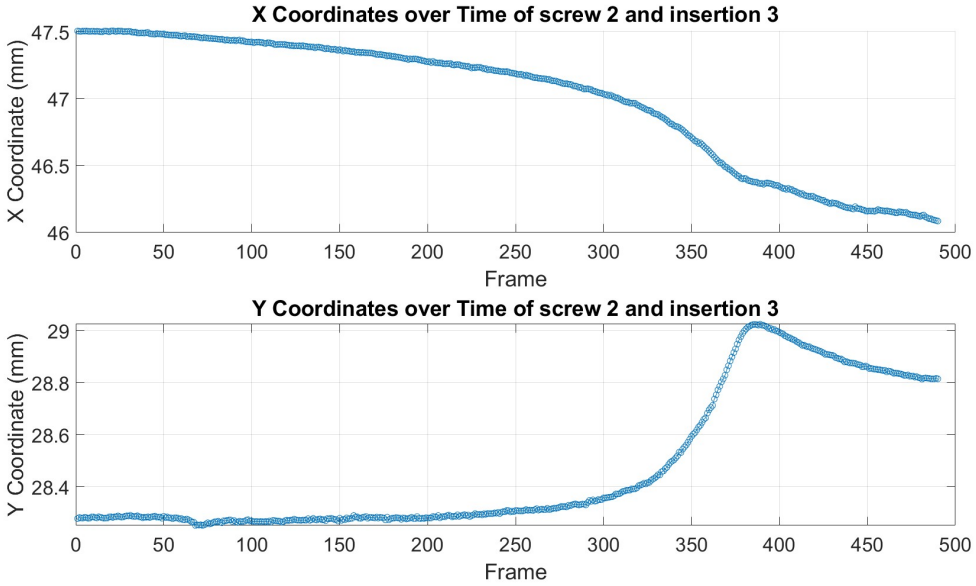

Figure 8.21: X- and y- displacement of screw 2 over time of insertion 3 into a 10% wt gelatin phantom at 3 mm/sec.

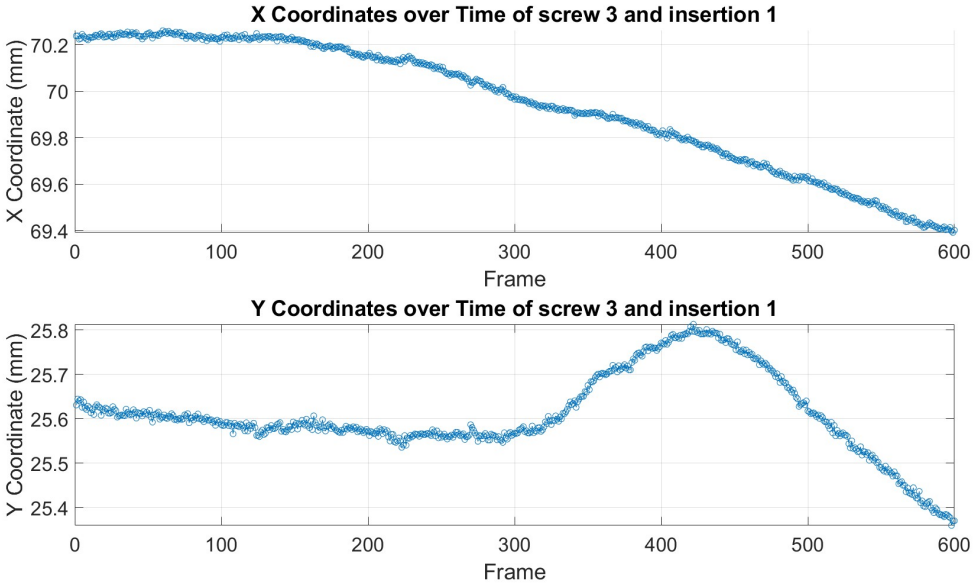

Figure 8.22: X- and y- displacement of screw 3 over time of insertion 1 into a 10% wt gelatin phantom at 3 mm/sec.

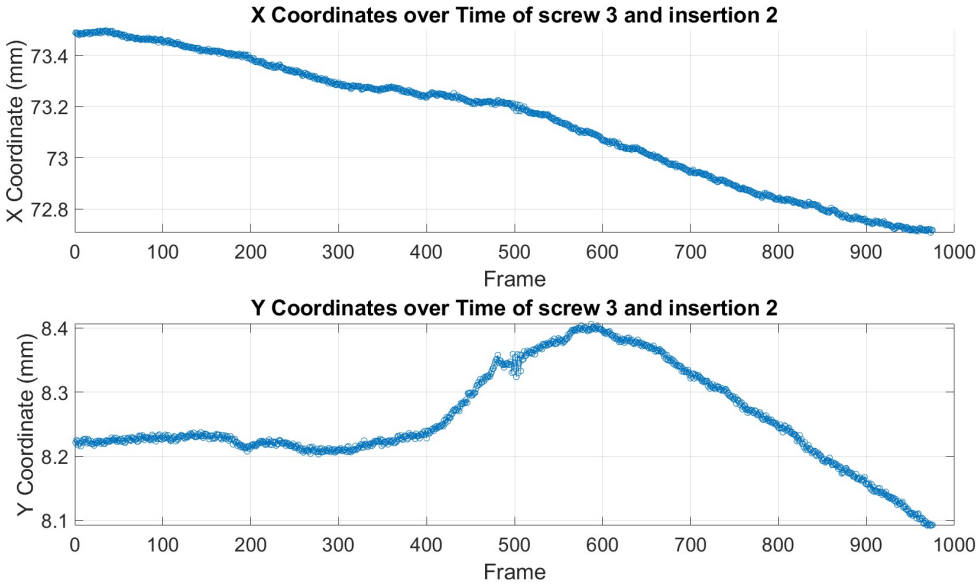

Figure 8.23: X- and y- displacement of screw 3 over time of insertion 2 into a 10% wt gelatin phantom at 3 mm/sec.

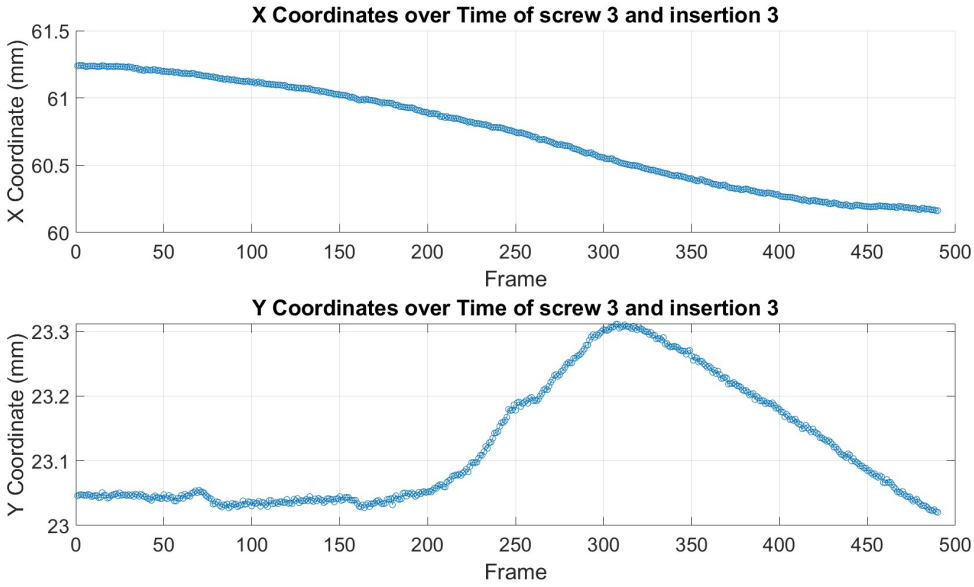

Figure 8.24: X- and y- displacement of screw 3 over time of insertion 3 into a 10% wt gelatin phantom at 3 mm/sec.

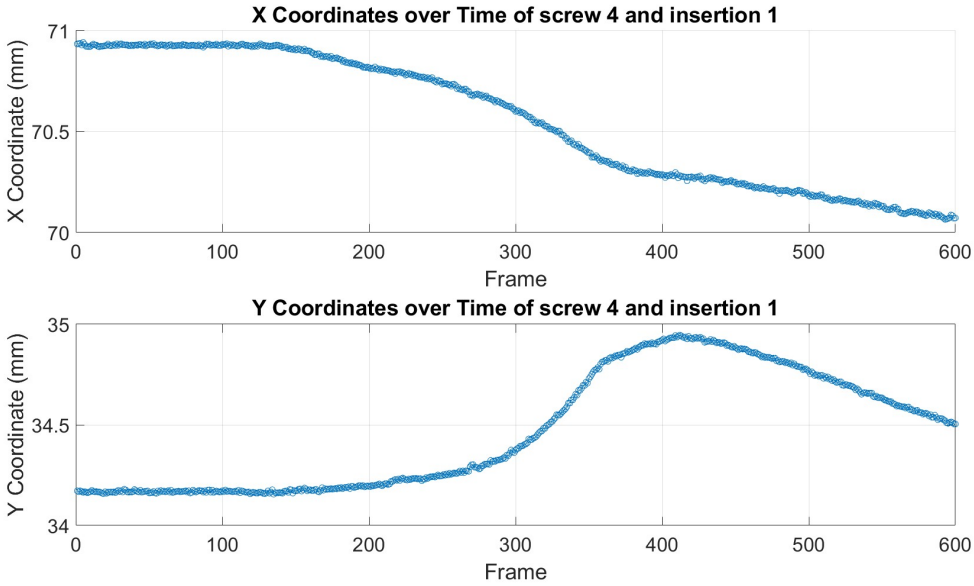

Figure 8.25: X- and y- displacement of screw 4 over time of insertion 1 into a 10% wt gelatin phantom at 3 mm/sec.

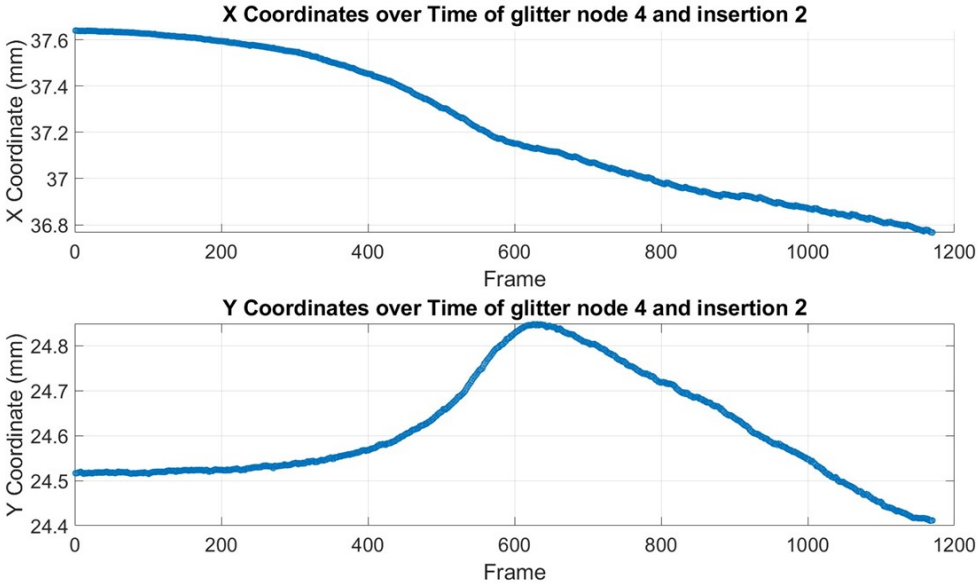

Figure 8.26: X- and y- displacement of screw 4 over time of insertion 2 into a 10% wt gelatin phantom at 3 mm/sec.

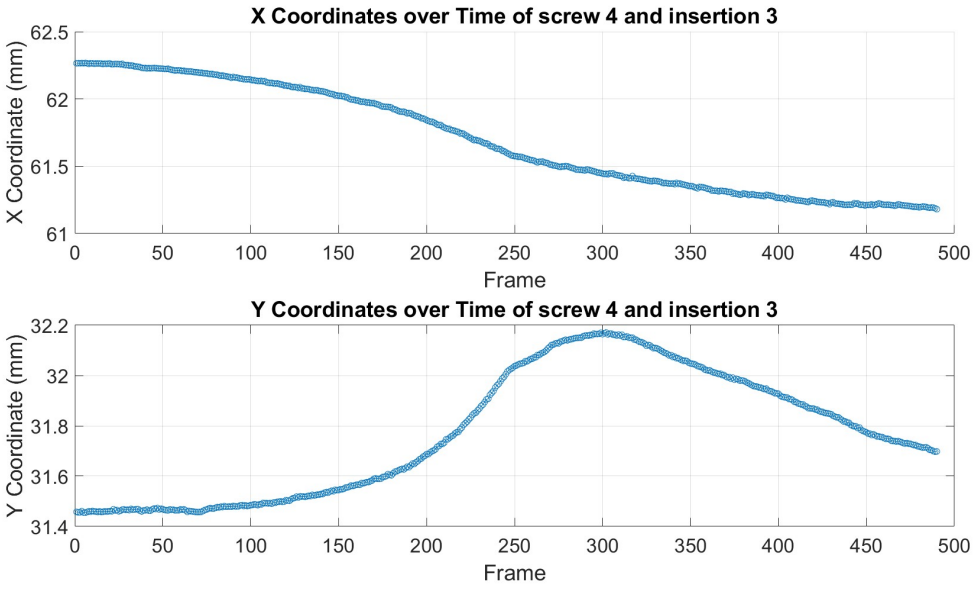

Figure 8.27: X- and y- displacement of screw 4 over time of insertion 3 into a 10% wt gelatin phantom at 3 mm/sec.

8.7 Glitter node experiment 3mm/sec

The following figures show the deformation of the 4 glitter nodes of all 3 insertions at a speed of 3 mm/sec. The deformation is caused by a needle insertion into a 10% wt gelatin phantom at 3 mm/sec. The 4 chosen nodes correspond closely with the nodes from the simulation.

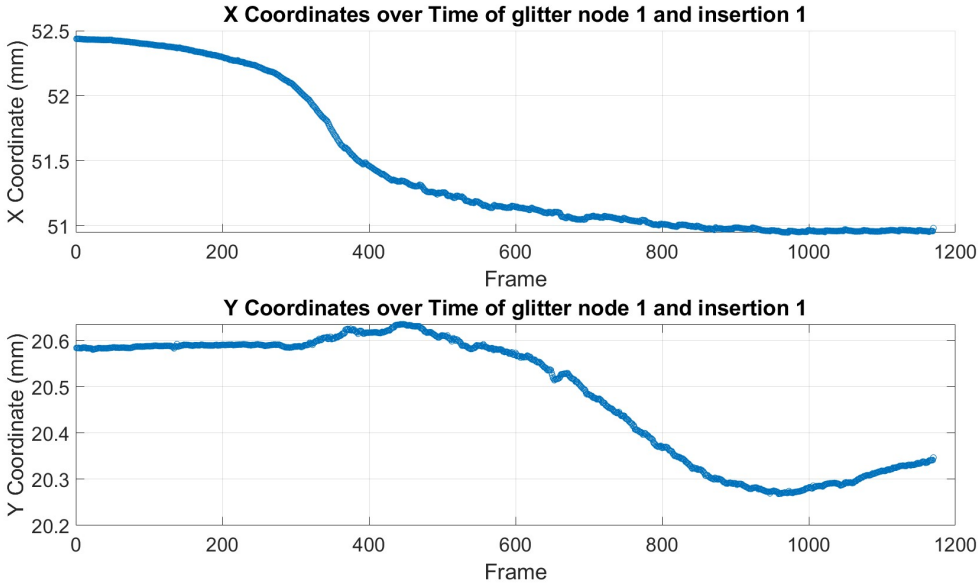

Figure 8.28: X- and y- displacement of glitter node 1 over time of insertion 1 into a 10% wt gelatin phantom at 3 mm/sec.

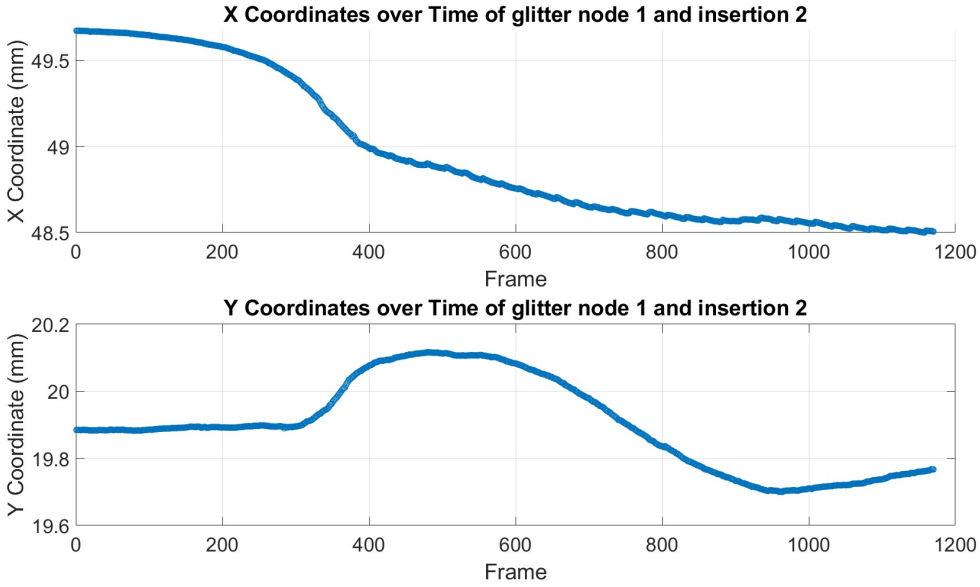

Figure 8.29: X- and y- displacement of glitter node 1 over time of insertion 2 into a 10% wt gelatin phantom at 3 mm/sec.

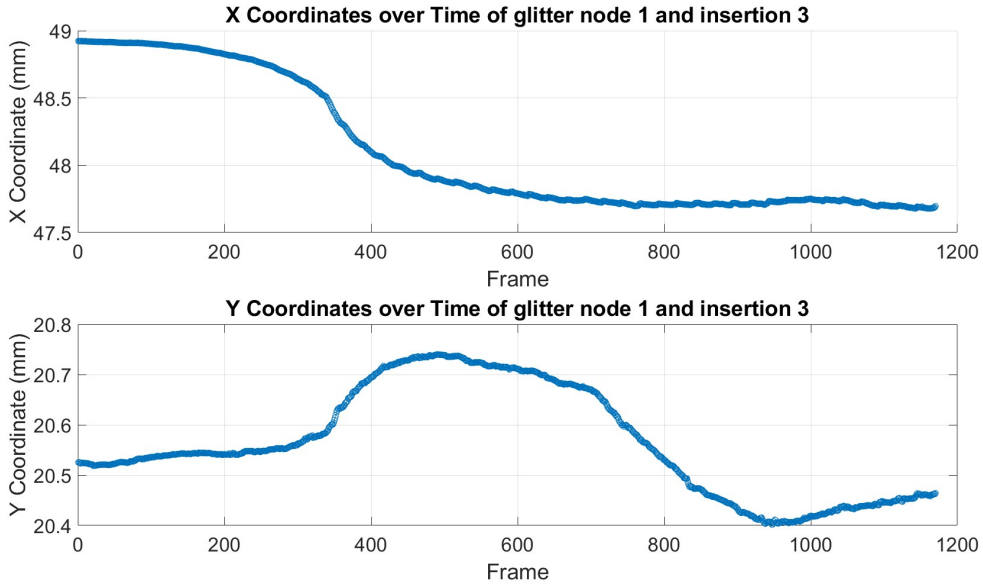

Figure 8.30: X- and y- displacement of glitter node 1 over time of insertion 3 into a 10% wt gelatin phantom at 3 mm/sec.

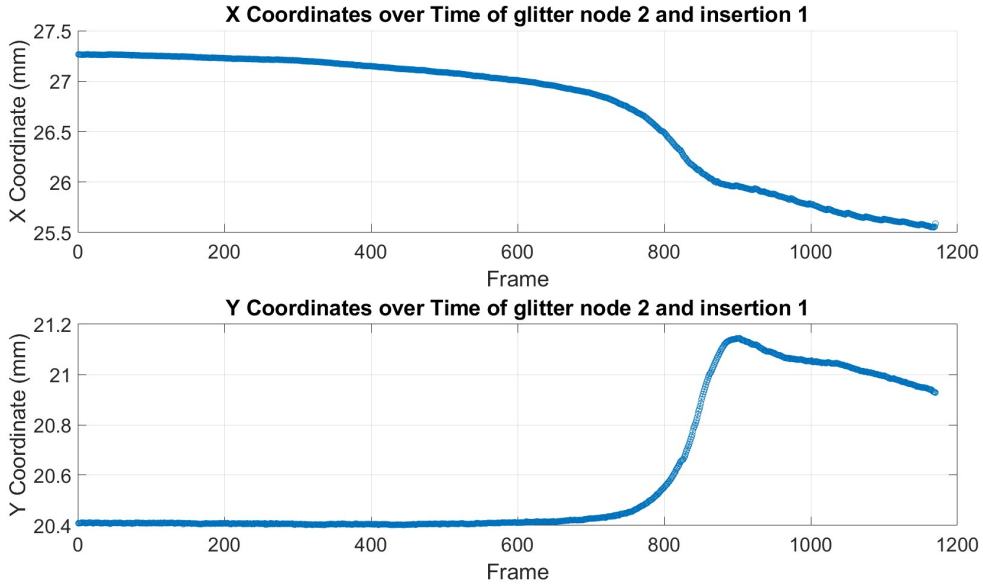

Figure 8.31: X- and y- displacement of glitter node 2 over time of insertion 1 into a 10% wt gelatin phantom at 3 mm/sec.

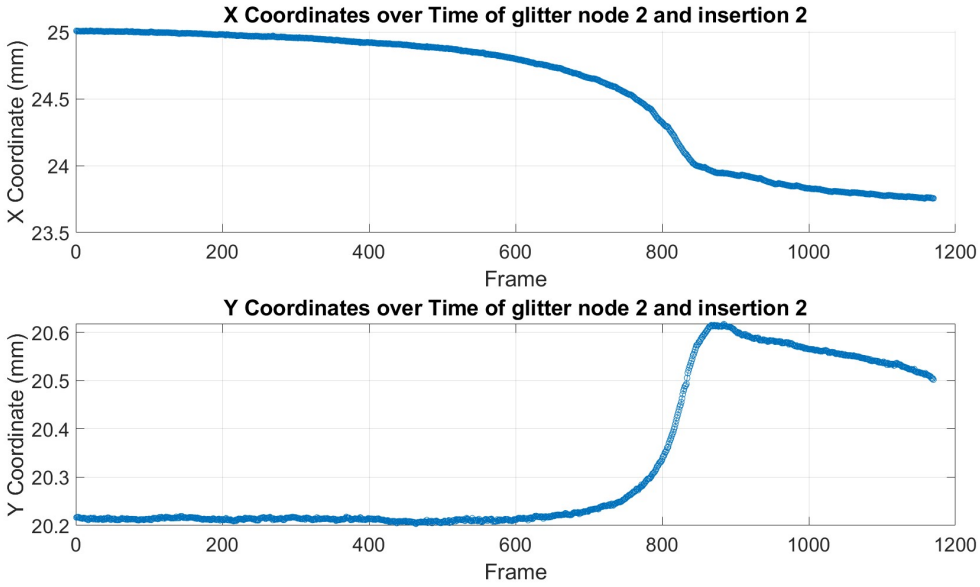

Figure 8.32: X- and y- displacement of glitter node 2 over time of insertion 2 into a 10% wt gelatin phantom at 3 mm/sec.

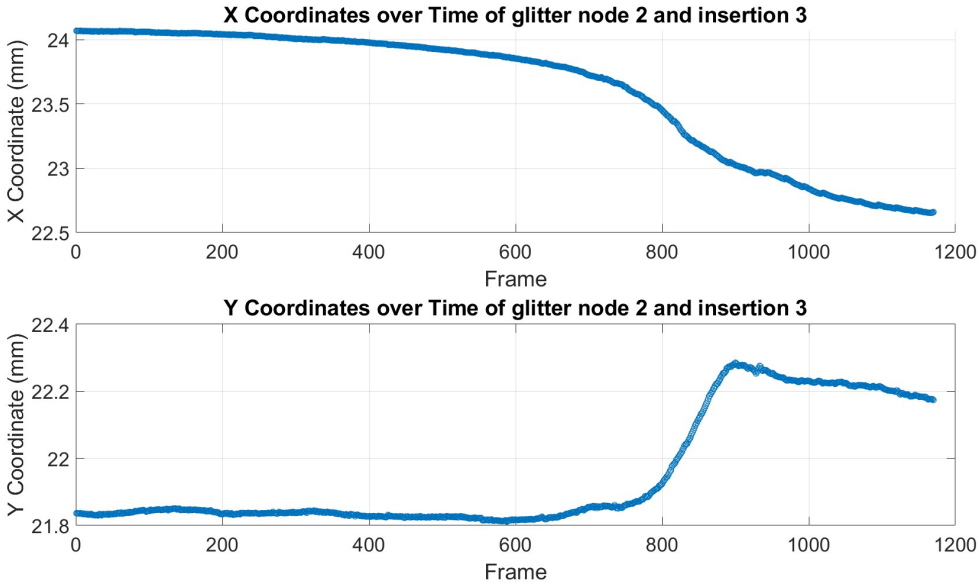

Figure 8.33: X- and y- displacement of glitter node 2 over time of insertion 3 into a 10% wt gelatin phantom at 3 mm/sec.

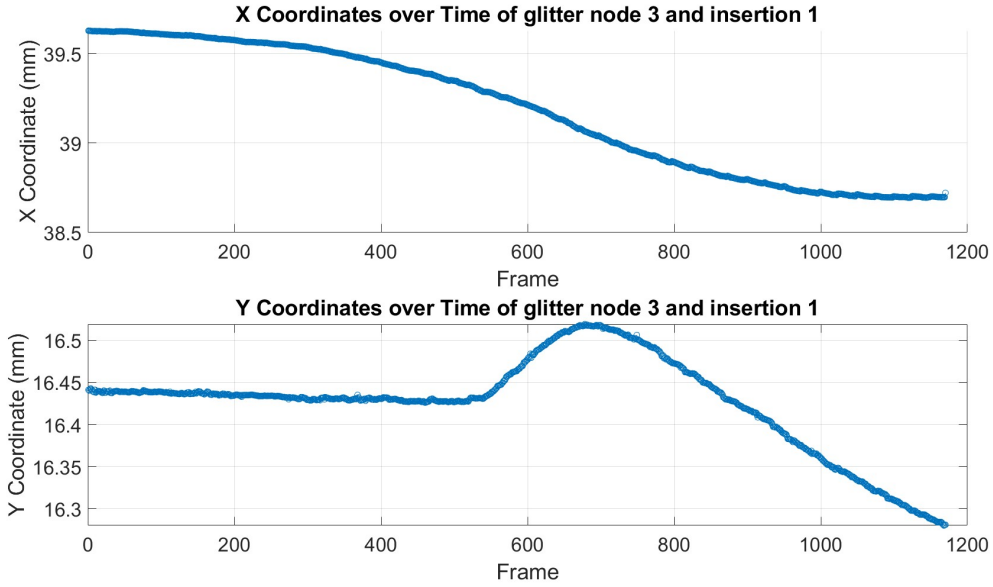

Figure 8.34: X- and y- displacement of glitter node 3 over time of insertion 1 into a 10% wt gelatin phantom at 3 mm/sec.

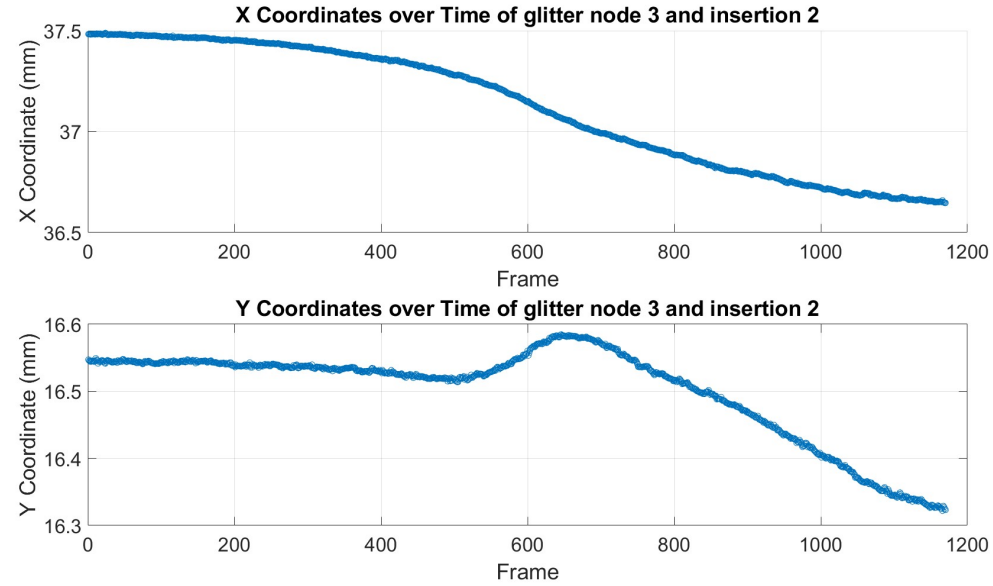

Figure 8.35: X- and y- displacement of glitter node 3 over time of insertion 2 into a 10% wt gelatin phantom at 3 mm/sec.

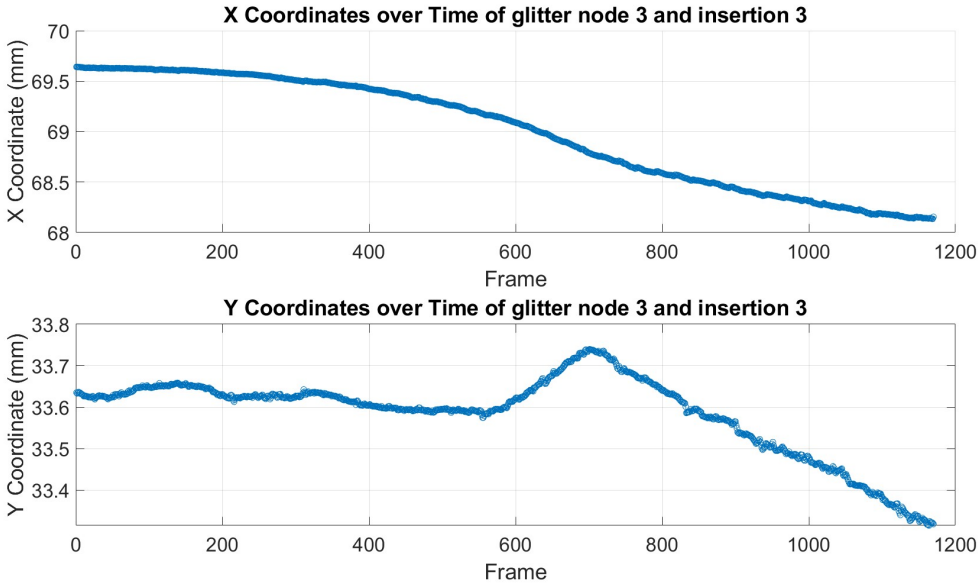

Figure 8.36: X- and y- displacement of glitter node 3 over time of insertion 3 into a 10% wt gelatin phantom at 3 mm/sec.

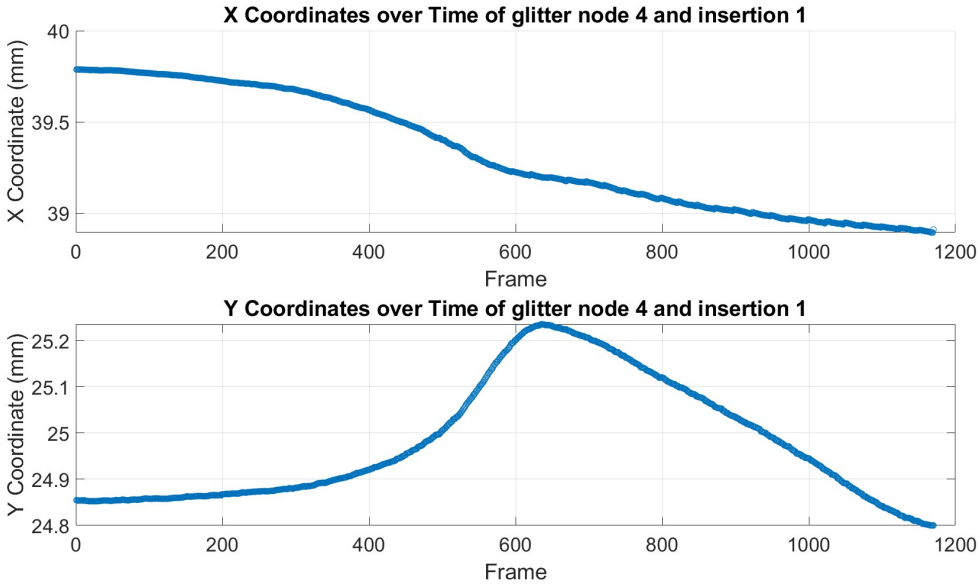

Figure 8.37: X- and y- displacement of glitter node 4 over time of insertion 1 into a 10% wt gelatin phantom at 3 mm/sec.

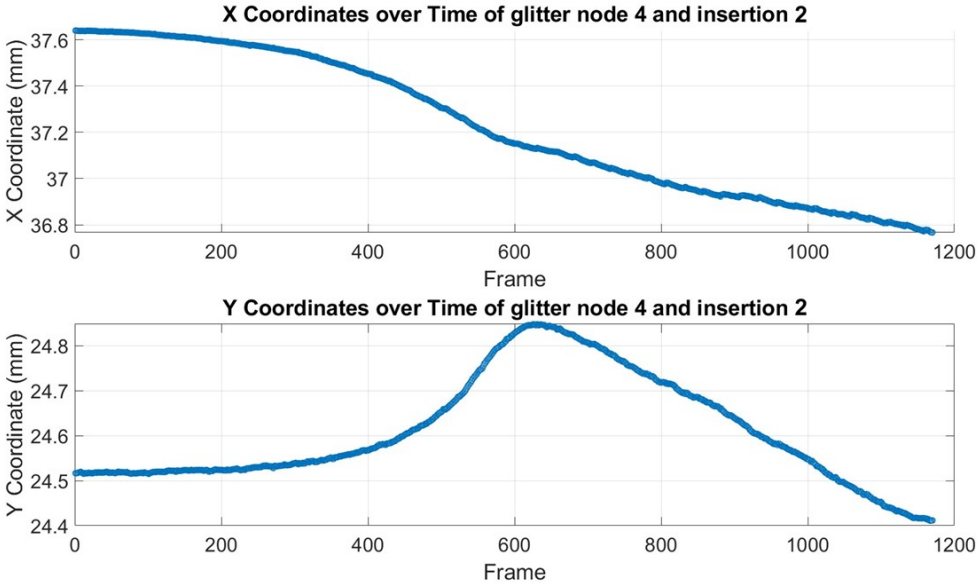

Figure 8.38: X- and y- displacement of glitter node 4 over time of insertion 2 into a 10% wt gelatin phantom at 3 mm/sec.

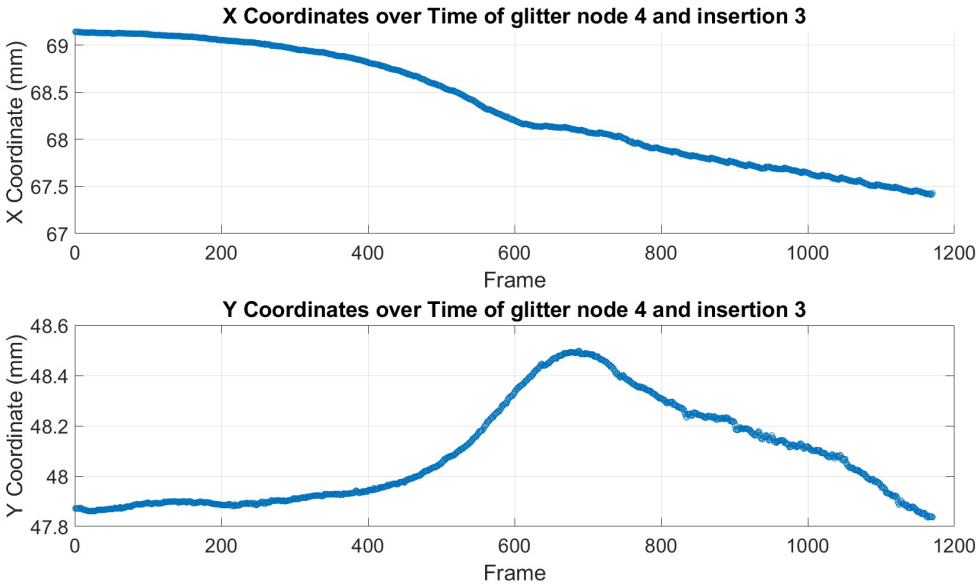

Figure 8.39: X- and y- displacement of glitter node 4 over time of insertion 3 into a 10% wt gelatin phantom at 3 mm/sec.

8.8 Glitter node experiment 10 mm/sec

The following 4 figures show the deformation of the 4 glitter nodes of only the first insertion into a 10% wt gelatin phantom at 10 mm/sec.

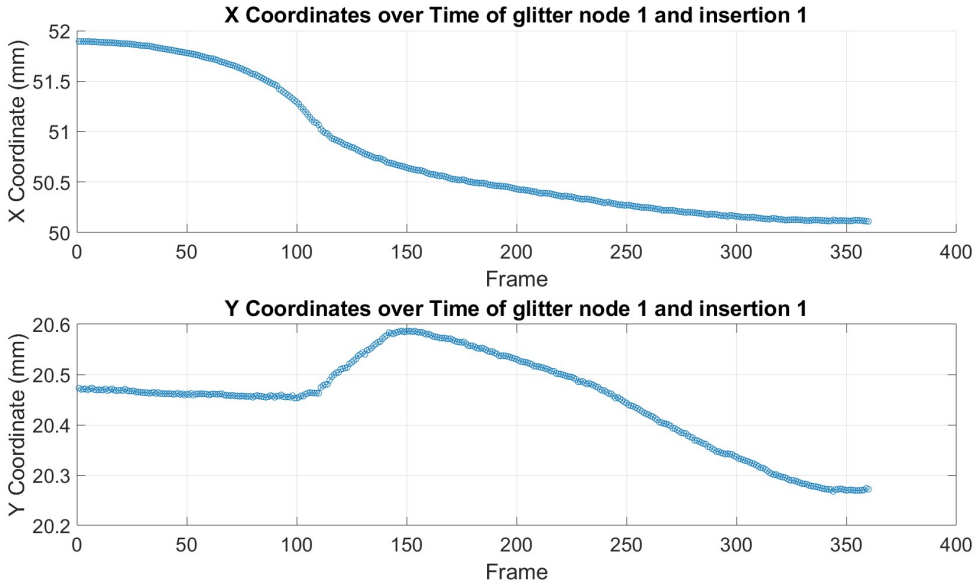

Figure 8.40: X- and y- displacement of glitter node 1 over time of insertion 1 into a 10% wt gelatin phantom at 10 mm/sec.

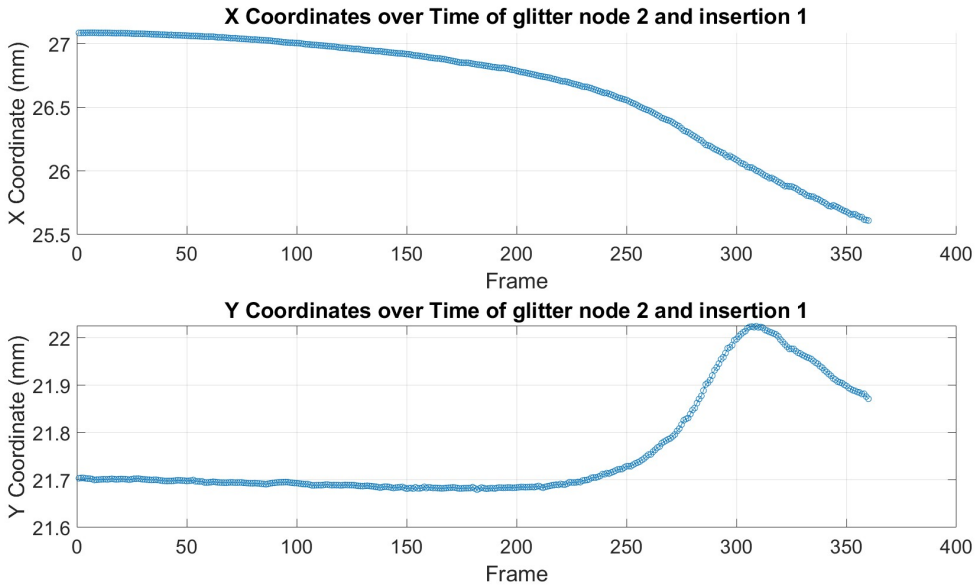

Figure 8.41: X- and y- displacement of glitter node 2 over time of insertion 1 into a 10% wt gelatin phantom at 10 mm/sec.

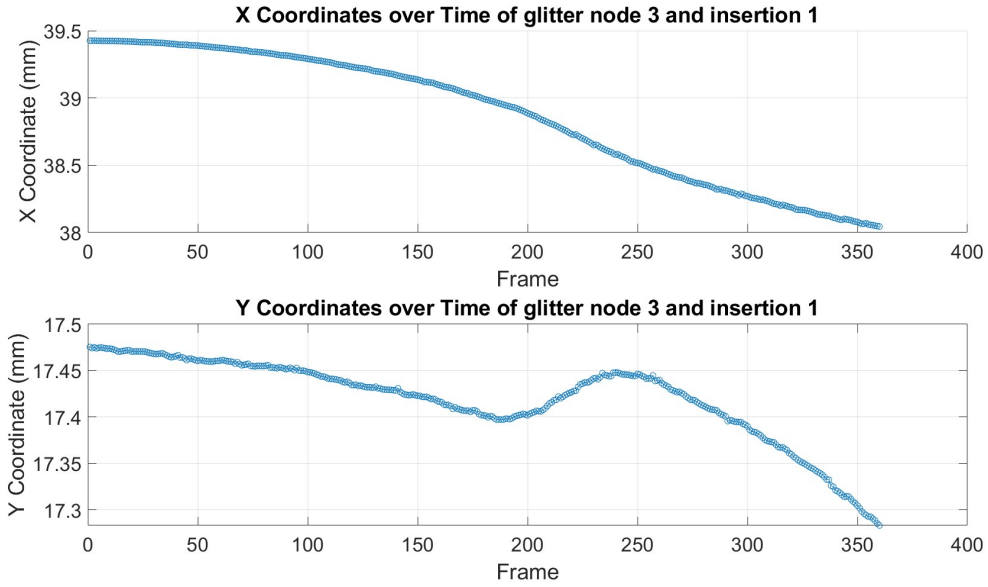

Figure 8.42: X- and y- displacement of glitter node 3 over time of insertion 1 into a 10% wt gelatin phantom at 10 mm/sec.

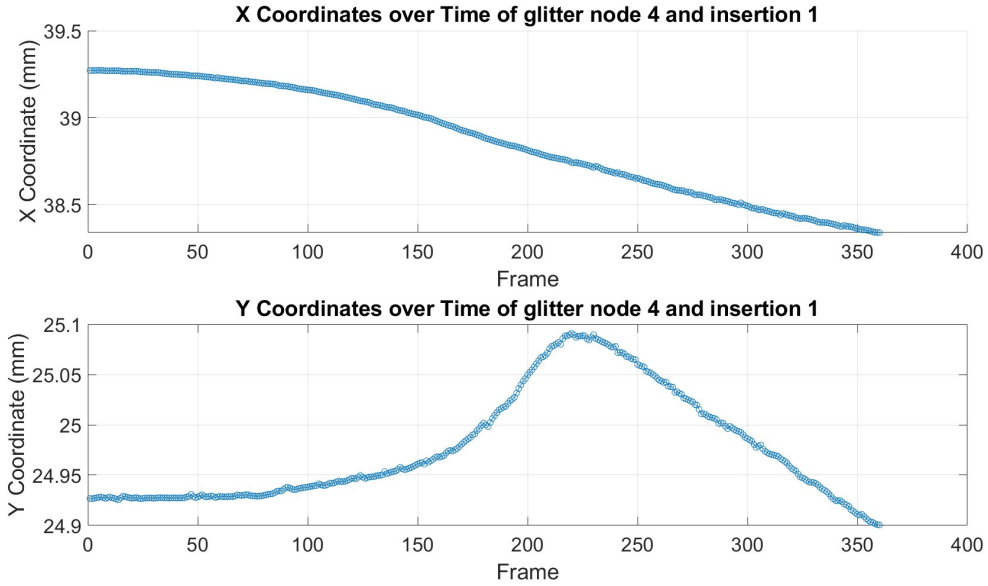

Figure 8.43: X- and y- displacement of glitter node 4 over time of insertion 1 into a 10% wt gelatin phantom at 10 mm/sec.